

**Infrared Radiative Properties of Tropical Cirrus Clouds Inferred  
from Broadband Measurements**

By

Keith T. Griffith and Stephen K. Cox

Department of Atmospheric Science  
Colorado State University  
Fort Collins, Colorado



**Department of  
Atmospheric Science**

Paper No. 269

INFRARED RADIATIVE PROPERTIES OF TROPICAL CIRRUS CLOUDS  
INFERRED FROM BROADBAND MEASUREMENTS

By

K.T. Griffith and S.K. Cox

Research Report supported by  
The Global Atmospheric Research Program,  
National Science Foundation and the  
GATE Project Office, NOAA Under grants  
OCD -74-21678 and 04-6-158-44036

Department of Atmospheric Science  
Colorado State University  
Fort Collins, Colorado  
80523

April 1977

Atmospheric Science Paper No. 269

## ABSTRACT

The longwave radiative properties of tropical cirrus clouds are studied using broadband hemispheric irradiance data. The data used were collected by the National Center for Atmospheric Research (NCAR) Sabreliner during the GARP Atlantic Tropical Experiment (GATE) in the summer of 1974. The longwave emissivities and the vertical profile of cooling rates are derived. Additionally, a broadband mass absorption coefficient relating water content to emissivity is defined. These parameters are determined by employing a broadband infrared radiative transfer routine. This model requires that the vertical structure of upward and downward irradiance, ice water content, temperature, water vapor and carbon dioxide along with cloud top and cloud base pressure be specified.

Three cases of high cirrus clouds are analyzed. It is found that these clouds approached an emissivity of 1.0 in a vertical distance of 1.0 to 1.5 kilometers. Broadband mass absorption coefficients ranging from  $0.076 \text{ m}^2 \text{ g}^{-1}$  to  $0.096 \text{ m}^2 \text{ g}^{-1}$  are derived. Comparison of these results to both theoretical and observational studies reveal large differences.

Ice water content information is deduced from data collected by a one-dimensional particle spectrometer. Information on the variability of IWC in the horizontal and its correlation to downward irradiance is presented. The observed particle size distributions are also depicted and discussed.

## ACKNOWLEDGEMENTS

The authors wish to express their gratitude to Dr. Robert Knollenberg of Particle Measuring Systems, Inc., who assisted in the design of the experiment and in the analysis of the cloud particle data. Many helpful suggestions have been made by Dr. Thomas McKee, Dr. David Krueger and Dr. Helen Poland. Special thanks are due to Ms. M. Charline Polifka for her valuable programming assistance, Ms. Sandy Wunch for typing the manuscript and to Renee Jorgensen for drafting the figures.

This research has been supported by the Global Atmospheric Research Program, National Science Foundation and the GATE Project Office, NOAA under grants OCD -74-21678 and 04-6-158-44036.

Acknowledgement is also made to the flight facility and the computing facility of the National Center for Atmospheric Research, sponsored by the National Science Foundation.

## TABLE OF CONTENTS

	<u>PAGE</u>
ABSTRACT	ii
ACKNOWLEDGEMENTS	iii
TABLE OF CONTENTS	iv
LIST OF TABLES	vi
LIST OF FIGURES	vii
LIST OF SYMBOLS	x
1.0 INTRODUCTION	1
2.0 BROADBAND INFRARED RADIATIVE TRANSFER MODEL	3
2.1 Method of calculation	3
2.2 Cloud contributions	6
2.3 Iterative solution for emissivity values	11
2.4 Sensitivity testing of the model	13
2.41 The effect of random errors in irradiance measurements	15
2.42 The effect of bias errors in irradiance measurements	18
2.43 The effect of errors in ice water content	20
2.44 The effect of cloud top and cloud base height errors	20
2.45 The effect of errors in temperature measurements	22
2.46 The effect of errors in water vapor mixing ratio	23
2.47 The effect of concurrent measurement errors	25
2.48 Summary of sensitivity testing	27
3.0 APPLICATION OF THE MODEL TO GATE SABRELINER DATA	29
3.1 Description of data available	29

## TABLE OF CONTENTS - Continued

	<u>PAGE</u>
3.2 Reduction and Analysis of Data	30
3.21 Radiation and state variable sampling	30
3.22 Ice water content sampling	31
3.23 Cloud top and base determination	31
3.24 Variability of IWC and downward irradiance	34
3.25 Cirrus cloud particle size distribution	38
3.3 Case Studies	41
3.31 Day 226 - August 14, 1974	41
3.32 Day 232 - August 20, 1974	52
3.33 Day 251 - September 8, 1974	61
3.34 Summary of case studies	68
3.4 Possible explanations of the discrepancy between theory and observation	74
3.5 Comparison to other observational studies	81
4.0 CONCLUSIONS	86
REFERENCES	89
APPENDIX: Derivation of cirrus cloud ice water content information from Knollenberg probe data	92

## LIST OF TABLES

	<u>PAGE</u>
1. Sources of infrared emissivity data and effective optical path exponents used in IRADLON-2.	5
2. Flux perturbations as a function of pressure and the resulting K values for 10 trial cases.	16
3. The effect of errors in IWC on retrieval of emissivities.	21
4. The effect of water vapor on the net gain of irradiance from a cloud.	24
5. Errors in emissivity as a function of depth below cloud top for concurrent measurement errors.	26
6. Summary of sensitivity tests.	28
A1. Correction factors used for adjusting measured IWC.	101
A2. The effect of particle shape assumption on calculated IWC.	102

## LIST OF FIGURES

<u>FIGURE</u>		<u>PAGE</u>
1	Comparison of $\epsilon_{\text{CLOUD}}$ to $\epsilon^*$ for a typical cirrus cloud.	10
2	Tropical atmosphere used to supplement measured levels.	12
3	Atmosphere used for sensitivity testing of IRADLON-2.	14
4	Emissivity as a function of pressure for two K values.	17
5	The effect of instrument bias errors on the retrieval of K values.	19
6	Change in <u>upward</u> flux as a function of K value for 2 levels in the cloud.	32
7	Simultaneous measurements of downward irradiance and ice water content vs. distance for Day 226, 35,000 ft.	35
8	Simultaneous measurements of downward irradiance and ice water content vs. distance for Day 232, 40,000 ft.	36
9	Simultaneous measurements of downward irradiance and ice water content vs. distance for Day 232, 36,000 ft.	37
10	Measured particle size distribution for three data flight legs with total number of particles normalized to 10,000 per cubic meter and for assumed column shape.	39
11	Measured particle size distribution for three data flight legs with total number of particles normalized to 10,000 per cubic meter and for assumed rosette shape.	40
12	Vertical profile of IWC for Day 226.	42
13	Day 226 Irradiance profiles.	43
14	Day 226 emissivity vs. distance below cloud top with comparisons to theoretical studies of Hunt (1973) and Liou (1974).	45
15	Day 226 emissivity vs. total column water content with comparisons to Hunt (1973) and Liou (1974).	47
16	Heating rate as a function of pressure, Day 226.	50
17	Comparison of effect of different K values on heating rate, Day 226.	51
18	Vertical profile of ice water content for Day 232.	53

LIST OF FIGURES - Continued

<u>FIGURE</u>	<u>PAGE</u>
19 Day 232 irradiance profiles.	56
20 Day 232 emissivity vs. distance below cloud top with comparisons to Hunt (1973) and Liou (1974).	57
21 Day 232 emissivity vs. total column water content with comparisons to Hunt (1973) and Liou (1974).	58
22 Heating rate as a function of pressure, Day 232.	60
23 Day 251 vertical profile of IWC.	62
24 Day 251 irradiance profiles.	64
25 Day 251 emissivity vs. distance below cloud top with comparisons to Hunt (1973) and Liou (1974).	66
26 Day 251 emissivity vs. total column water content with comparisons to Hunt (1973) and Liou (1974).	67
27 Heating rate as a function of pressure for Day 251.	69
28 Heating rate as a function of pressure for the three cases. (normalized cloud top location).	70
29 Flux emissivity vs. distance below cloud top for the three cases studied, with total column water content at selected points.	71
30 Effective emissivity, $\epsilon^*$ , vs. frequency of occurrence for data flight leg at 36,000 ft. on Day 232. (1.3 kilometers below cloud top).	73
31 Particle size distribution for Day 226, 34,000 ft. Crystals are here assumed to be 100% columns. Measured points and two possible extrapolations are illustrated.	75
32 Ice water content as a function of particle size for Day 226, 34,000 ft. Crystals are here assumed to be 100% columns. Measured points and two possible extrapolations are illustrated.	76
33 Day 226 emissivity vs. total column water content with comparisons to Hunt (1973) and Liou (1974). Observed curve derived using modified ice water content obtained from extrapolations of Figures 31 and 32. (Dashed line envelope indicates uncertainty in observations.)	78

LIST OF FIGURES - Continued

<u>FIGURE</u>		<u>PAGE</u>
34	Day 226 emissivity vs. distance below cloud top with comparisons to theoretical studies of Hunt (1973) and Liou (1974). These curves use the modified ice water content obtained from Figures 31 and 32. (Dashed line envelope indicates uncertainty in observation.)	79
35	Comparison between present study and previous observations of intensity emissivity vs. cloud thickness.	82
36	Comparison of emissivity vs. total column water content between present study and theoretical results for water clouds of similar LWC and drop size distribution.	85
A1	Corrected crystal size vs. indicated crystal size (Columns).	94
A2	Corrected crystal size vs. indicated crystal size (Rosettes).	95
A3	Equivalent water drop diameter vs. corrected crystal size for the two crystal shapes assumed to be present.	97
A4	Particle size distribution for Day 226, 34,000 feet, combined rosettes (50%) and columns (50%).	99
A5	Ice water content as a function of particle size for a mixture of columns (50%) and rosettes (50%) for Day 226, 34,000 ft.	100

## LIST OF SYMBOLS

$C_p$	Specific heat of air at constant pressure, $1.00 \text{ Joule g}^{-1} \text{ } ^\circ\text{K}^{-1}$
$\text{CO}_2$	Carbon dioxide
CS1	Tabular corrected particle size, $\mu\text{m}$
CSF	Final airspeed corrected particle size, $\mu\text{m}$
$g$	Acceleration due to gravity, $9.8 \text{ m sec}^{-2}$
$\text{H}_2\text{O}$	Water vapor
$H$	Longwave irradiance, $\text{wm}^{-2}$
$H_{\uparrow}$	Upward longwave irradiance, $\text{wm}^{-2}$
$H_{\downarrow}$	Downward longwave irradiance, $\text{wm}^{-2}$
$H_0$	Longwave background irradiance, $\text{wm}^{-2}$
$H(P)$	Longwave irradiance at pressure level $P$ , $\text{wm}^{-2}$
$H_{\text{NET}}$	Net longwave irradiance, $H_{\downarrow} - H_{\uparrow}$ , $\text{wm}^{-2}$
$H_B(\downarrow)$	Downward longwave irradiance at cloud base, $\text{wm}^{-2}$
$H_T(\downarrow)$	Downward longwave irradiance at cloud top, $\text{wm}^{-2}$
IWC	Ice water content, $\text{gm}^{-3}$
$K$	Longwave broadband grey body mass absorption coefficient, $\text{m}^2\text{g}^{-1}$
LWC	Liquid water content, $\text{gm}^{-3}$
$\text{O}_3$	Ozone
$P$	Pressure, mb
$P_0$	Standard pressure, 1013.25 mb
$T$	Temperature, $^\circ\text{K}$
$T_0$	Standard temperature, $273.16^\circ\text{K}$
$\Delta T$	Temperature increment, $^\circ\text{K}$

LIST OF SYMBOLS - Continued

$T_B$	Cloud base temperature, °K
TAS	True air speed, m sec <sup>-1</sup>
$\Delta t$	Time increment
$\Delta z$	Distance, m
$\alpha$	Pressure broadening exponent
$\beta$	Temperature broadening exponent
$\Delta \epsilon$	Longwave flux emissivity increment
$\epsilon^{*\downarrow}$	Layer effective longwave flux emissivity derived from downward irradiance
$\sigma$	Stefan-Boltzman constant, $5.67 \times 10^{-8} \text{ w m}^{-2} \text{ } ^\circ\text{K}^{-4}$
$\mu$	Uncorrected optical path, gm <sup>-2</sup>
$\mu^*$	Pressure and temperature corrected optical path, gm <sup>-2</sup>
$\lambda$	Wavelength
R	Radius of equivalent spherical particle

## 1.0 INTRODUCTION

Radiative properties of cirrus clouds have been observed by many authors using several different techniques [Brewer and Houghton (1956); Fritz and Rao (1967); Kuhn and Weickmann (1969); Platt (1973); Platt and Gambling (1971); Allen (1971); Davis (1971)]. However, information on cloud microphysics has been lacking in every study. Theoretical studies of the radiative properties of cirrus have been made by Hunt (1973) and Liou (1974). These theoretical studies must incorporate crucial assumptions about the microphysical nature of cirrus clouds.

The present study combines aircraft measurements of cirrus cloud microphysics with simultaneous radiometric observations. This unique data set may serve as a first step toward the coherent merging of observation and theory.

The longwave radiative properties of tropical cirrus clouds are studied using broadband hemispheric irradiance data. The longwave emissivities and the vertical profile of cooling rates are determined. Additionally, a broadband mass absorption coefficient relating water content to emissivity is defined.

These parameters are determined by employing a variation on a broadband infrared radiative transfer computational routine that was outlined by Cox, et al. (1976). The routine requires that the vertical structure of upward and downward irradiance, temperature, water vapor, carbon dioxide and ozone (if desired) along with the cloud top and cloud base pressure be specified. Emissivities and cooling rates are computed with this information alone. If the vertical structure of the ice water content is also known, a broadband mass absorption coefficient of the solid water component may be computed.

The vertical variation of emissivity in the cloud layer is smoothed using an exponential relation. The best fit is obtained by an iterative method. Cooling rates are then calculated from the divergence of net radiation which is determined using the smoothed cloud emissivities. The emissivity of the cloud aerosol alone is isolated from the effects of water vapor and carbon dioxide in the cloud layer. This differs from the concept of the effective emissivity of the layer which has been used previously by some authors (Cox, 1971, 1976; Paltridge, 1974). Layer effective emissivity does not distinguish between the contributions of the gaseous constituents and the contribution due to the cloud aerosol itself.

The data used were collected by the National Center for Atmospheric Research (NCAR) Sabreliner during the GARP Atlantic Tropical Experiment (GATE) in the summer of 1974. The longwave irradiance data were obtained using pyrgeometers built by the Eppley Laboratory, Inc., Newport, Rhode Island. A complete description of the instrument, its limitations and the techniques used in reducing the raw Sabreliner data may be found in Albrecht, et al (1974), Albrecht and Cox (1976a, 1976b).

The ice water content information was derived from data collected by a one-dimensional particle spectrometer manufactured by Particle Measuring Systems, Inc., Boulder, Colorado. A description of this instrument is given by Heymsfield (1976).

## 2.0 BROADBAND INFRARED RADIATIVE TRANSFER MODEL

The infrared numerical transfer model used in this study, hereafter referred to as IRADLON-2, is designed to calculate the upward and downward broadband infrared (IR) irradiances at specified levels in the atmosphere using the radiative transfer equation. These IR irradiances are obtained from the vertical distribution of temperature, water vapor, clouds, ozone, and carbon dioxide as independent variables in a radiative transfer equation evaluation. The calculated irradiances are compared to the measured irradiances at each level and the cloud contribution (i.e. emissivity) is adjusted in an iterative scheme until the best match is achieved. The radiative heating rates are then calculated from the divergence of net radiation which is determined using the smoothed irradiance profile.

### 2.1 Method of Calculation

A broadband approximation to the rigorous spectral radiative transfer equation is used. The equation is evaluated at specified levels in its finite difference form, taking into account the contribution of the various atmospheric constituents.

$$\begin{aligned}
 H(P) = H_0 & \left[ 1 - \sum_{i=1}^n \Delta\epsilon_{iH_2O} - \sum_{i=1}^n \Delta\epsilon_{iCO_2} - \sum_{i=1}^n \Delta\epsilon_{iO_3} \right. \\
 & \left. - \sum_{i=1}^n \Delta\epsilon_{iCLOUD} + \sum_{i=1}^n \Delta\epsilon_{iOVERLAP} \right] \quad (1) \\
 & + \sum_{i=1}^n H_i \left[ \Delta\epsilon_{iH_2O} + \Delta\epsilon_{iCO_2} + \Delta\epsilon_{iO_3} + \Delta\epsilon_{iCLOUD} - \Delta\epsilon_{iOVERLAP} \right]
 \end{aligned}$$

where  $H(P)$  is the irradiance at pressure level  $P$ . This can be either upward or downward irradiance.  $H_0$  is the emitted irradiance of the background surface. For  $H\downarrow$  calculations, this is the earth's surface emission. The program assumes perfect Planckian emission of the surface, therefore,  $H_0 = \sigma T_{\text{SURFACE}}^4$ . The program assumes that there is no IR arriving from space, therefore,  $H_0 = 0$  for the  $H\downarrow$  calculation. This first term in Eq. 1 represents the transmitted term; it gives the contribution to the total irradiance at a level  $P$ , emanating from the underlying surface.  $H_i$  is equal to  $\sigma T_i^4$ , where  $T_i$  is the average absolute temperature of the layer  $i$ . This term accounts for the radiation originating from within the atmosphere itself.  $\Delta\epsilon_{i\text{H}_2\text{O}}$ ,  $\Delta\epsilon_{i\text{CO}_2}$ , etc. are the emissivity increments in the layer  $i$  from each of the constituents  $\text{H}_2\text{O}$ ,  $\text{CO}_2$ , etc.  $\Delta\epsilon_{i\text{OVERLAP}}$  refers to both the  $\text{H}_2\text{O} - \text{CO}_2$  gaseous overlap region and the  $\text{H}_2\text{O} - \text{CO}_2$  vs. cloud overlap correction.

The index  $i$  will always equal 1 in the layer just above level  $P$  for the  $H\downarrow$  calculation and will be equal to 1 in the layer just below level  $P$  for the  $H\uparrow$  calculation. The index is incremented going away from the level  $P$  toward the top of the atmosphere for  $H\downarrow$  or toward the surface for  $H\uparrow$  computations. The stopping point of the summation,  $N$ , changes as the level of interest,  $P$ , changes. It is equal to the number of layers between level  $P$  and the top or bottom of the atmosphere as appropriate for  $H\downarrow$  or  $H\uparrow$  respectively.

In Equation 1, we assume that we know the vertical profiles of the absorbing gases,  $\text{H}_2\text{O}$ ,  $\text{CO}_2$ , and  $\text{O}_3$ . We also know  $H_0$  and all  $H_i$  by virtue of knowing the temperature as a function of pressure and using the Stefan-Boltzmann Law. The aircraft radiometric measurements provide us with  $H(P)$  at specific levels. The one unknown quantity is the cloud

emissivity contribution and hence the cloud overlap correction. It is this one element that is adjusted iteratively to achieve agreement with the measured irradiances.

The gaseous emissivity data referred to in Eq. 1 have been compiled from several authors as outlined in Table 1.

	<u>Source</u>	<u><math>\alpha</math></u>	<u><math>\beta</math></u>
H <sub>2</sub> O 6.3 $\mu$ m	Staley and Jurica (1970)	1.0	0.5
H <sub>2</sub> O continuum	Bignell (1970), Cox (1973)	0	0
H <sub>2</sub> O rotational	Smith (1969)	Tabular	Tabular
CO <sub>2</sub>	Smith (1969)	Tabular	Tabular
O <sub>3</sub>	Walshaw (1957)	Tabular	Tabular
H <sub>2</sub> O - CO <sub>2</sub> OVERLAP	Staley and Jurica (1970)	1.0	0.5

Table 1: Sources of infrared emissivity data and effective optical path exponents used in IRADLON-2.

The effect of pressure and temperature broadening on the effective optical path  $\mu^*$ , is taken into account by a parameterization of the following form:

$$\mu^* = \mu \left( \frac{P}{P_0} \right)^\alpha \left( \frac{T_0}{T} \right)^\beta \quad (2)$$

where  $T$  is temperature,  $P$  is pressure and  $\mu$  is optical path.  $P_0$  is taken to be 1013 mb and  $T_0$  is 273°K. Adjusting the two exponents  $\alpha$  and  $\beta$  gives

one the ability to modify the magnitude of the effect. Table 1 summarizes the  $\alpha$  and  $\beta$  values used in IRADLON-2.

With the exception of the treatment of cloud and the cloud overlap correction, the basic computational technique for the gaseous constituents follows the method of Cox (1973).

After the determination of the upward and downward irradiances and using the definition  $\Delta H_{\text{NET}} = H_{\uparrow} - H_{\downarrow}$ , the layer heating rates are calculated from the formula:

$$\frac{\Delta T}{\Delta t} = \frac{g}{c_p} \frac{\Delta H_{\text{NET}}}{\Delta P} . \quad (3)$$

This is an instantaneous heating rate based on the observed irradiances. It is actually a measure of the rate of loss or gain of energy in the layer  $\Delta P$ . This energy flux may, of course, be manifested in some form other than sensible temperature change.

## 2.2 Cloud Contributions

Cloud contributions are handled in a manner similar to the other atmospheric constituents. Equation 3 describes the emissivity curve within the cloud in terms of the cloud thickness,  $z$ , in meters (distance from cloud top or base to the point in question), the liquid (or ice) water content, LWC, in  $\text{gm}^{-3}$  and a grey body mass absorption coefficient,  $K$ .

$$\epsilon_{\text{CLOUD}} = 1 - \exp(-K \text{ LWC } \Delta z) \quad (4)$$

see Paltridge (1974) for details on the derivation of Eq. 4.

Paltridge justifies the use of a constant mass absorption coefficient  $K$  by the following argument:

The mass absorption coefficient can be expressed as the ratio of the absorption cross-section to the liquid water content of the distribution. The liquid water content of a stratocumulus cloud increases with height and simultaneously the size distribution moves to larger radii. The absorption cross-section increases with increasing radius. Thus, as the LWC increases with height, the absorption cross-section also increases, tending to keep their ratio,  $K$ , relatively constant.

This reasoning does not apply to the cirrus clouds studied here. The vertical profile of ice water content generally shows a decrease with height while the size distribution remains relatively constant (see Sections 3.24, 3.25). It was decided to retain the form of Eq. 4 because empirically it produces a good fit to the observed data. It may be possible to demonstrate theoretically that this assumption of  $K$  being a constant is justifiable for the irregular cirrus particles, however, no attempt to provide that justification is made in this work.

A correction is made for the overlap between the cloud aerosol, which is assumed to radiate as a "grey" body, and the gaseous constituents of the atmosphere. The grey body cloud is assumed to radiate at all the wavelengths encompassed by the Planck function for the cloud temperature but with each wavelength interval reduced in proportion to the emissivity of the cloud. It must, therefore, overlap the emission

of water vapor, carbon dioxide, etc. in their respective bands. This duplication is accounted for by defining a cloud overlap term which is subtracted from the other emissivity increments:

$$\Delta\epsilon_{i\text{CLOUD OVERLAP}} = \Delta\epsilon_{i\text{CLOUD}} [\Delta\epsilon_{i\text{H}_2\text{O}} + \Delta\epsilon_{i\text{CO}_2} + \Delta\epsilon_{i\text{O}_3}]. \quad (5)$$

This form of the cloud overlap correction precludes the possibility of the computed total atmospheric emissivity exceeding 1.0, as required by physical constraints. The cloud overlap is combined with the H<sub>2</sub>O - CO<sub>2</sub> gaseous overlap correction in the single term  $\Delta\epsilon_{i\text{OVERLAP}}$  in Eq. 1.

The concept of layer effective emissivity as used by Cox (1971, 1976) and Paltridge (1974) differs from the definition of cloud emissivity used here. Equation 6 gives the effective emissivity for the downward irradiance according to Cox (1976). A similar expression is used for the upward irradiance.

$$\epsilon^*(\downarrow) = \frac{H_B(\downarrow) - H_T(\downarrow)}{\sigma T_B^4 - H_T(\downarrow)}. \quad (6)$$

This simply gives the ratio of the observed change in downward irradiance through the layer to the change in the irradiance which a "black" cloud would have produced. The subscripts B and T refer to cloud base and top respectively, the symbol ( $\downarrow$ ) refers to the downward irradiance and  $\sigma$  is the Stefan-Boltzmann constant. This expression includes the effects of

all the constituents of the layer, water vapor, carbon dioxide and ozone as well as the cloud itself and any other unspecified radiators, such as dust. Equation 4 defines the emissivity of the cloud liquid or ice substance alone. The iterative solution described below which uses Eq. 4 distinguishes the cloud aerosol emissivity from the contribution of water vapor, carbon dioxide and ozone.

Figure 1 compares  $\epsilon_{\text{CLOUD}}$  derived from Eq. 4 to  $\epsilon^*$  derived from Eq. 6 for a typical cirrus cloud. It is seen that  $\epsilon^*$  is slightly greater (1% - 2%) than  $\epsilon_{\text{CLOUD}}$  for emissivities less than about 0.5. This occurs because the contribution of water vapor is excluded from  $\epsilon_{\text{CLOUD}}$ . The very small difference between the two curves is an indication of how dominant the cloud aerosol is in comparison to the water vapor of the cloud layer.

At emissivities greater than approximately 0.6,  $\epsilon^*$  is less than  $\epsilon_{\text{CLOUD}}$ . This occurs because of the temperature used in computing the two emissivities. Equation 6 shows that the change in downward irradiance through the layer is compared to a term containing  $\sigma T^4$  of the base of the layer. In an atmosphere with a positive lapse rate, this is the warmest level and therefore, the highest possible irradiance. IRADLON-2, using Eq. 4, calculates multi-layer contributions to the downward irradiance using the average temperature of the layers. This results in a lower effective temperature for the layer and therefore, a higher emissivity. This multi-layer treatment of the cloud emissivity is a better approximation to the way in which radiative transfer takes place.

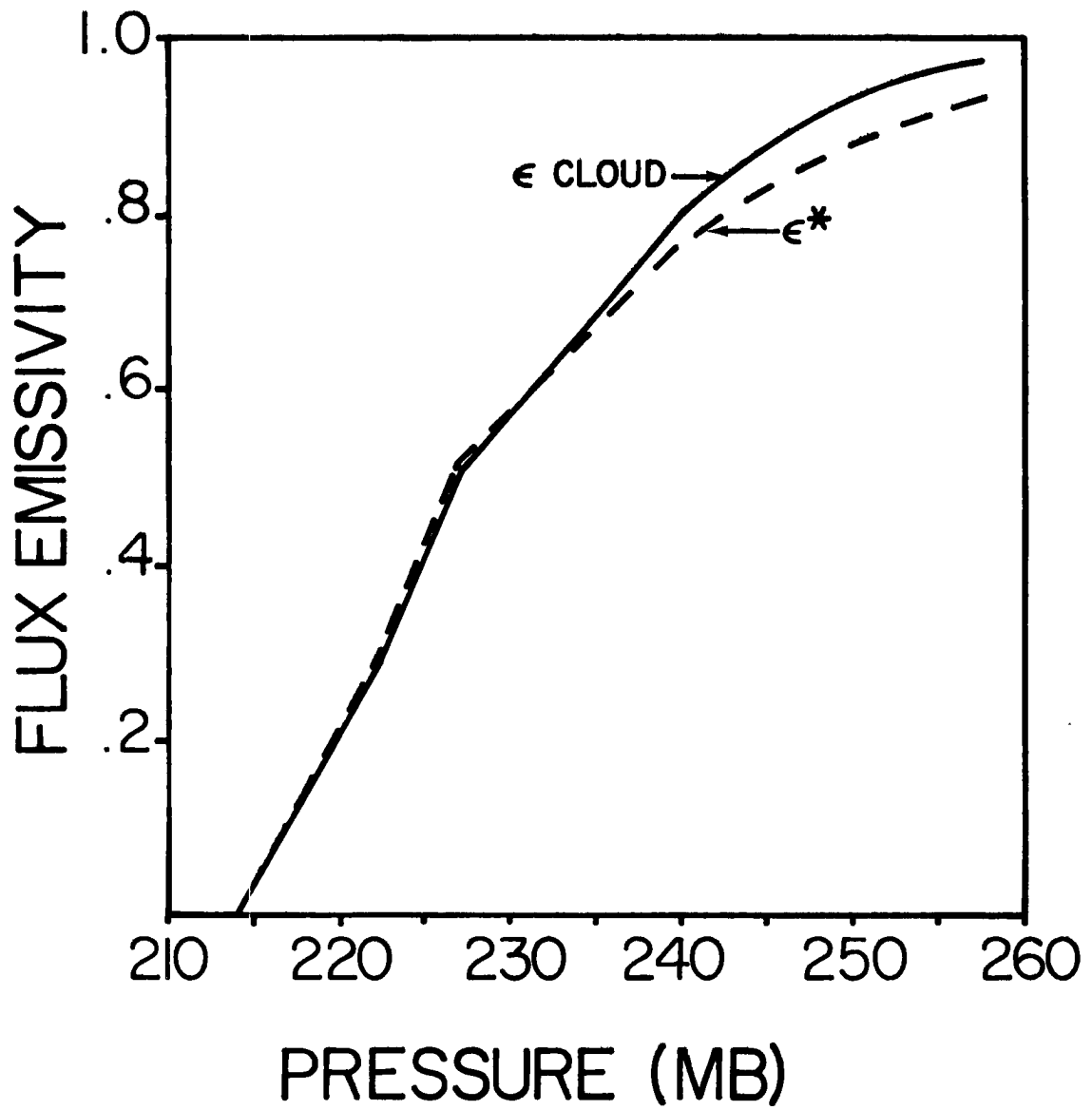


Figure 1. Comparison of  $\epsilon_{\text{CLOUD}}$  to  $\epsilon^*$  for a typical cirrus cloud.

### 2.3 Iterative Solution for Emissivity Values

A profile of measured irradiances was analyzed in the following manner:

- Step 1. An atmosphere (pressure, temperature, mixing ratio,  $\text{CO}_2$ ) was constructed using the actual collected data for as many levels as were available and then filling in the remaining levels with data from a typical tropical atmosphere. That atmosphere is graphed in Fig. 2. Ozone was omitted from all calculations because of its small effect on tropospheric IR divergence. Carbon dioxide was assumed to be constant with height and have a mixing ratio of 0.486 g/kg.
- Step 2. In order to obtain correct cloud emissivities, it is necessary that the downward irradiance at cloud top and the upward irradiance at cloud base be identical for the calculated and measured cases. To satisfy this condition, the model was run with no cloud present for the first trial. The cloud top and cloud base calculated irradiances were then compared to the measured irradiances. If they did not agree within  $.007 \text{ wm}^{-2}$ , an adjustment was made to the background irradiance,  $H_0$  of Eq. 1, to ensure agreement at the cloud boundaries.
- Step 3. Cloud parameters of ice water content, cloud base and top pressure and an initial guess of the mass absorption coefficient,  $K$  are input to the model. A complete profile of irradiances is generated and compared to the measured irradiances. A sum of the absolute value of the deviations between calculated and measured irradiances is found. Now  $K$  is incremented or decremented by  $0.001 \text{ m}^2 \text{ g}^{-1}$  and a new profile of calculated

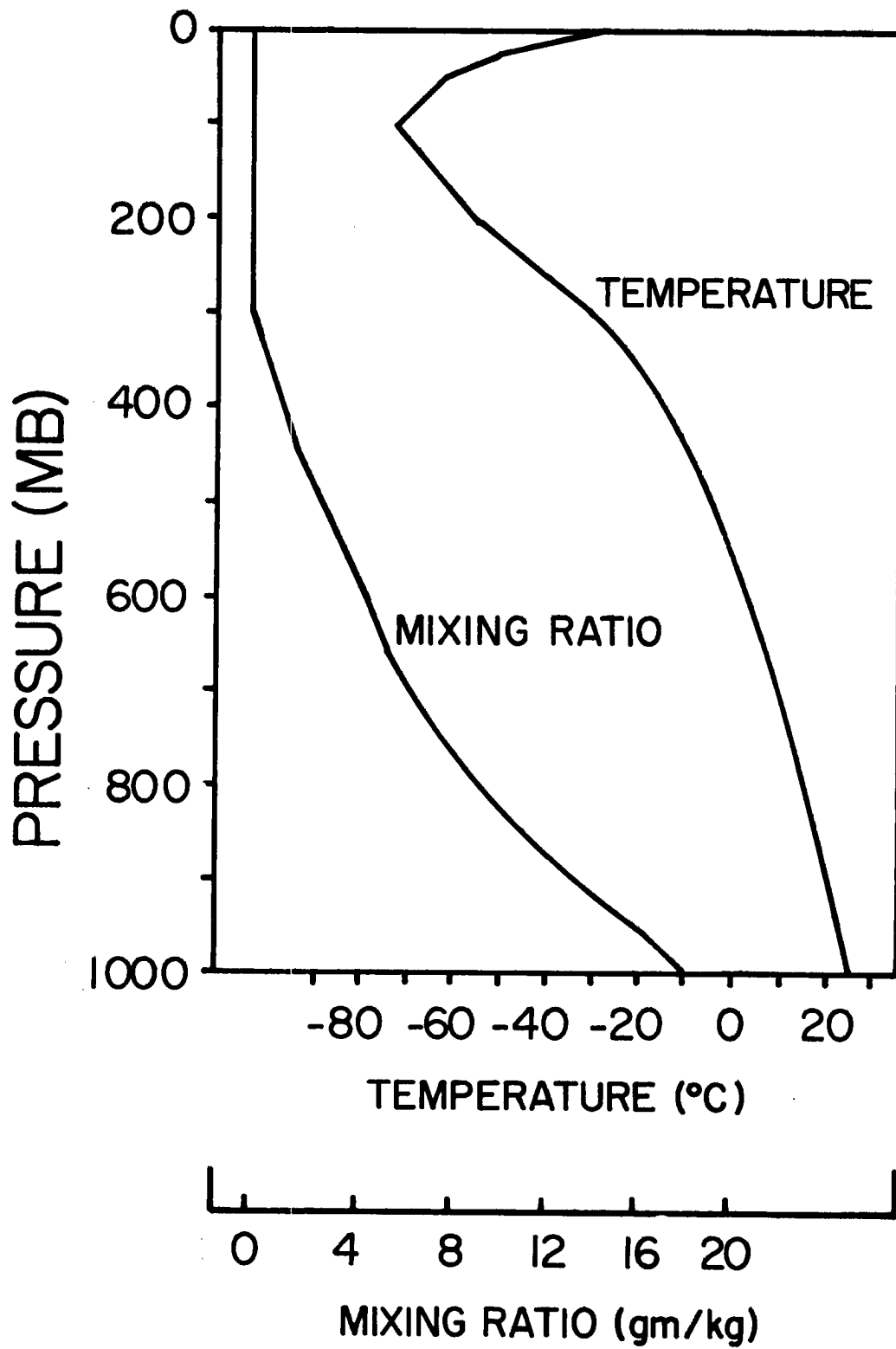


Figure 2. Tropical atmosphere used to supplement measured levels.

irradiance is generated, and a new comparison with measured irradiance is made. The sum of the absolute value of the deviations is recalculated and compared to the last sum of deviations. The process continues until the sum of the deviations is minimized. At that time the  $K$  that produced the minimum deviation and the resulting cloud emissivities are known and the cooling rates follow directly.

#### 2.40 Sensitivity Testing of the Model

The model was tested extensively to determine how well it could retrieve the desired parameters when the input data contained errors. It is inevitable that there will be noise in the data on radiation, temperature, moisture, cloud top and cloud base pressures, and ice water content. This noise may be due to instrument errors, inhomogeneities in the meteorological situation or even inaccuracies in observers' notes. It is essential to know how tolerant the model is of these conditions.

A profile of both upward and downward irradiances was generated using the atmosphere depicted in Fig. 3 with a cloud between 300 mb and 400 mb. The ice water content was  $0.1 \text{ gm}^{-3}$  throughout the cloud and an absorption coefficient of  $0.050 \text{ m}^2 \text{ g}^{-1}$  was used. This profile of irradiances generated from a cloud of known properties was input to the model. The proper ice water content and cloud base and top pressure was supplied but the initial guess for  $K$  was offset from the known correct value. The iterative scheme retrieved the proper  $K$  value and profile of cloud emissivity flawlessly regardless of the direction of the initial  $K$  offset.

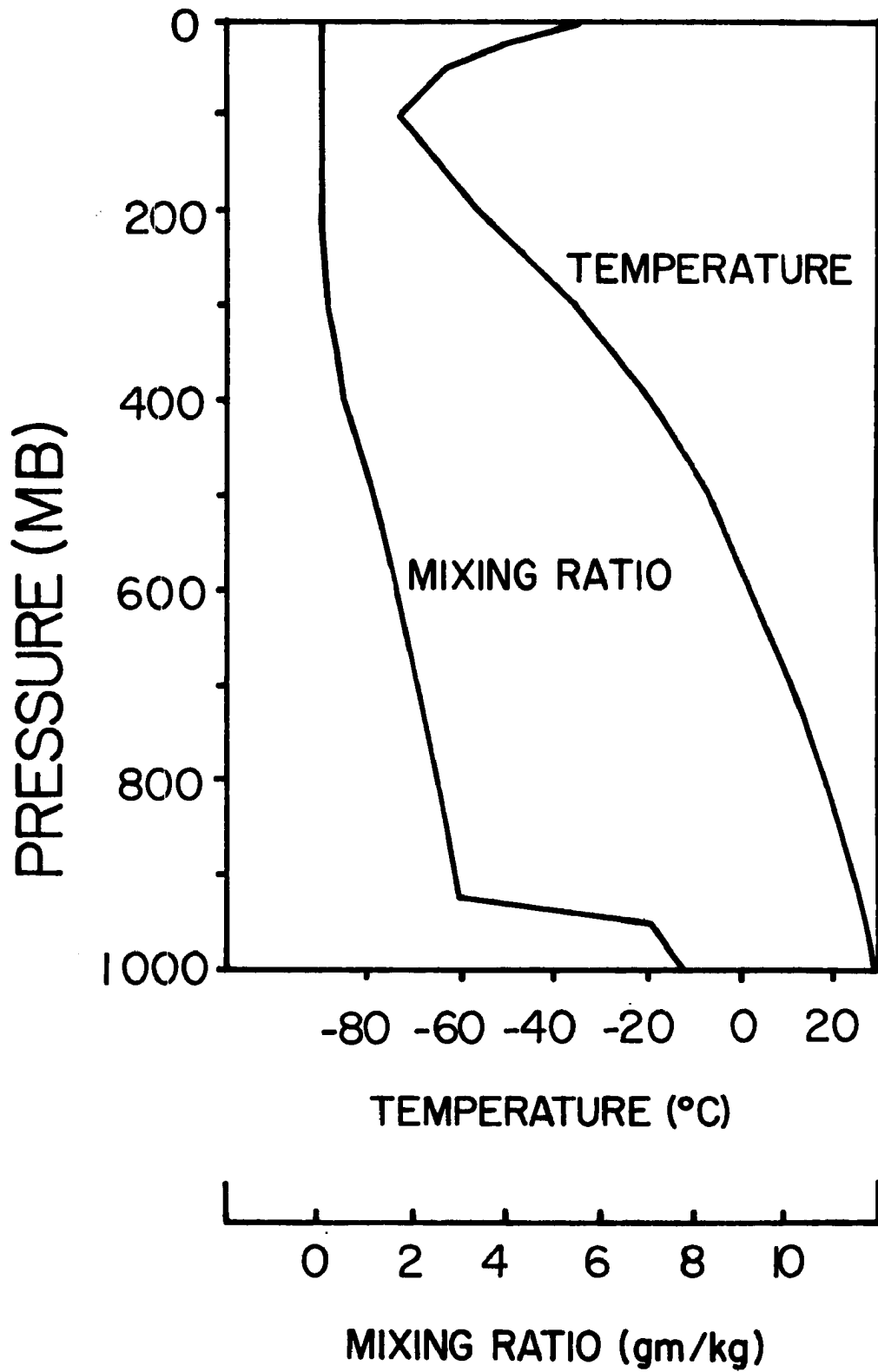


Figure 3. Atmosphere used for sensitivity testing of IRADLON-2.

## 2.41 The Effect of Random Errors in Irradiance Measurements

The next avenue of exploration was to randomly perturb the simulated measured irradiances. Accurate information was still supplied for the cloud top and base and the ice water content. The only deviation from perfect data that was allowed was in the irradiances themselves. In addition, downward irradiances above cloud top and upward irradiances below cloud base were not perturbed because of the boundary condition requirement that they be identical at cloud top and base, respectively. In any case, the presence of the cloud does not affect downward irradiance above cloud top or upward irradiance below cloud base.

Table 2 summarizes the results of 10 trial runs for the downward irradiance only. Similar results are found for the upward irradiance. The amount and direction of the irradiance perturbation is listed as a function of pressure, the standard deviation of the perturbations, and the resulting value of  $K$  are tabulated. The cloud emissivity at each pressure level for the unperturbed case is shown at the bottom for reference. It is seen that the deviation of the value  $K$  is directly proportional to the size and direction of the irradiance perturbation of the first cloud level, 310 mb. Note that the cloud is essentially black by the second level, 325 mb, with an emissivity of .9395. Below the point at which the cloud turns black, the irradiance perturbations become meaningless. That is, the choice of a  $K$  value can make very little difference to the irradiance in that situation. The burden of determining the appropriate  $K$  falls to only those points at which the cloud has not achieved blackness. Hence, for the test cases, the first point is paramount in determining the correct  $K$ . Figure 4 demonstrates this point; it shows the curve of emissivity vs. pressure for two different

TRIAL NUMBER	IRRADIANCE PERTURBATIONS ( $\text{wm}^{-2}$ ) AS A FUNCTION OF PRESSURE - DOWNWARD IRRADIANCE ONLY							K VALUE	STD. DEV. OF PERTURBATIONS $\text{wm}^{-2}$
	300 mb	310 mb	325 mb	350 mb	375 mb	390 mb	400 mb		
1	0	-4.6	+1.7	-5.0	-9.8	-3.3	+3.1	.045	4.33
2	0	+5.9	-28.6	+7.1	+21.6	+2.0	+1.5	.057	15.08
3	0	-7.9	-5.2	+2.6	+10.4	-6.7	-3.7	.042	6.38
4	0	+8.7	-9.7	-6.5	-4.8	-2.1	+5.9	.061	6.59
5	0	-7.9	-38.2	+9.5	+28.9	-2.7	+2.0	.060	20.18
6	0	+0.9	-4.5	+1.1	+3.4	+0.3	+0.2	.051	2.35
7	0	+3.9	-19.1	+4.7	+15.9	+1.4	+1.0	.055	10.39
8	0	+2.0	-9.6	+2.4	+7.9	+0.7	+0.5	.052	5.19
9	0	+9.3	-5.1	-7.1	+0.2	-2.8	-1.3	.061	5.25
10	0	0	0	0	0	0	0	.050	0.00
Emissivity of Unperturbed case								unperturbed case	
	0	.681	.939	.996	.999	.999	.999		

TABLE 2. Irradiance perturbations as a function of pressure and the resulting K values for 10 trial cases.

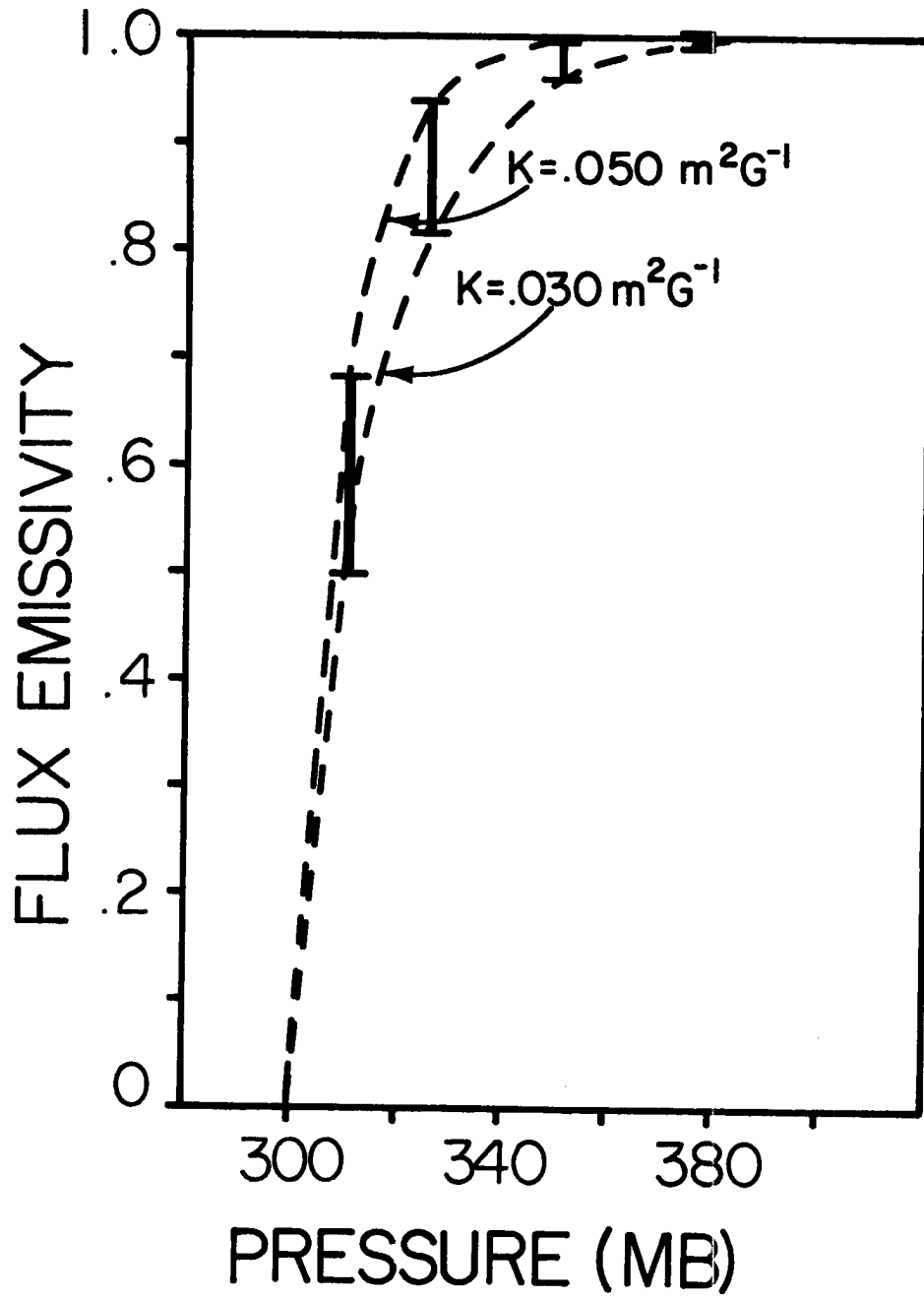


Figure 4. Emissivity as a function of pressure for two K values.

values of  $K$ . Note that the change in emissivity for a given change in  $K$  is much greater at short distances into the cloud. The irradiance perturbations used in the test are larger than the expected random instrumental errors of approximately  $2 \text{ Wm}^{-2}$  (Albrecht, et al., 1974). For test #8, in which the perturbation of the first point approximates this expected random error of  $2 \text{ Wm}^{-2}$ , the  $K$  value is within 4% of the target value.

#### 2.42 The Effect of Bias Errors in Irradiance Measurements

The possibility of a bias error in the instrument that would shift the entire curve uniformly either up or down was explored. The known measured irradiances were offset by various amounts and the retrieved  $K$  values were monitored. Figure 5 depicts the variation in  $K$  value as a function of the amount and direction of the curve offset. This figure shows that for errors in absolute instrument accuracy of up to  $\pm 5 \text{ Wm}^{-2}$ , the  $K$  value is within 12%. This dependency on the accuracy of the pyrgeometer is therefore, quite critical. However, there are two considerations which will help in assessing this accuracy and making adjustments when necessary. First, in an atmosphere with a positive lapse rate of temperature, the downward irradiance at any level should never exceed the blackbody irradiance computed from ambient temperature. This puts an upper physical limit on the downward measurement. Secondly, when the cloud achieves blackness, the measured irradiance profile must basically parallel the curve of ambient temperature blackbody irradiance. The distance required to go from cloud top to the point at which the downward irradiance begins to parallel the blackbody curve is the distance in which the cloud becomes radiatively black. This distance corresponds

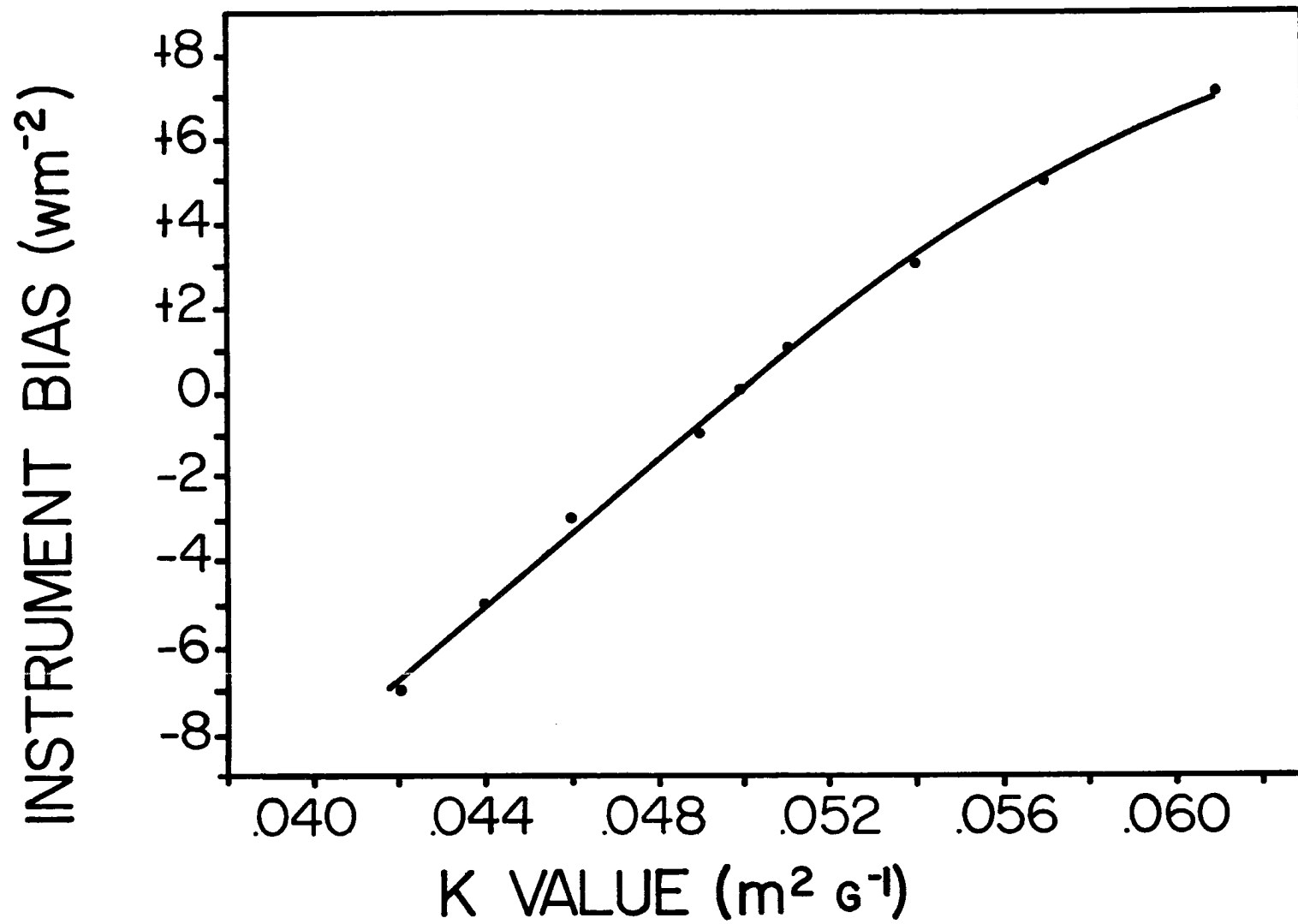


Figure 5. The effect of instrument bias errors on the retrieval of K values.

to a minimum temperature which the instrument can "see" and hence to a minimum possible downward irradiance. The envelope defined by these two points will generally give a range of reasonable downward irradiances of approximately  $10 \text{ Wm}^{-2}$ . An accuracy within  $\pm 5 \text{ Wm}^{-2}$  is therefore to be expected.

#### 2.43 The Effect of Errors in Ice Water Content

The effect of errors in ice water content was examined next. Cloud top, base, and irradiances were correctly specified but the ice water content was varied. As would be expected from examining Eq. 4, the K value varies inversely with IWC. But, for reasons analogous to those mentioned in the case of irradiance perturbations, the result is heavily weighted by those points with lower cloud emissivities. Table 3 gives an example of two perturbed cases, one with high and one with low cloud top water content. The unperturbed case is shown for comparison. Note that the total cloud water content is the same for the three cases and that the product of K and the average IWC of cloud points with emissivity less than 0.9 is nearly conserved. Table 3 lists the values of emissivity through the cloud for the three IWC profiles. The model does a rather good job of reproducing the emissivity profile in spite of errors as large as 50% in IWC.

#### 2.44 The Effect of Cloud Top and Cloud Base Height Errors

The positioning of cloud top and cloud base was varied also. This affects K values by changing the  $\Delta z$  term in the exponential of Eq. 4. For example, if cloud top is reported to be higher than it actually is, the distance  $\Delta z$  from cloud top to the first irradiance measurement within the cloud will be too large. This forces K to be smaller in order to

(1)	(2)	(3)	(4)	(5)	(6)		
IWC Cloud Top	Average IWC for Entire Cloud	IWC of First Cloud Layer	K Value Retrieved	Product K* IWC (3 x 4)	Emissivities		
(gm <sup>-3</sup> )	(gm <sup>-3</sup> )	(gm <sup>-3</sup> )	(m <sup>2</sup> g <sup>-1</sup> )	(m <sup>-1</sup> )	310 mb	325 mb	350 mb
0.15	0.10	0.139	.037	.0051	.705	.941	.993
0.05	0.10	0.061	.090	.0059	.681	.959	.999
0.10	0.10	0.100	.050	.0050	.681	.939	.995
							unper- turbed case

Table 3. The effect of errors in ice water content on retrieval of emissivities.

preserve the required irradiance profile. A cloud top displacement of 5 mb, equal to nearly 400 feet was input to the model. The value of K was within 12% and the cloud emissivity within 15% of the desired values. In addition, the placement of cloud top has no effect on the retrieval of emissivities or K values from the upward irradiance, if the cloud exceeds approximately 0.9 emissivity. Likewise, cloud base placement does not influence the retrieval scheme using downward irradiance for fairly thick clouds. In any case, the error in cloud boundary specification should not exceed 1 to 2 mb or approximately 100 feet for cirrus clouds.

#### 2.45 The Effect of Errors in Temperature Measurements

The expression for cloud emissivity, Eq. 4, contains no direct temperature dependence; IWC and K have no overt temperature interaction.  $\Delta z$ , the layer thickness within the cloud, does vary slightly with mean layer temperature. But basically, the cloud emissivity when computed from Eq. 4 is only a function of K, IWC, and distance into the cloud.

Cloud emissivities inferred from measured irradiances are sensitive to the accuracy of the temperature measurements even though the final emissivity profile is smoothed using Eq. 4. The model tries to match a profile of irradiances by adding just the right amount of cloud emissivity, but the irradiance contribution is the product of cloud emissivity and the  $\sigma T^4$  of the layer in question. Thus, a given change in irradiance over a given pressure interval will yield different cloud emissivity depending on the mean temperature of the layer. Consequently, the K value found by the model will be lower for a positive error in

temperature measurement and higher for an error to the cold side of the actual temperature.

A random number noise generator, similar to the one used for irradiances, was used to perturb the temperature profile. The standard deviation of the temperature perturbations was  $0.57^{\circ}\text{C}$ . The retrieved value of  $K$  was disturbed by less than 2%. Since the expected random errors in temperature measurement are on the order of  $0.2^{\circ}\text{C}$ , this temperature dependence is not critical. The effect of a systematic bias error was also explored. Such an error could arise, for instance, from calibration difficulties or in the correction for dynamic heating due to the aircraft's motion. It was found that for a bias error of as much as  $\pm 3^{\circ}\text{C}$ , the  $K$  value was disturbed by approximately  $\pm 20\%$ . A temperature bias error of not more than  $0.5 - 1.0^{\circ}\text{C}$  can normally be expected, resulting in  $K$  perturbations of less than 5%.

#### 2.46 The Effect of Errors in Water Vapor Mixing Ratio

Water vapor mixing ratio will also influence the determination of cloud emissivity and mass absorption coefficient. The model separates the emission due to water vapor from the emission due to the cloud aerosol. If, for instance, the water vapor is overestimated, the cloud contribution would be underestimated. Several tests were run using a random error in water vapor mixing ratio of up to 100%. The results indicate the rather small effect of this parameter since the  $K$  factor and emissivities at their greatest excursion were within 8% of the target values.

One ramification of this dependency is illustrated in Table 4 which shows the net gain in downward irradiance for a given cloud emissivity

(1)	(2)	(3)	(4)	(5)
Water Vapor Optical Path (ATM-CM)	Cloud Emissivity	Overlap Correction	Net Cloud Emissivity (2-3)	Net Cloud Irradiance Contribution ( $\text{wm}^{-2}$ )
0	.68134	.13011	.55123	100.55
.010	.68134	.24118	.44016	84.27
.926	.68134	.27879	.40255	76.86
1.385	.68134	.29889	.38245	73.08
1.845	.68134	.31802	.36332	69.48

Table 4. The effect of water vapor on the net gain of irradiance from a cloud.

emissivity as a function of optical path of water vapor above cloud top. It is seen that the greater the water vapor content, the less the net increase in downward irradiance. Stated in another way, a cloud with a given set of properties will have less net radiative effect in a very moist atmosphere than an identical cloud in a dry atmosphere.

#### 2.47 The Effect of Concurrent Measurement Errors

The preceding sections have described the possible errors in emissivity and mass absorption coefficient due to measurement errors in any one of the six necessary parameters. Only the one parameter under scrutiny was allowed to vary in those sensitivity tests. All of the other five variables were held constant at their unperturbed values. In this final sensitivity test, all six parameters were allowed to vary concurrently in a random manner during 600 separate computations. The magnitudes of the allowed variations were equal to the expected precision of the data as outlined in Table 6. Table 5 gives the response of the cloud emissivity to these concurrent errors. The values given are the limits such that 90% of the 600 cases computed had percentage emissivity errors not larger than the indicated values at the given depth below cloud top. It can be seen that the greatest percentage errors occur at the smallest depths into the cloud. When the cloud has reached an emissivity of 0.95, the percentage errors are very small, indicating very little uncertainty. The absolute uncertainty in terms of emissivity is also given in Table 5. The maximum uncertainty in 90% of the cases was not greater than  $\pm .12$  at any level and for emissivities greater than .95 was less than  $\pm 0.02$ .

Depth Below Cloud Top		Percentage Emissivity Error	Absolute Emissivity Error
(mb)	(meters)	(90% confidence limits)	(90% confidence limits)
5	150.9	$\pm 29\%$	$\pm .05$
10	299.0	$\pm 25\%$	$\pm .09$
15	444.5	$\pm 21\%$	$\pm .12$
20	587.6	$\pm 17\%$	$\pm .12$
25	728.5	$\pm 14\%$	$\pm .10$
30	867.4	$\pm 11\%$	$\pm .08$
40	1139.2	$\pm 5\%$	$\pm .04$
50	1403.0	$\pm 3\%$	$\pm .02$
60	1659.5	$\pm 2\%$	$< \pm .02$
70	1908.7	$< \pm 2\%$	$< \pm .02$

Table 5. Errors in emissivity as a function of depth below cloud top for concurrent measurement errors.

The mass absorption coefficients were found to vary over a much wider range, as expected. 90% of the 600 cases were within  $\pm 60\%$  of the desired value. This is due primarily to the uncertainty in ice water content as discussed in Section 2.43.

#### 2.48 Summary of Sensitivity Testing

The sensitivity testing of IRADLON-2 has shown that the input requirements are comparable to the expected quality of the available real data. Temperature and moisture measurements are quite accurate and the use of climatological data where measurements are not available should be sufficiently accurate to preclude difficulty. Uncertainties in emissivities and K values should be 3% or less. Cloud top and base data from observer's notes can normally be relied upon to 100 feet. Emissivities and K values within 1% are, therefore, expected. Ice water content is seen to be critical to the determination of the mass absorption coefficient. The inverse relationship means that any percentage error in IWC will be matched by an equal percentage error of opposite sign in the K value. This difficulty does not afflict the emissivities derived from the K value. Since the  $K * IWC$  product is nearly conserved, emissivities will be accurate to a few percent. The expected precision of the IWC data is listed as  $\pm 40\%$  in Table 6. This figure applies to the data as analyzed using the technique described in the Appendix. The uncertainty is due mainly to the necessity of assuming a crystal shape. (See Table A2). The possible effect of numerous undetected small particles, as discussed in Section 3.4 have not been considered in Table 6. The measured irradiances will yield K values and emissivities to within 4% if only random instrumental error is

considered. The effects of concurrent measurement errors in all six relevant variables will result in emissivities within  $\pm .12$  and K values within  $\pm 60\%$ . Table 6 summarizes the results of the sensitivity testing.

Parameter	Expected Precision of Data	Resulting Emissivity	Errors K
Irradiance (Random errors)	$\pm 2 \text{ } \mu\text{m}^{-2}$	$\pm .01$	$\pm 4\%$
Irradiance (Bias errors)	$\pm 5 \text{ } \mu\text{m}^{-2}$	$\pm .05$	$\pm 12\%$
Cloud top and base pressure	$\pm 1.5 \text{ mb}$	$\pm .03$	$\pm 3\%$
Temperature	$\pm 0.5^\circ\text{C}$	$\pm .02$	$\pm 3\%$
Water vapor mixing ratio	$\pm 10\%$	$< \pm .01$	$< \pm 1\%$
Ice water content	$\pm 40\%$	$\pm .03$	$\pm 40\%$
Maximum cumulative error (90% confidence limits)		$\pm .12$	$\pm 60\%$

Table 6. Summary of sensitivity tests.

### 3.0 APPLICATION OF IRADLON-2 TO GATE SABRELINER DATA

The radiative transfer model IRADLON-2 is used to analyze data collected by the National Center for Atmospheric Research Sabreliner during the GARP Atlantic Tropical Experiment (GATE) in the summer of 1974. Values of mass absorption coefficient, cloud emissivity and cooling rates are derived for specific cases.

#### 3.1 Description of Data Available

The following parameters which were either measured directly or derived from measured quantities were used in the analysis:

- Time
- Ambient Temperature
- Dew Point Temperature
- Static Pressure
- True Air Speed
- True Heading
- Downward Longwave Irradiance
- Upward Longwave Irradiance
- Particle Spectra

In addition, the following information was intermittently available from the aircraft's Inertial Navigation System (INS):

- Latitude
- Ground Speed
- Longitude
- Wind Vector Components
- Pitch
- Yaw
- Roll

While these INS data are not essential to the analysis, they were helpful in visualizing flight track, aircraft attitude and winds aloft. It

was also used to verify the position of the start and end points of the various sampling flight legs and the location of these flight legs relative to one another.

### 3.2 Reduction and Analysis of Data

Broadband longwave hemispheric irradiance data were collected by one upward- and one downward-facing Eppley Precision Infrared Radiometer (Pyrgeometer). This instrument responds to radiation in the 4-50  $\mu\text{m}$  spectral range. A description of the Sabreliner radiation system and details of the radiation data reduction procedures are given by Albrecht and Cox (1976a). Detailed reports on the operating characteristics, calibration procedures and theory of operation of pyrgeometers may be found in Albrecht et al. (1974) and Albrecht and Cox (1976b).

#### 3.21 Radiation and State Variable Sampling

Basically, the values of pressure, temperature, dew point and long-wave irradiance for any given level in the atmosphere were obtained from averaging 1 sec values on straight and level data collection flight legs. These sampling flight legs varied in length on different days from 14 minutes (approximately 170 km) to as little as 1 minute 15 seconds (approximately 15 km). However, all data collection flight legs that are used to construct any given vertical profile are of similar length. As mentioned before, climatological values of pressure, temperature and moisture in accord with Figure 1 were used to fill in the atmosphere above and below the sampling flight legs. For in-cloud data flight legs at these very cold temperatures, ( $-60^{\circ}\text{C}$  to  $-30^{\circ}\text{C}$ ) the air was assumed to be at saturation with respect to ice. Upward and downward irradiance and blackbody irradiance at ambient temperature vs. pressure is graphed.

### 3.22 Ice Water Content Sampling

Ice water content values were derived from data collected by a one-dimensional optical array particle spectrometer built by Particle Measuring Systems, Inc. of Boulder, Colorado. This instrument, commonly known as the Knollenberg Probe, counts and sizes cloud particles into 15 equally spaced size channels in the nominal range of 20 $\mu\text{m}$  to 300 $\mu\text{m}$ . A good operational description of this instrument is given by Knollenberg (1970, 1973). The Appendix provides a more complete description of the reduction process used for obtaining ice water contents.

### 3.23 Cloud Top and Base Determination

Cloud top and cloud base were determined using both observer's notes and Knollenberg Probe data. The pressure level at which the spectrometer first transitioned from clear to cloud or vice versa was used as cloud top or base as appropriate. This was checked against observer's notes to assure consistency.

There is one serious limitation of any method of determining cloud emissivities. It is necessary to obtain an irradiance measurement outside of the cloud to define the starting point. For the downward irradiance stream a measurement above cloud top is required and for the upward irradiance, a measurement below cloud base is needed.

A test case was prepared using the atmosphere of Figure 1 with a cloud between 300 mb and 400 mb and an IWC of 0.1  $\text{gm}^{-3}$ . The value of K in Eq. 3 was varied and the change in upward flux at 2 levels in the cloud was monitored. Figure 6 illustrates the results. The curve for the 390 mb level (only 187 m into the cloud) shows that a 1  $\text{wm}^{-2}$  change in upward irradiance can be produced by a K change of approximately .001  $\text{m}^2\text{g}^{-1}$ . The 350 mb curve (974 m into the cloud) requires a K change

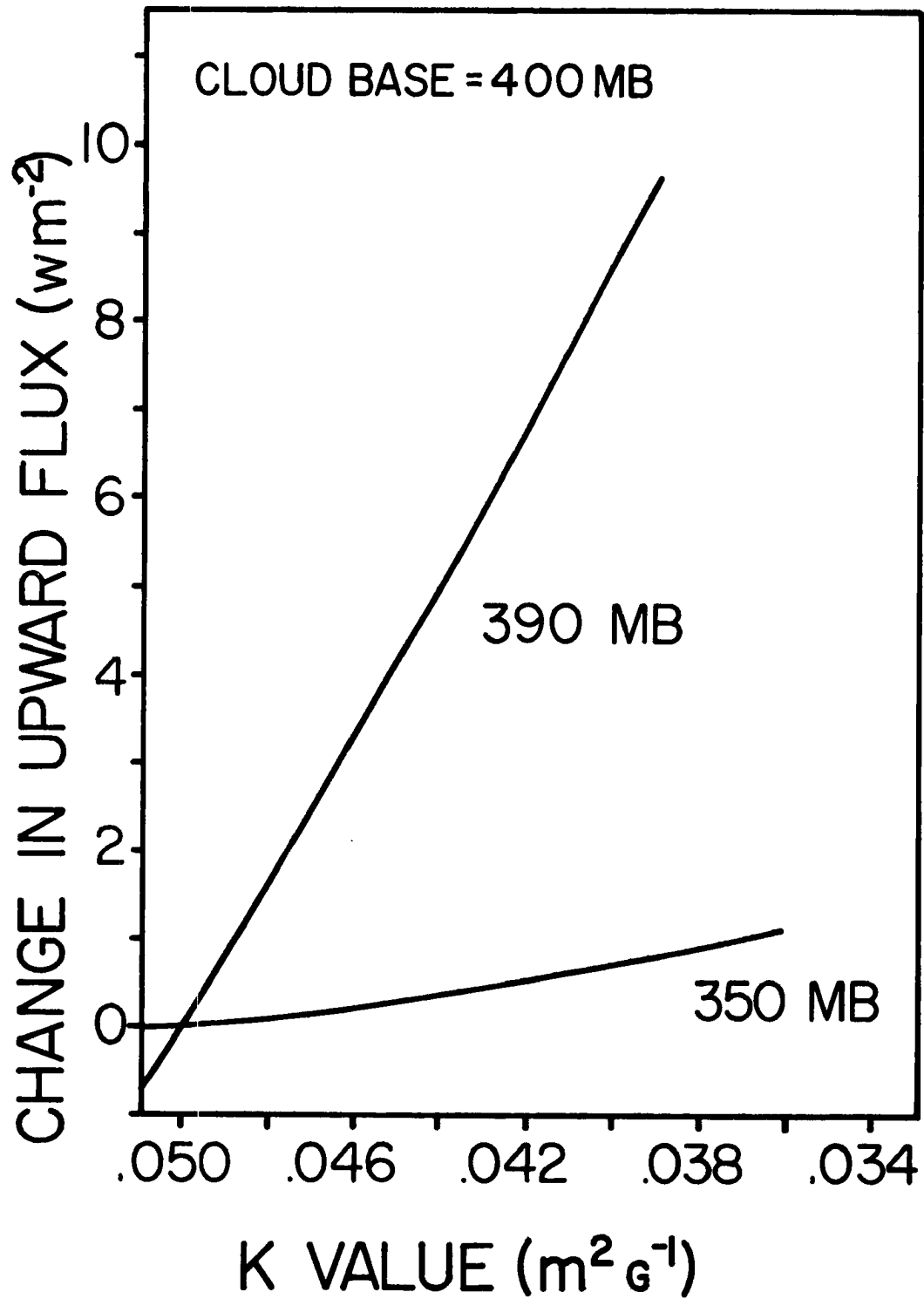


Figure 6. Change in upward flux as a function of K value for 2 levels in the cloud.

of  $.013 \text{ m}^2\text{g}^{-1}$  to produce the identical  $1 \text{ wmm}^{-2}$  change in upward irradiance. Therefore, the uncertainty in the emissivity profile is 13 times greater for the 350 mb level than for the 390 mb level for a random error in irradiance measurement of only  $1 \text{ wmm}^{-2}$ . The same argument applies to the downward irradiance regime. One ramification of this phenomenon is that in order to derive an emissivity profile and the K value that describes it, measurements must be obtained at levels at which the cloud has not yet achieved blackness.

A physical understanding of why this is true may be gained by examining the transmitted term in the upward irradiance. At the 390 mb level, the transmitted term is still contributing about 17% of the upward irradiance. This portion is rapidly changed as the cloud emissivity changes. Referring to Eq. 1, it may be seen that any incremental change in emissivity changes the upward irradiance by substituting  $\sigma T^4$  of the surface for  $\sigma T^4$  of the layer in question. Once the total atmospheric emissivity approaches 1.0 and forces the transmitted term toward zero, upward irradiance can be modified only by rearranging the emissivity profile relative to the temperature profile. This is a very much less responsive procedure as the curve for 350 mb in Figure 5 shows.

For the downward irradiance there is no transmitted term. The sensitivity to position in the cloud arises from the fact that total atmospheric emissivity is less than 1.0 until reaching the cloud. Hence, downward irradiance increases rapidly as cloud emissivity forces total atmospheric emissivity towards 1.0. As the increase in total emissivity slows to an asymptotic approach to 1.0, the mechanism for affecting changes in downward irradiance shifts to rearranging the emissivity distribution relative to the temperature profile. This latter process is

quite slow and insensitive in bringing about substantial changes in downward irradiance.

For the cases studied here, measurements below cloud base were not obtained thus, the upward irradiance measurements are not useful for determining emissivities. They were, however, used for cooling rate calculations.

### 3.24 Variability of IWC and Downward Irradiance

Important information was gathered on these flights regarding the horizontal variability of IWC in a cirrus layer. It may be expected that downward longwave irradiance would be strongly modulated by and highly correlated with the variations in IWC. In addition, if it is proper to integrate layer values of IWC ( $\text{gm}^{-3}$ ) in the vertical to obtain column water content ( $\text{gm}^{-2}$ ) then the correlation of IWC with  $H\downarrow$  should be as good deep inside the cloud layer as it is near cloud top.

Figure 7 shows the variation with time and distance of IWC and  $H\downarrow$  on the flight leg at 35,000 feet on Day 226. This is approximately 1 kilometer below cloud top. The IWC varies by large amounts from a minimum of  $0.001 \text{ gm}^{-3}$  to  $0.09 \text{ gm}^{-3}$ . The downward irradiance shows excellent correlation with the IWC, as expected.

Figures 8 and 9 depict the same relationship for the flight legs at 40,000 feet (0.1 km below cloud top) and 36,000 feet (1.4 km below cloud top) respectively on Day 232. The IWC varies from zero to a maximum of  $0.04 \text{ gm}^{-3}$ . The correlation of IWC with  $H\downarrow$  is very good at both levels, confirming that vertical integration of layer IWC is appropriate.

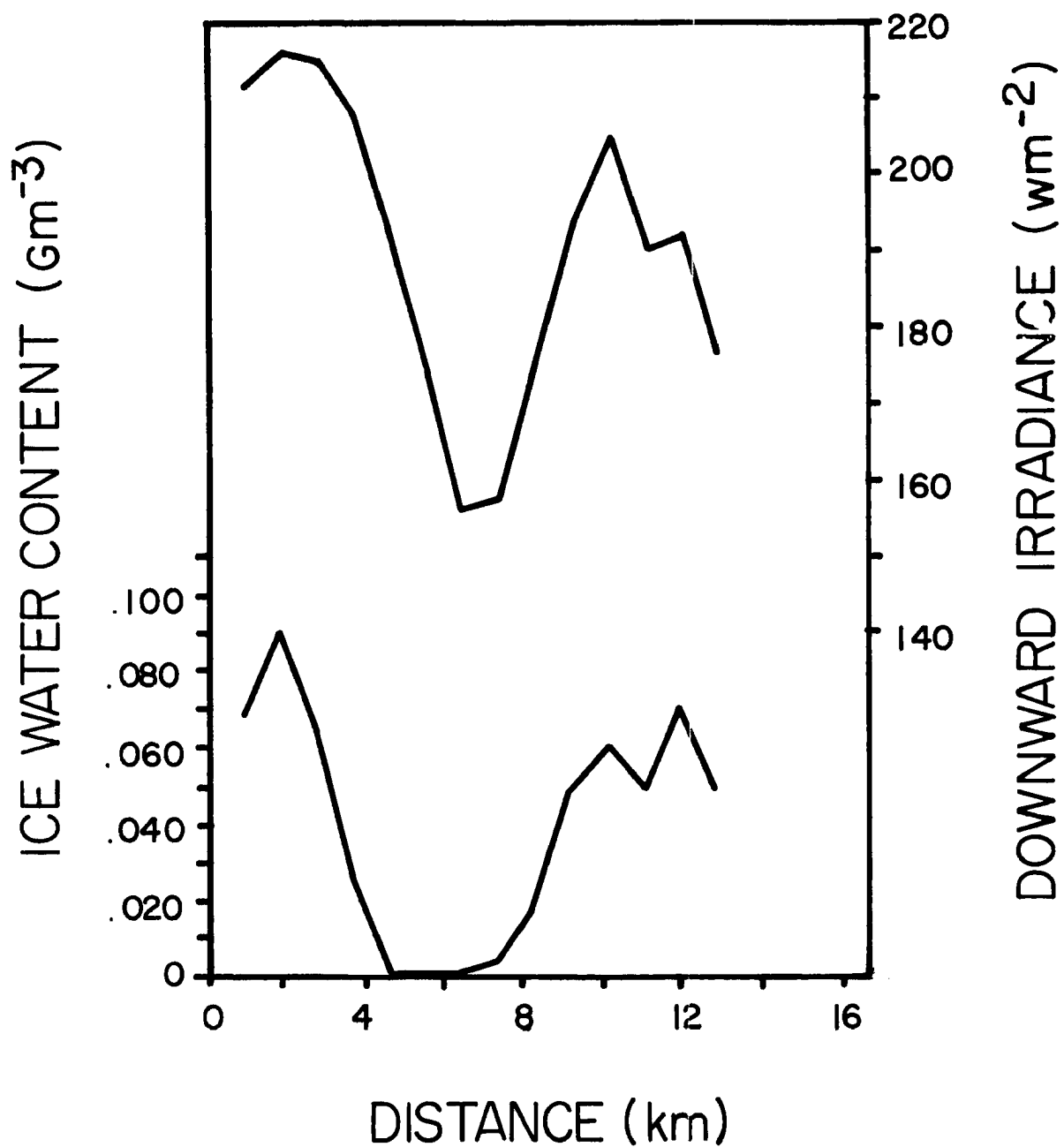


Figure 7. Simultaneous measurements of downward irradiance and ice water content vs. distance for Day 226, 35,000 feet.

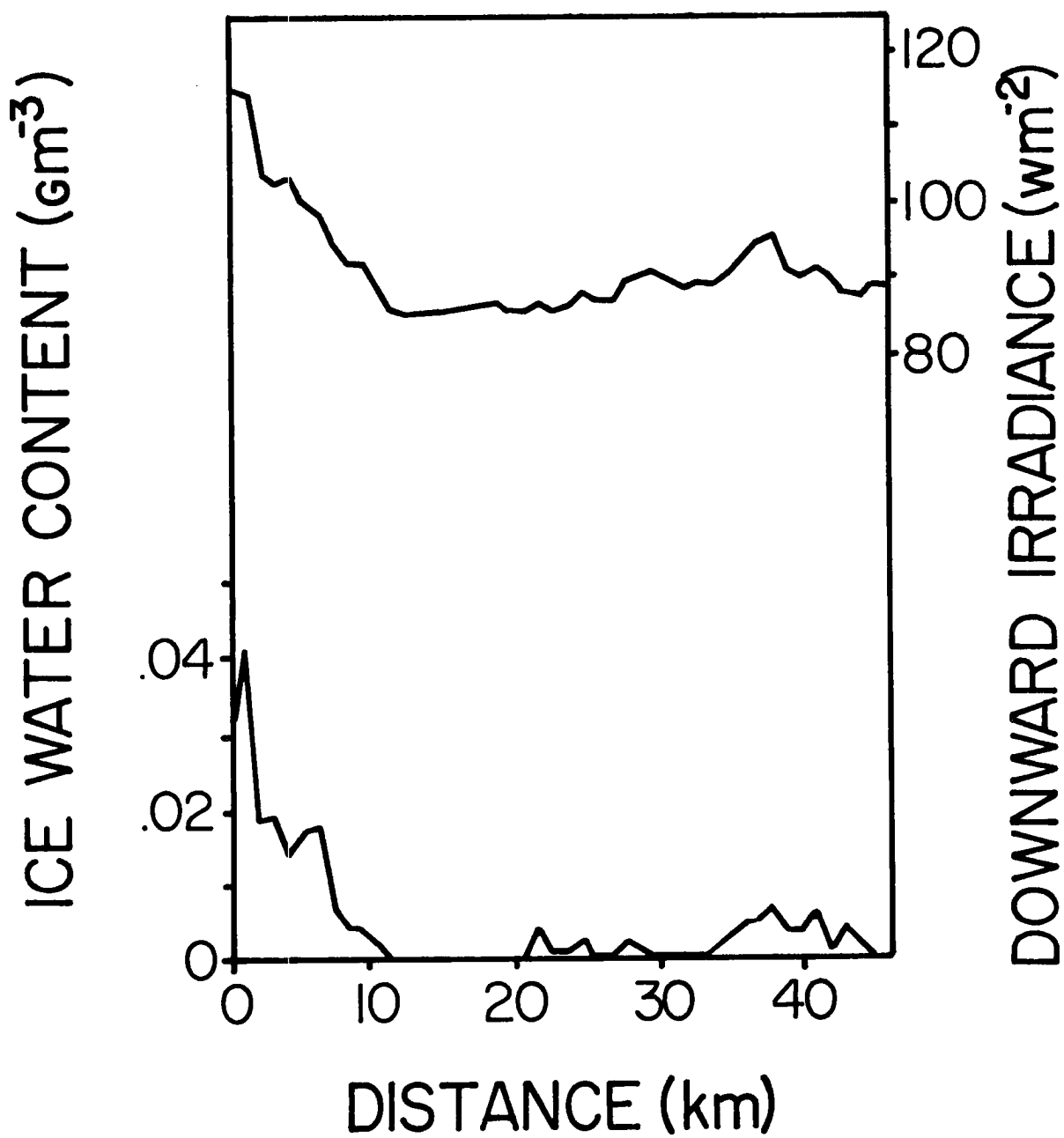


Figure 8. Simultaneous measurements of downward irradiance and ice water content vs. distance for Day 232, 40,000 feet.

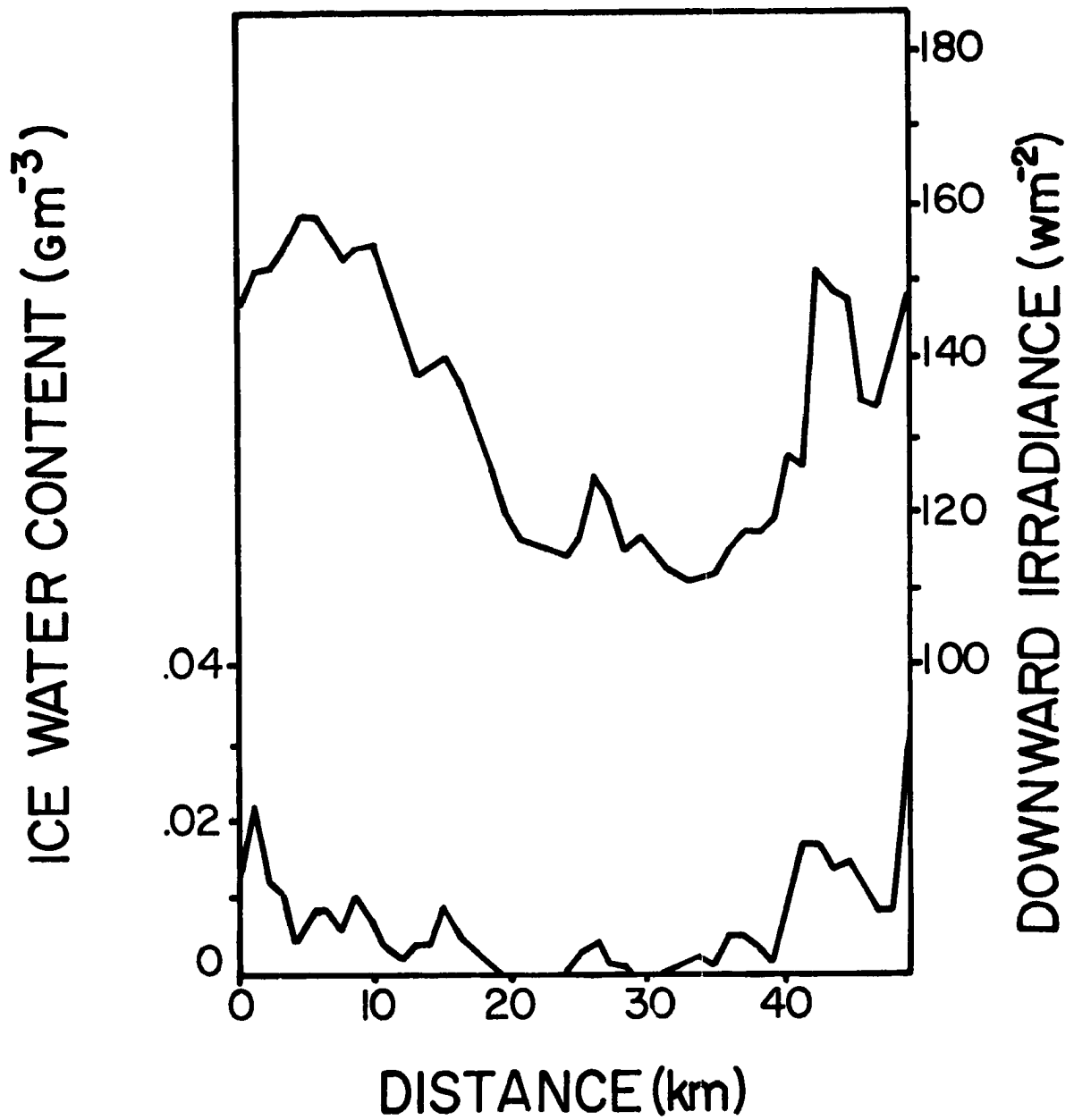


Figure 9. Simultaneous measurements of downward irradiance and ice water content vs. distance for Day 232, 36,000 feet.

### 3.25 Cirrus Cloud Particle Size Distribution

Typical size distributions for 3 separate flight legs, assuming that the particles are hexagonal columns of 4:1 ratio, are shown in Figure 10. The same information is depicted in Figure 11, but here the particles are assumed to be bullet rosettes. Figures 10 and 11 display only the number of actual measured particles as a function of final corrected crystal size. No extrapolated data are included. The reader should consult the Appendix for information on the extrapolation correction applied to this data to obtain total IWC. In addition, an alternative extrapolation scheme is discussed in Section 3.4. Displayed in each figure are two flight legs on Day 232, one at 40,000 feet and one at 36,000 feet; and one flight leg on Day 251 at 42,000 feet. The variation from one level to another is shown by the two flight legs on Day 232 and the variation from day to day is shown by the distribution for Day 251. In both figures the curves have been normalized to the same total number of particles so that the spectra may be more directly compared. There is apparently very little difference from day to day or from one level to another on the same day. The main differences in IWC, and therefore longwave radiative properties, are due to the different concentrations of particles.

The data are presented separately for the two crystal shapes that were assumed to be present. The Appendix explains how this size distribution information was converted to IWC. The figures should be interpreted with caution since the size refers to the crystal length for the columns and crystal diameter for the rosettes. Sketches of these particle shapes are found in Figures A1 and A2 of the Appendix. The distribution used to calculate IWC is really a superposition of the

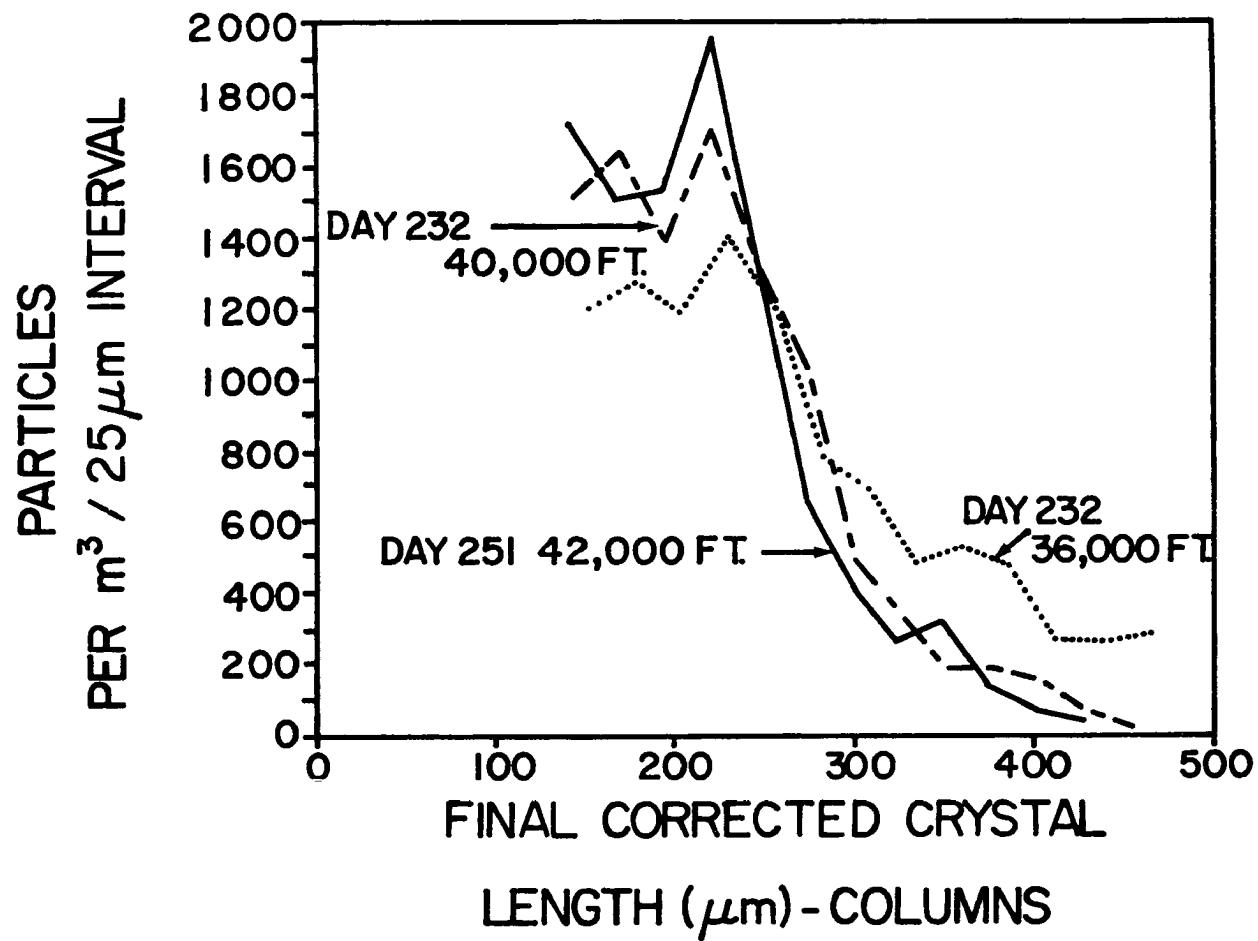


Figure 10. Measured particle size distribution for three data flight legs with total number of particles normalized to 10,000 per cubic meter and for assumed column shape.

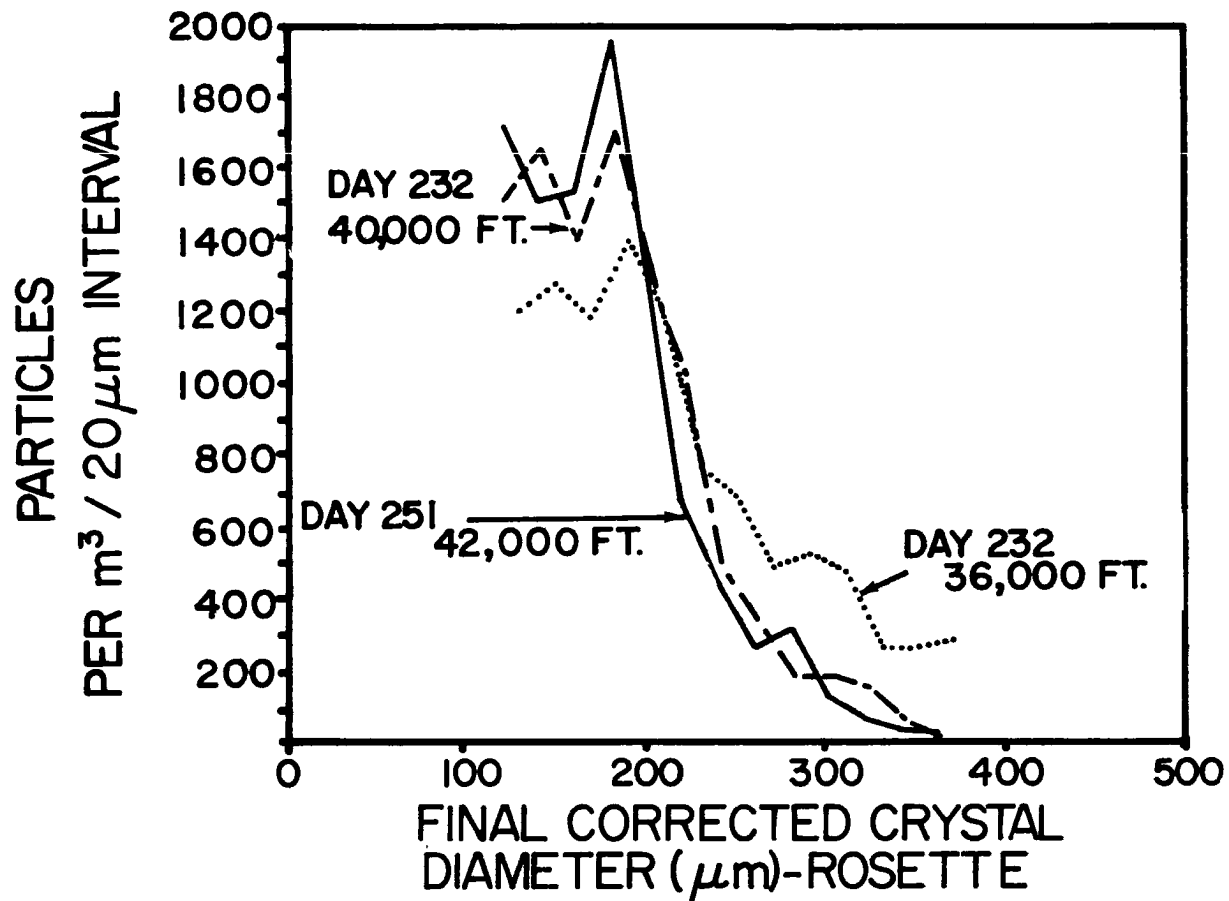


Figure 11. Measured particle size distribution for three data flight legs with total number of particles normalized to 10,000 per cubic meter and for assumed rosette shape.

curves representing columns and rosettes. However, the abscissas of Figures 10 and 11 are not really identical.

Although it appears that the size distribution may contain a significant number of particles below the lower limit of the Knollenberg Probe, these small particles contribute very little to the total IWC, for the extrapolation that has been used. This is illustrated in Appendix Figures A4 and A5 which show the relationship of IWC vs. particle size and the corresponding size distribution.

### 3.3 Case Studies

The model IRADLON-2 described in Section 2 was used to analyze the data collected by the NCAR Sabreliner. Three flights that appeared to contain all the necessary information were studied.

#### 3.31 Day 226 - August 14, 1974

This set of sampling flight legs were conducted on a high cirrus layer at 9 levels ranging from 40,000 feet to 30,000 feet. The pattern consisted of straight and level flight legs through the sampling area followed by descending 180° turns to the next altitude. The data flight legs were of 80 seconds average length. None of the 10 sampling flight legs succeeded in getting below cloud base, hence the upward irradiance cannot be used for emissivity computations. Figure 12 depicts the profile of ice water content, with actual measured points indicated. The Appendix details the assumptions made in deriving ice water content. Figure 13 shows the measured profile of upward and downward irradiances with the blackbody curve shown for reference. Also shown is the irradiance profile for a clear sky to add perspective to the measured irradiances. There were some obvious problems with the

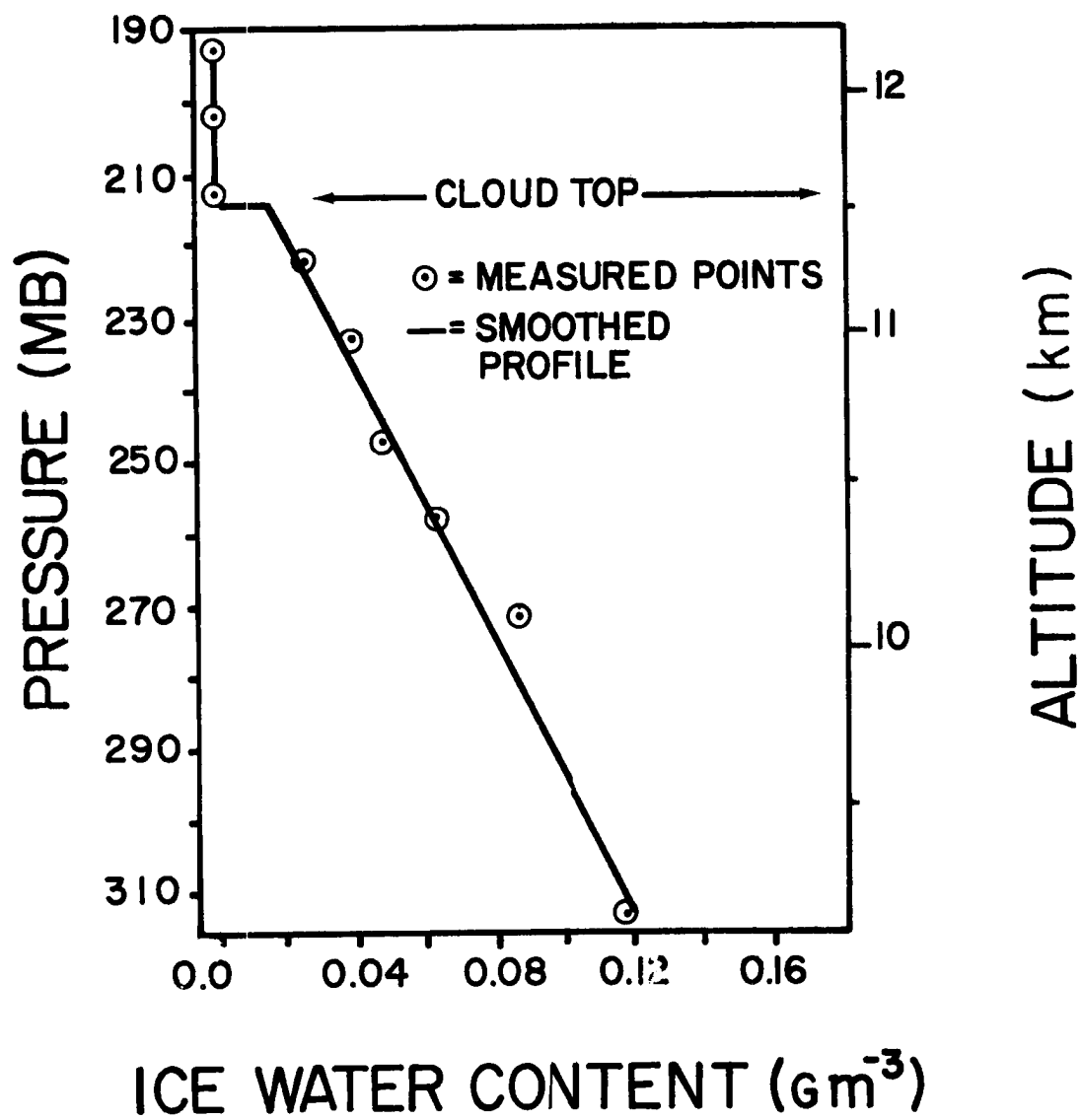


Figure 12. Vertical profile of IWC for Day 226.

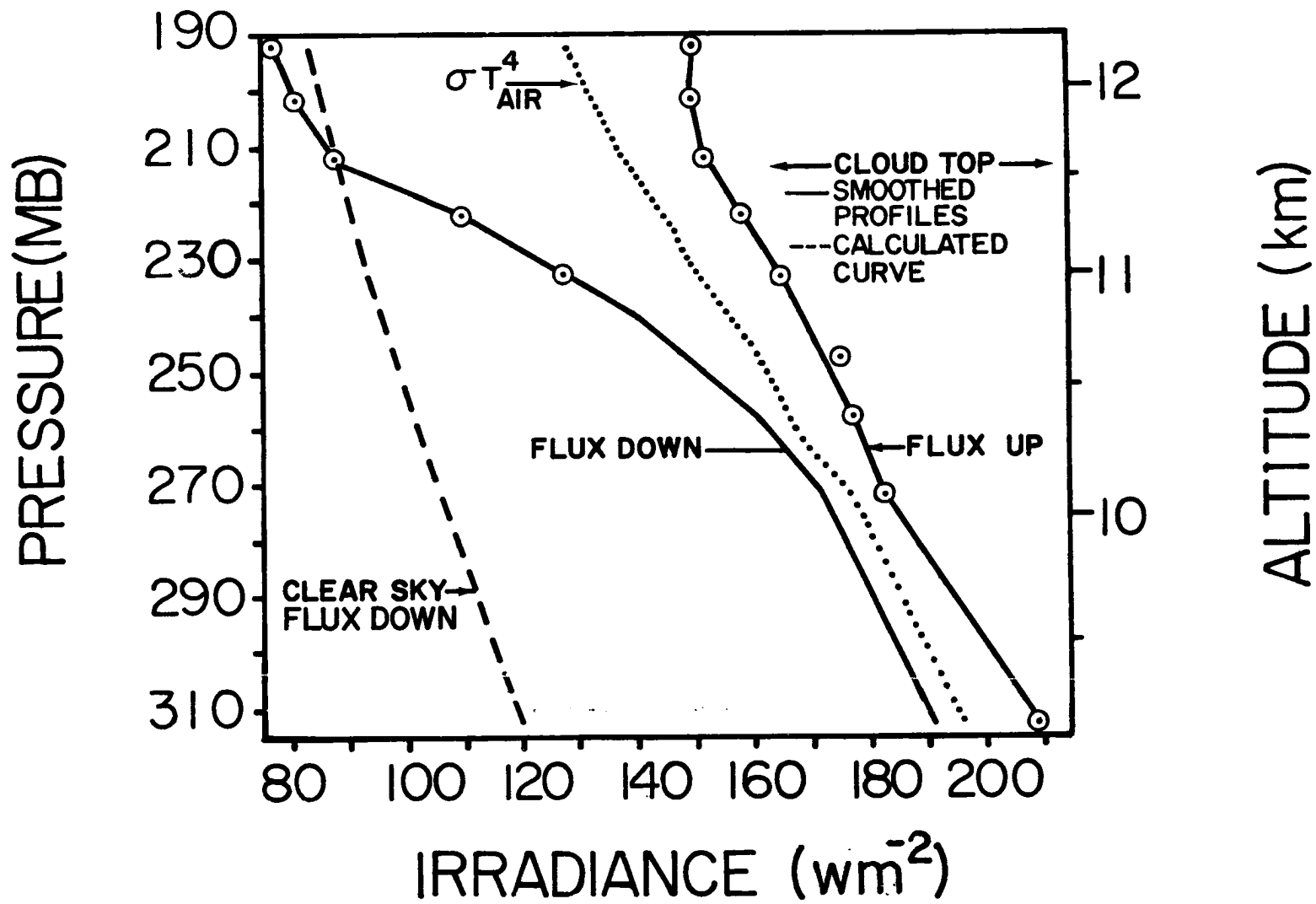


Figure 13. Day 226 irradiance profiles.

downward irradiance since it exceeded blackbody radiation at all points below 36,000 feet. Instrumental problems were undoubtedly at fault since nothing in the meteorological situation would allow such an irradiance profile. It was assumed that the undefined problem affected only those points measured after the flight leg at 36,000 feet. The model was run using the 5 levels obtained before that time and an extrapolation of the curve down to the lowest measured level. Three test cases were examined to explore what effect the placement of this extrapolation of the downward irradiance curve would have on the determination of the K value. The test irradiance profiles ranged from within  $1 \text{ wm}^{-2}$  to as much as approximately  $20 \text{ wm}^{-2}$  away from the blackbody curve. These extremes correspond closely to the maximum and minimum of the envelope of reasonable values described in Section 2.42. The K values obtained varied from  $0.108 \text{ m}^2\text{g}^{-1}$  to  $0.064 \text{ m}^2\text{g}^{-1}$ . This is not a very great range for such widely different irradiance profiles. This is further evidence confirming the statement made in Section D that the choice of the K parameter is driven primarily by the points above the level at which the cloud achieves radiative blackness.

The K value deduced from this downward irradiance data for Day 226 is  $0.076 \text{ m}^2\text{g}^{-1}$ . Figure 14 depicts the emissivity values as a function of distance below cloud top. Given the possibility of concurrent measurement errors of magnitudes as outlined in Table 6, the 90% confidence limits are shown by the dashed line envelope. For comparison purposes, a curve obtained from the theoretical calculations of Hunt (1973) is shown. This curve uses Hunt's Table 2(i) for ice spheres of  $50\mu\text{m}$  modal radius with the optical depth vs. distance below cloud top relation derived from the IWC profile of this specific case. Hence,

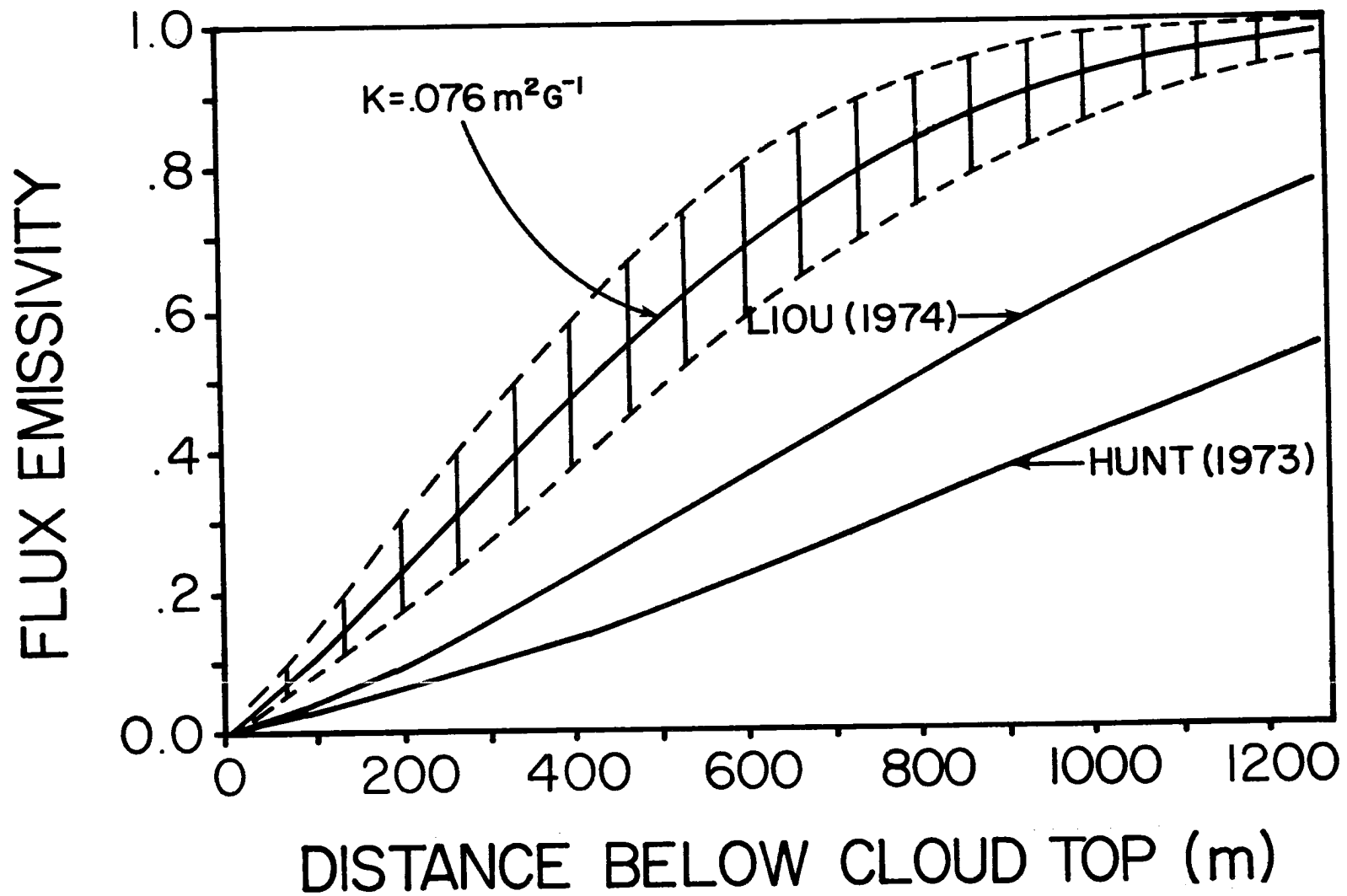


Figure 14. Day 226 emissivity vs. distance below cloud top with comparisons to theoretical studies of Hunt (1973) and Liou (1974).

the curves are directly comparable on the question of total column water content as a function of distance below cloud top. The Hunt curve shows a lower emissivity than the measured case at all depths into the cloud. There are several possible explanations for this disagreement. The most likely relates to the difference in extinction coefficient for spherical particles as opposed to the irregularly shaped columns, bullet rosettes or other crystalline forms found in real cirrus. Hunt assumes spherical ice particles in compiling his tables. However, it is pointed out by Liou (1974) that the extinction cross section for cylinders is about 1.5 times greater than for spheres of the same volume. Of course, optical depth is directly proportional to this extinction coefficient. A factor of approximately 5 would bring the Hunt curve reasonably close to agreement with the measured curve. This large an extinction efficiency factor is not inconceivable considering the probable mix of cirrus crystal forms and their large range of sizes compared to the sizes assumed by Hunt and Liou.

A second comparison curve is shown which is derived from the work of Liou (1974). This curve was obtained by deriving a mass absorption coefficient from Liou's Figure 6, converting it for use with a flux emissivity relation and applying the IWC profile of Day 226. Hence, as with the Hunt comparison curve, total column water content as a function of distance below cloud top is identical to the measured case. The Liou curve lies between the present measurements and the Hunt curve, presumably due to the larger extinction coefficients used by Liou.

Figure 15 depicts emissivity as a function of the total water content in the column above the point of measurement. This column water

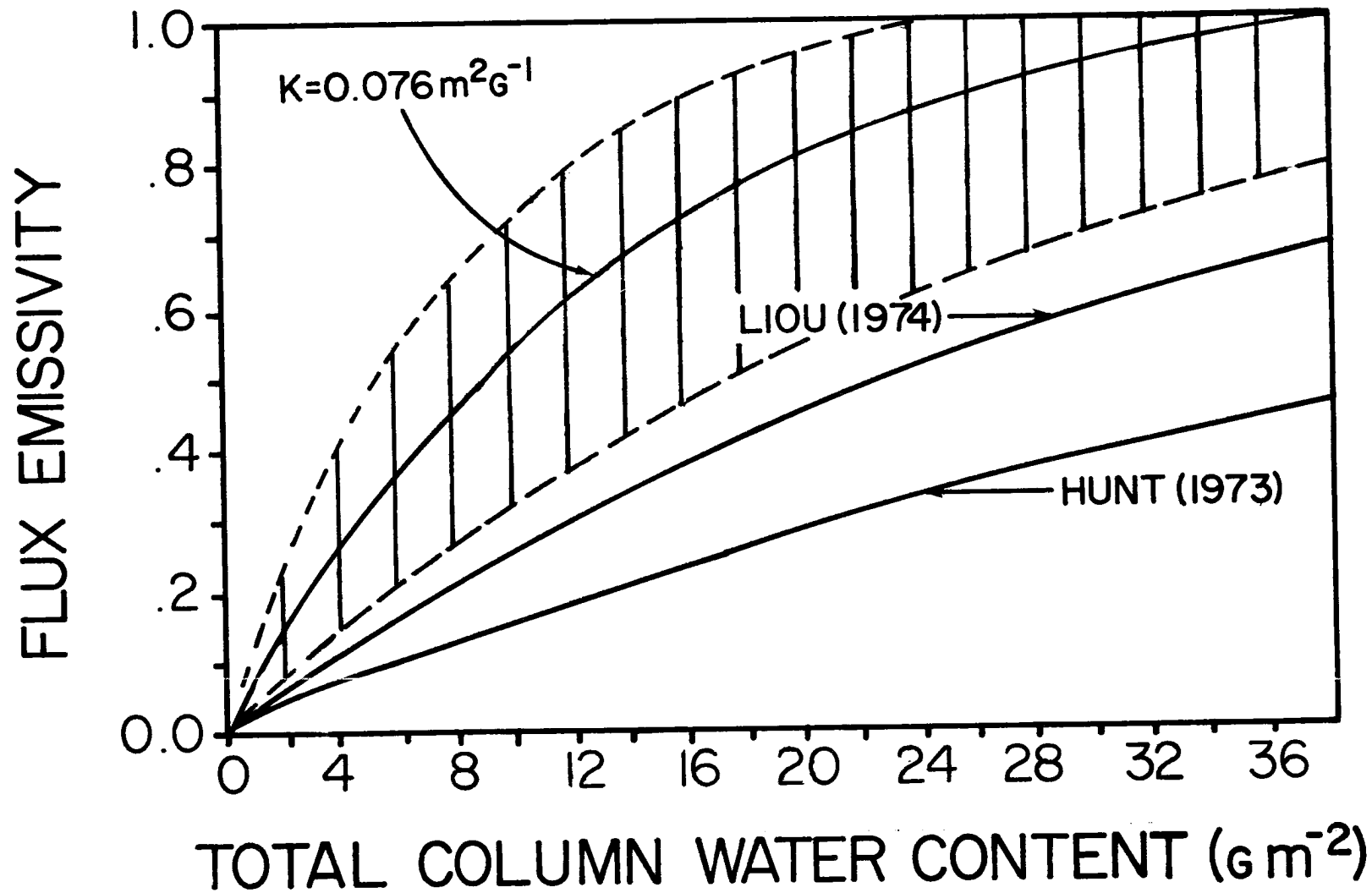


Figure 15. Day 226 emissivity vs. total column water content with comparisons to Hunt (1973) and Liou (1974).

content ( $\text{gm}^{-2}$ ) is simply a vertical integration of the ice water content ( $\text{gm}^{-3}$ ). The reader should consult the Appendix for a discussion of the assumptions made in deriving ice water content. In addition, some ramifications of alternative assumptions on derived ice water content are discussed in Section 3.4. The dashed line envelope indicates the region within which 90% of the emissivity values would lie given the possibility of concurrent measurement errors of magnitudes as outlined in Table 6. Comparison curves obtained from Hunt (1973) and Liou (1974) are displayed. Again, both theoretical curves are substantially lower than the measured values. This indicates that the naturally occurring cirrus crystals must have greater extinction efficiencies than the spherical ice crystals of Hunt or the uniform cylinders of Liou.

The possibility was considered that significant IR reflectivity of the cloud could be augmenting the downward irradiance and producing this discrepancy between theory and observations. We assume here that the cloud reflectivity is the same for both the upward and downward irradiance. The net gain in the downward irradiance is equal to the difference between the upward irradiance and the downward irradiance multiplied by the reflectivity factor. When there is little difference between the two, as in these cases (see Fig. 13), there can be little net gain in the downward for typical cloud reflectivity of 5% or less. Clearly, this effect can be important in some situations such as at the base of dense cirrostratus with a warm underlying surface. Feigel'son (1970) and Platt (1977) have noted that downward IR radiation from such a cloud can exceed blackbody radiation at the cloud temperature if the cloud reflectivity is not taken into account.

Heating rate as a function of pressure is displayed in Figure 16. The smoothed curve is computed from the irradiances generated by the K value retrieved by the model. The K value was derived from the downward irradiances only, as discussed previously. However, that same K value was used to generate the smoothed upward fluxes. This demonstrates that the derived mass absorption coefficient produces reasonable results for the upward irradiance, as would be expected. The observed layer heating rates are represented by vertical bars. They are obtained from the actual measured upward and downward irradiances at 5 levels. Figure 13 indicates the 5 levels where both upward and downward irradiances were obtained. The measurements show good qualitative agreement with the calculations. The measured heating rates above cloud top are relatively constant, as expected. The first layer in the cloud shows a cooling maximum of approximately the proper magnitude followed by decreased cooling deeper into the cloud.

The general profile of heating rate is modified very little by the choice of the K value for downward irradiance. Figure 17 displays heating rate as a function of pressure for Day 226 for two different K values. The two K values represent the envelope of the most likely extremes of K value. There are several interesting features of these profiles. First, above cloud top the heating rates are identical. This occurs because the downward irradiance has not yet been affected by the cloud and the upward irradiance is nearly constant. Upon entering the cloud, the higher K value, representing a more dense cloud, produces greater cloud top cooling. However, slightly farther into the cloud the curves cross and greater cooling is maintained by the lower K value. This occurs because the higher K produces a sharper increase of downward

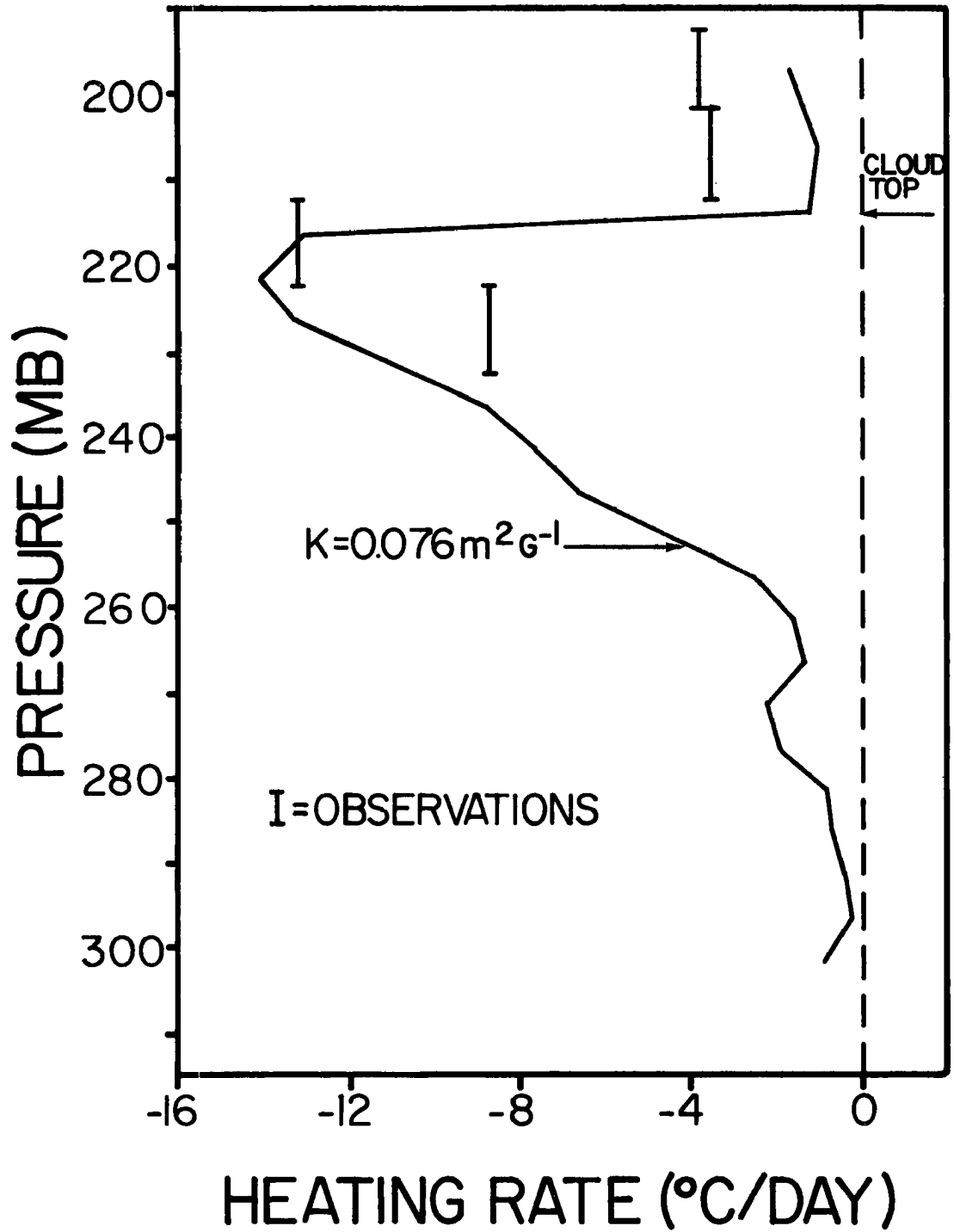


Figure 16. Heating rate as a function of pressure, Day 226.

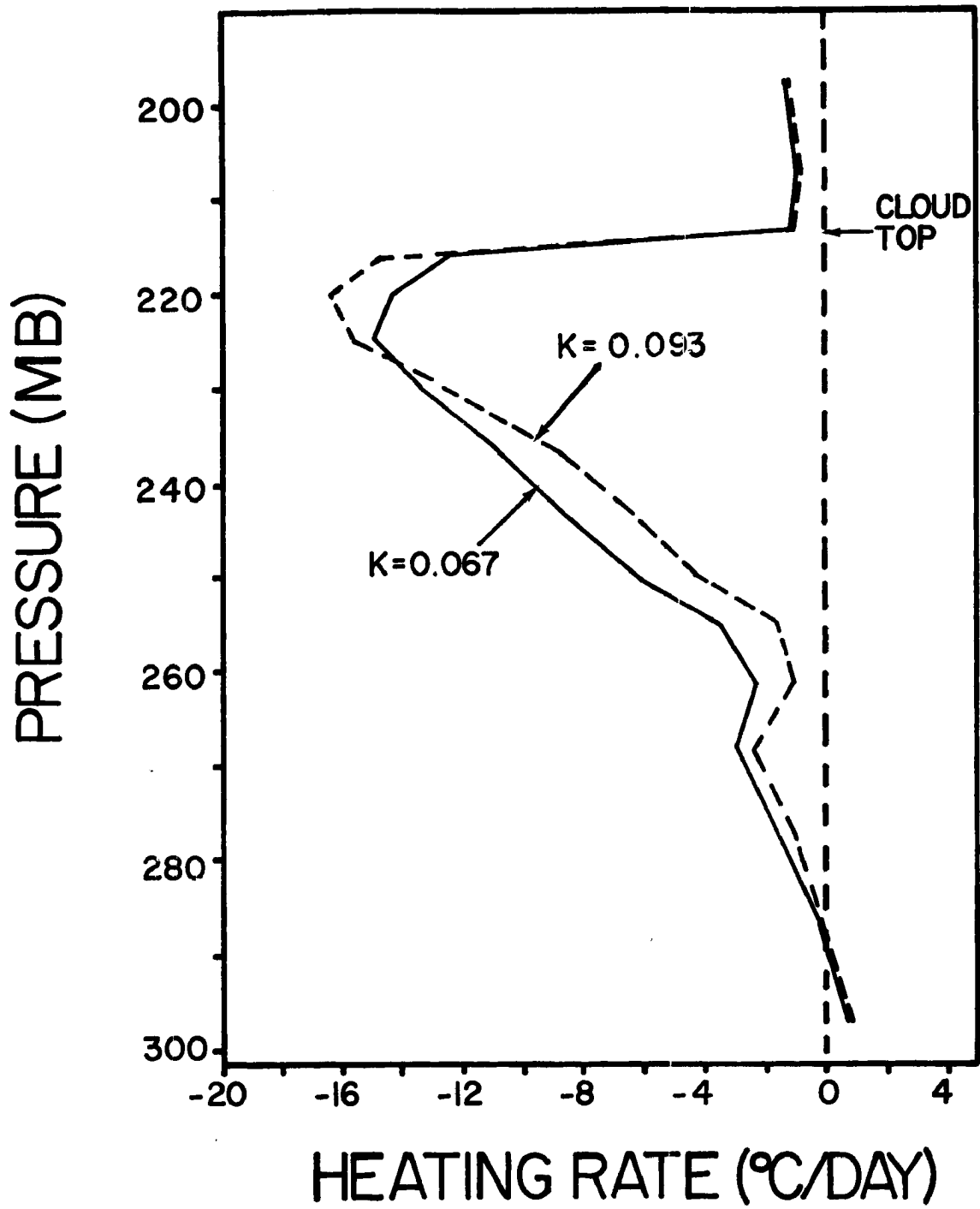


Figure 17. Comparison of effect of different K values on heating rate, Day 226.

irradiance upon entering the cloud. The lower K increases less rapidly at first but its rate of increase soon becomes larger than for the higher K. In addition, for thick clouds such as these, conservation of energy dictates that the total cloud layer cooling be approximately the same for both K values. Therefore, if the higher K cools more in the top of the layer, it must cool less deeper inside the layer. Near the lowest part of the cloud layer the two curves converge, signifying that the downward irradiance has begun to parallel the blackbody irradiance curve. The choice of K value is then insignificant in determining the cooling rate.

### 3.32 Day 232 - August 20, 1974

This sampling area contained a very tenuous, patchy cirrus cloud. There were 6 data flight legs, at 2,000 foot intervals from 42,000 to 32,000 feet. The first four flight legs were flown in a race track pattern. Straight and level flight legs through the area were followed by descending 180° turns to the next altitude. The final two flight legs were interrupted due to air traffic control considerations but sufficient data was gathered to make them useful. The runs averaged 3.5 minutes in length (approximately 45 km). Observer's notes indicate the very thin nature of the cloud since the African coast line was visible during part of the sampling time. An irradiance measurement clearly above cloud top was obtained on the 42,000 foot run but descent clearly below cloud base was not achieved. INS data were not available on this flight. The vertical profile of IWC, derived under the assumptions described in the Appendix, is shown in Figure 18. It shows no coherent pattern such as was found on Day 226. This further indicates

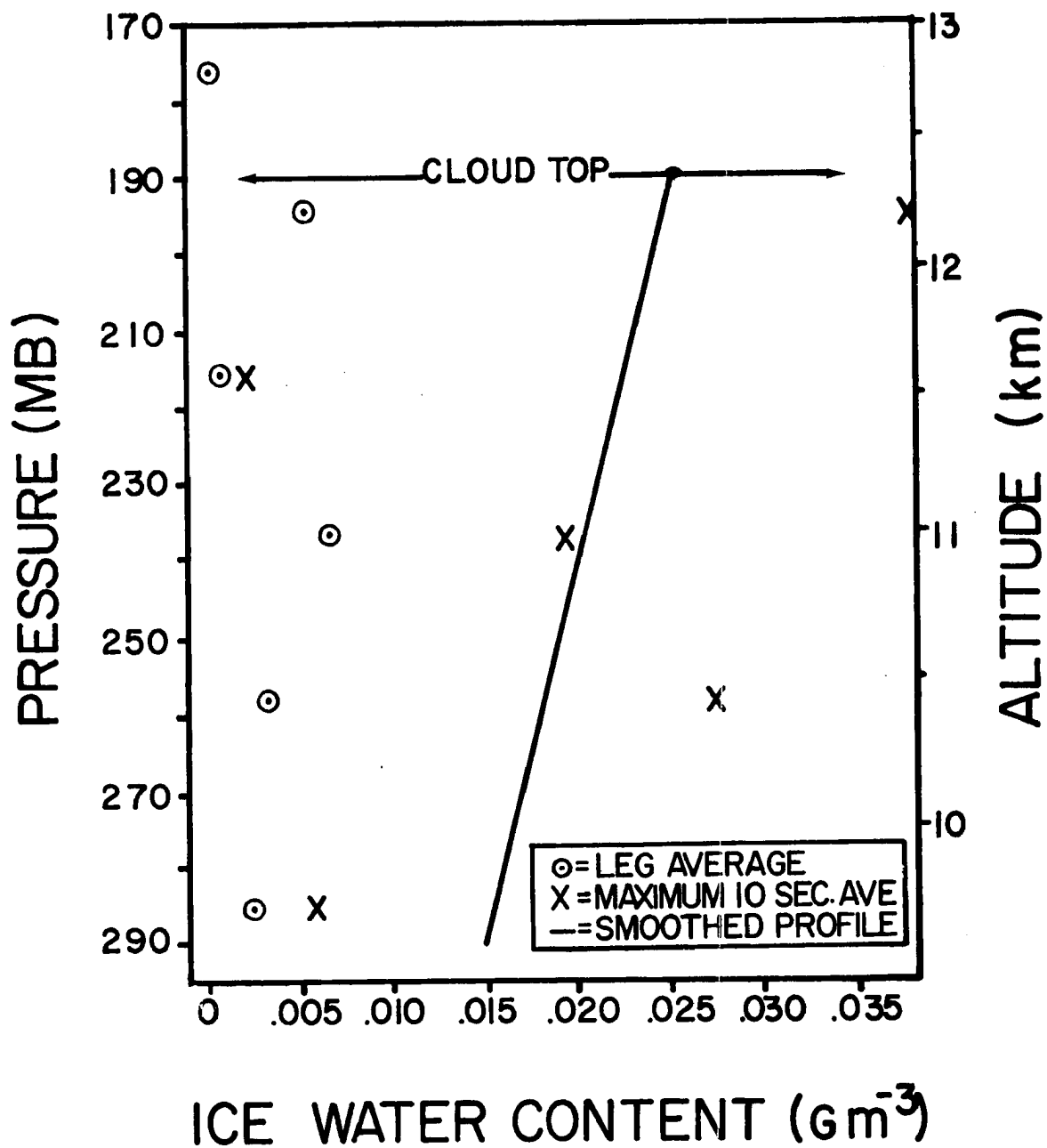


Figure 18. Vertical profile of ice water content for Day 232.

the patchy, disorganized nature of this cloud system. Detailed inspection of IWC on each data flight leg revealed that the aircraft was totally out of the cloud for a portion of every flight leg. Figure 18 presents both the average IWC for each flight leg and the maximum 10 second average value. The solid line is the hand drawn profile chosen to represent the column water content when integrated in the vertical.

Since this case does not fit the desired ideal horizontally homogeneous situation, a different method of analysis was used. The irradiance data at each level were stratified into 3 categories based on the range of values found at each level. The categories are composed of all values falling in the top 10% of the range, the bottom 10% of the range and thirdly all values not fitting into either of the first two categories.

The rationale in using this procedure is that in a broken cloud condition such as this there should be a nearly binary instrument response. For instance, the highest downward irradiance values should occur while in the cloud and the lowest values should occur while in clear air. There will be a region of intermediate values where the hemispheric field of view of the instrument will sense both clear and cloudy regions. Using the criteria of 10% of the range requires that only one tenth of the flight leg be typical of the cloudy area or of the clear area. The implicit assumption is also made that the cloudy areas are correlated in the vertical. That is, the maximum downward irradiance at 32,000 feet must be related to the same cloud situation that produced the maximum downward irradiance at 38,000 feet. One test of this hypothesis is whether or not the maximum IWC on each leg occurs at the same time as the maximum downward irradiance. In this case, four

of the five in cloud data flight legs satisfied this test. The one flight leg that did not had only slightly smaller IWC than the maximum at the time of highest downward irradiance.

The results of this stratification analysis are shown in Figure 19. The maximum and minimum downward irradiance, blackbody irradiance at ambient temperature and the minimum curve for upward irradiance are shown. The actual measured points are indicated. Only the minimum curve for upward irradiance is shown since it is used for cooling rate calculations only and is essentially parallel to the maximum upward irradiance curve. For reference, a curve of clear sky downward irradiance has been calculated and plotted. It indicates that the minimum downward irradiance curve is being influenced by the surrounding cloud field. That is, even though the minimum curve values are taken in clear air, it is not the same as a sounding in a totally cloud free region. The irradiance values that were input to the model are represented by the smoothed curves of Figure 19.

Analysis of the stratified curves of maximum downward irradiance combined with the minimum upward irradiance is given in Figure 20 and 21. Emissivity vs. distance below cloud top is shown in Figure 20, with the 90% confidence limits shown by the dashed line envelope. Comparisons to curves derived from the work of Hunt and Liou are shown. These comparison curves were derived in a manner analagous to that used for Day 226. Hence, the total column water content as a function of distance below cloud top is the same for the three curves of Figure 20. The results are very similar to Day 226. The cloud of Day 232 has a higher emissivity than Day 226 down to a distance of approximately 800 meters, at that point, the curves cross. That behavior conforms to

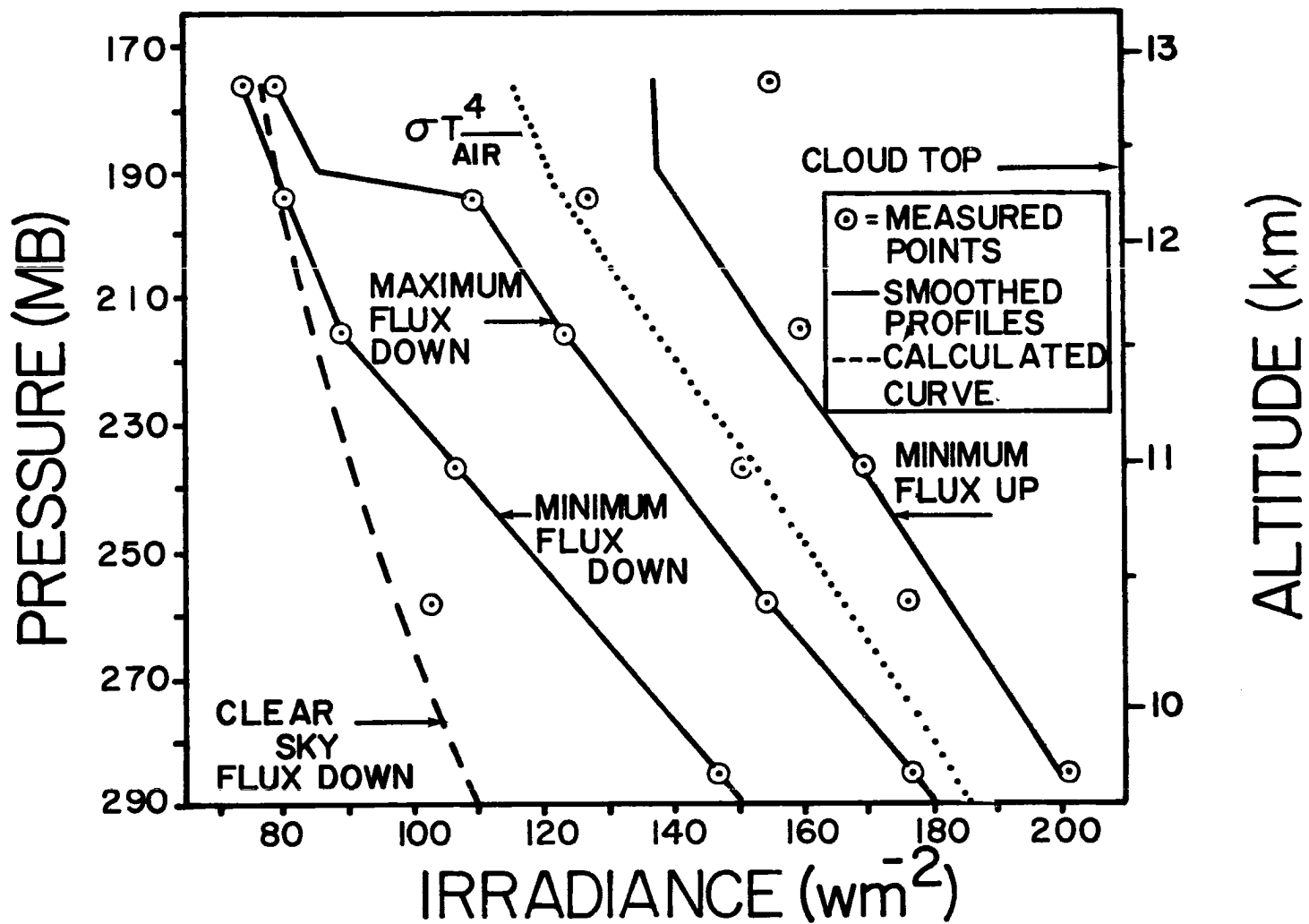


Figure 19. Day 232 irradiance profiles.

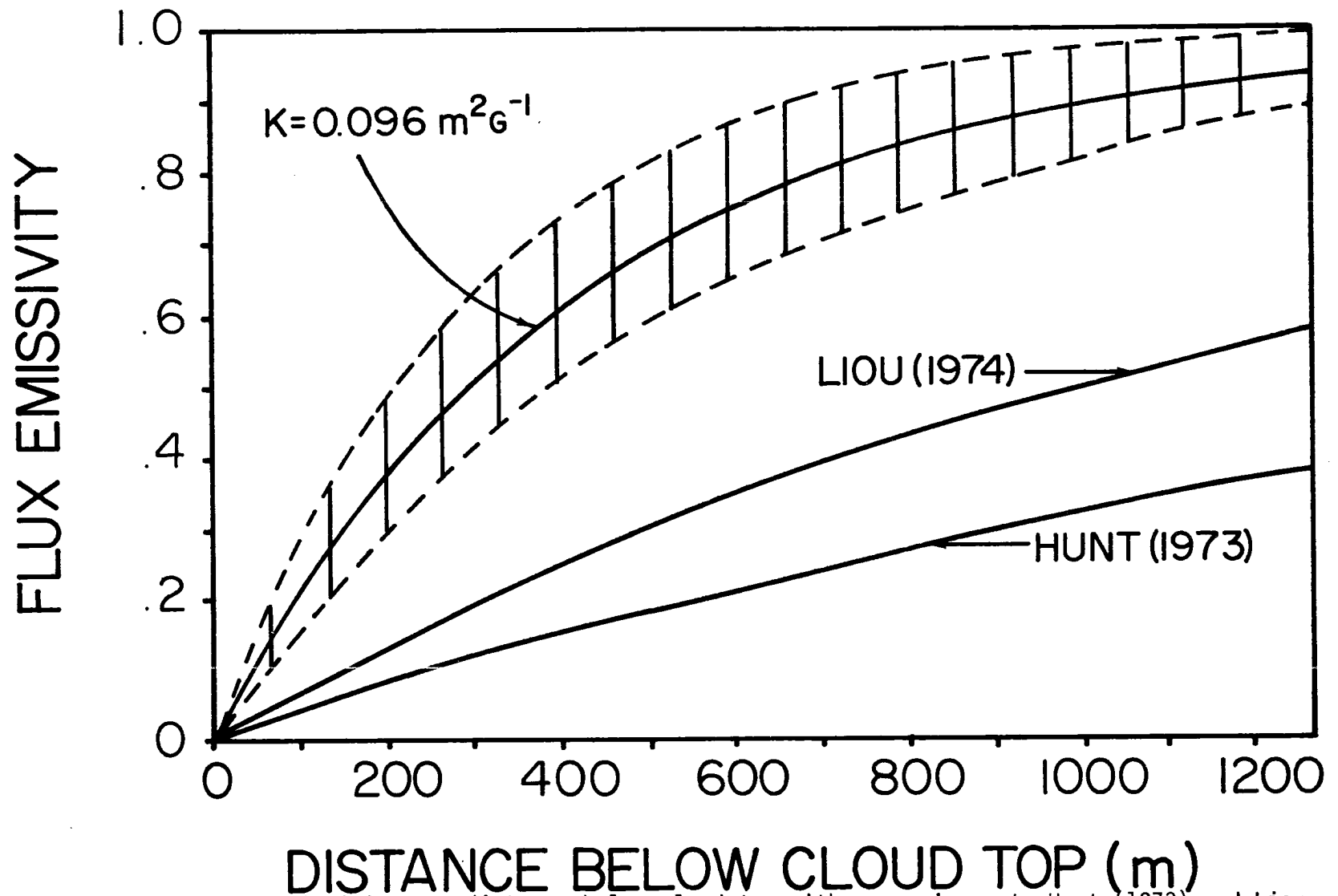


Figure 20. Day 232 emissivity vs. distance below cloud top with comparisons to Hunt (1973) and Liou (1974). (Dashed line envelope indicates uncertainty).

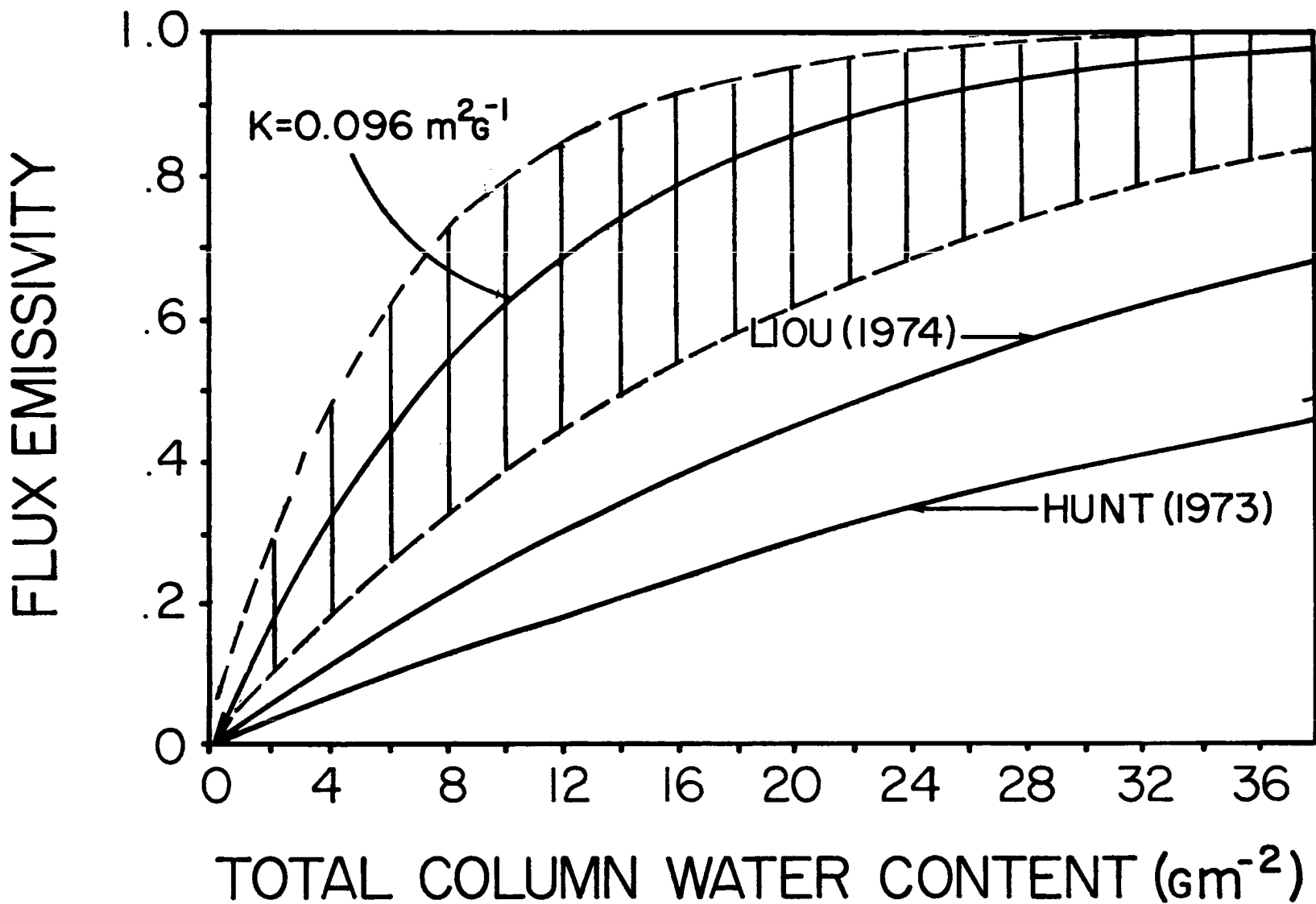


Figure 21. Day 232 emissivity vs. total column water content with comparisons to Hunt (1973) and Liou (1974). (Dashed line envelope indicates uncertainty).

that which would be expected based on a comparison of the water content structure of the two clouds. As on Day 226, the measured emissivities are much greater than those obtained from the work of Hunt or Liou for a cloud of identical ice water content. The higher extinction efficiency factor of natural cirrus is again evident.

Figure 21 depicts emissivity as a function of the total water content of the column above the point in question. This figure depends, of course, on assumptions made in deriving ice water content as described in the Appendix. Section 3.4 details the effects of making some alternative assumptions about the ice water content. Again, the dashed line envelope indicates the region within which 90% of the emissivity values would lie given the possibility of concurrent measurement errors of magnitudes as outlined in Table 6. The curve is described by a K value of  $0.096 \text{ m}^2\text{g}^{-1}$ . The K value is inversely proportional to the total column water content as discussed previously. There is uncertainty in the K parameter due to the placement of the IWC curve indicated in Figure 18. The curve used to obtain the K value of 0.096 was determined subjectively to be the most reasonable representation of the IWC in the maximum downward irradiance areas. The most extreme assumptions of IWC profile would have yielded a mass absorption coefficient of  $0.060 \text{ m}^2\text{g}^{-1}$  (for maximum IWC) to  $0.180 \text{ m}^2\text{g}^{-1}$  (for minimum IWC).

The results of Day 232 depicted in Figure 21 are again similar to Day 226. The K values agree within the bounds of the uncertainty in their determination. The comparison to the curves of Hunt and Liou reveals the same situation as discussed for Day 226, the measured emissivities are substantially higher than the theoretical values.

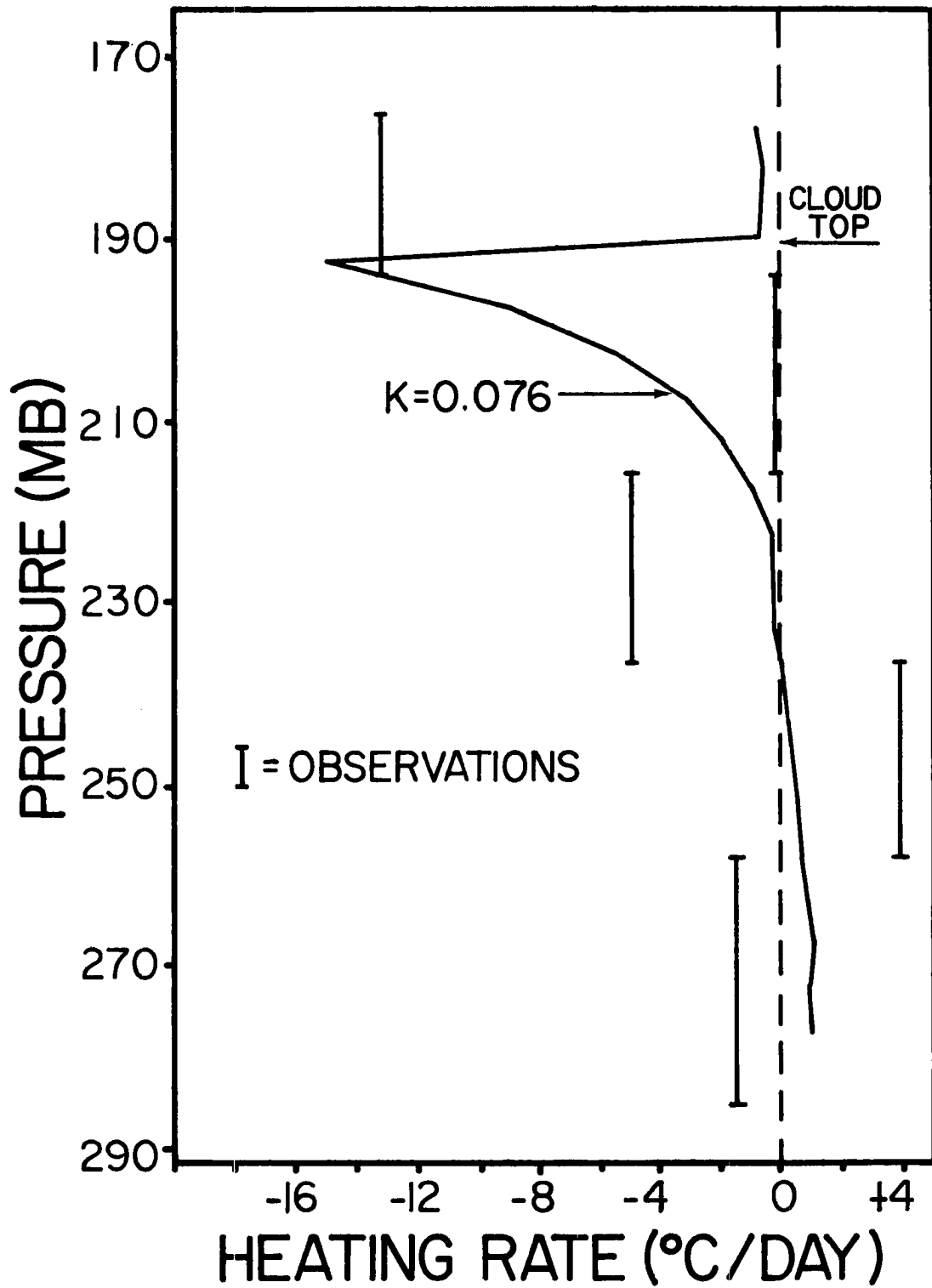


Figure 22. Heating rate as a function of pressure, Day 232.

Heating rate as a function of pressure is displayed in Figure 22. The continuous curve is obtained from the model smoothed upward and downward irradiances. As on Day 226, the K value derived from the downward irradiance has been used to produce the smoothed upward irradiances, demonstrating that the K value yields reasonable results in a situation other than that in which it was obtained. The vertical bars represent layer heating rates obtained from the actual measured downward irradiances coupled with the smoothed profile of upward irradiance depicted in Figure 19. This method was adopted due to the obvious effects of inhomogeneities in the cloud field on the upward irradiance. It is felt that this is justified because in this situation heating rates are primarily driven by the downward irradiance.

### 3.33 Day 251 - September 8, 1974

This set of data flight legs was flown in and through an active cumulonimbus cell with a classic cirrus anvil in the outflow region. There were 9 sampling flight legs at 8 levels ranging from 43,000 feet to 20,000 feet and averaging 8 minutes in length. The flight leg at 43,000 feet (164 mb) was clearly above cloud top but no flight leg below cloud base was obtained. Hence, the upward irradiance can be used only for cooling rate calculations, as in the first two cases.

Figure 23 depicts the profile of ice water content with the measured points indicated. The smoothed profile was drawn to indicate a slightly higher IWC at the 40,000 foot level than was actually measured. This was necessary because examination of the flight film indicated that there was a somewhat layered structure to the cloud. The integrated smoothed profile is intended to provide a more accurate representation

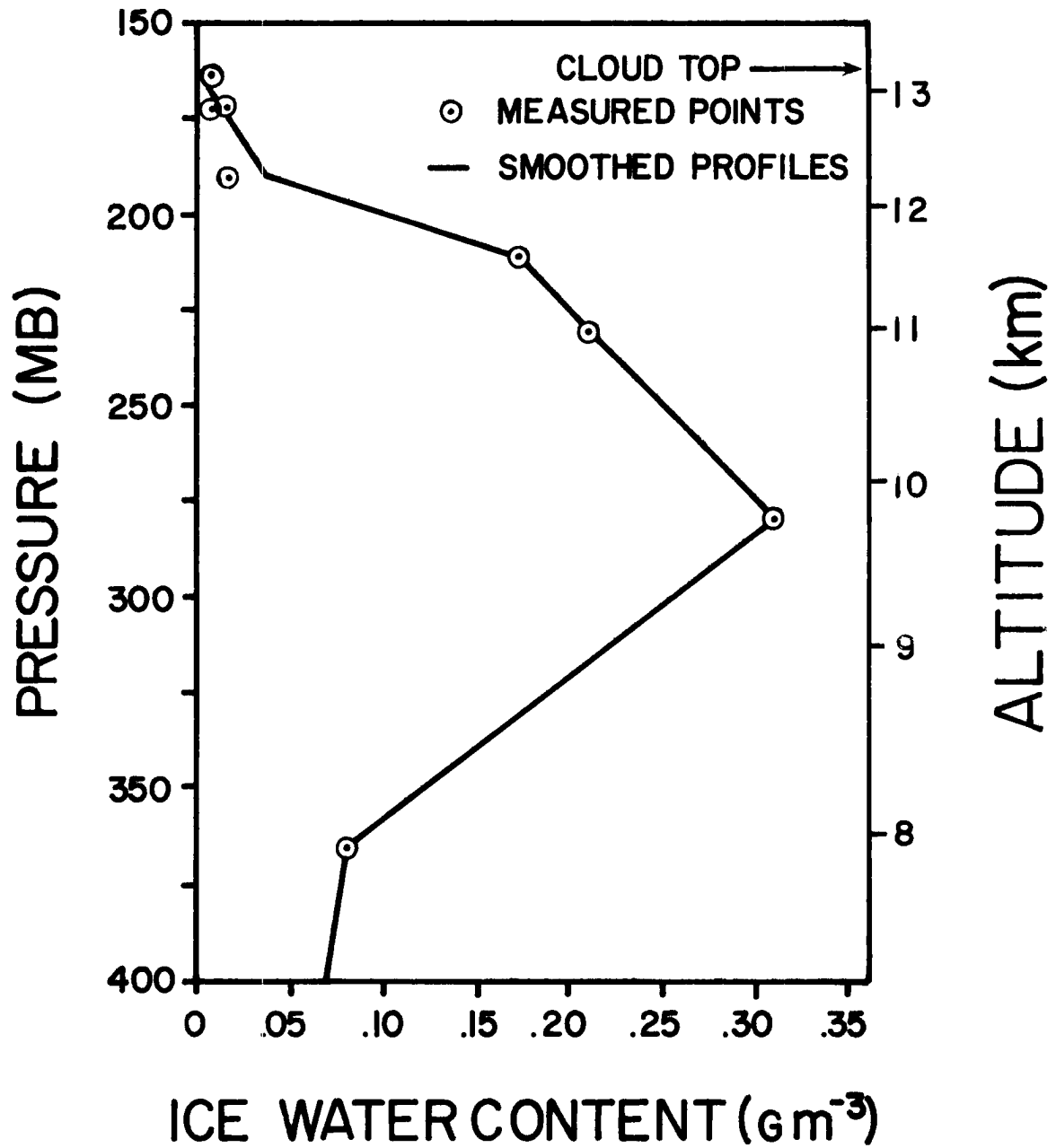


Figure 23. Day 251 vertical profile of IWC.

of the total column water content than would be obtained from strict interpretation of the 40,000 foot IWC measurement. There is a rather sharp transition between the flight leg at 40,000 feet and the flight leg at 38,000 feet. The four data points at 40,000 feet and above are similar in magnitude to the values found on Days 226 and 232. The points below that peak out at over  $0.3 \text{ gm}^{-3}$ , which is nearly an order of magnitude larger than any previous IWC measurement. This clearly indicates that the lower portions of this cloud system contained an active cell. As in the previous two cases, some assumptions have been made in deriving IWC. The Appendix should be consulted for details.

This case was treated with the stratification technique outlined in the Day 232 case. The results are shown in Figure 24 with the maximum and minimum downward irradiance, maximum and minimum upward irradiance and the blackbody curve computed from ambient temperature. It is seen that the maximum downward irradiance exceeds the blackbody curve at several points. The discrepancy is not large, however, corresponding to approximately  $3^{\circ}\text{C}$ . This occurs only in the 3 legs that penetrated the most active part of the cell as indicated by the highest IWC. It is likely that there was some difficulty in making the correction for dynamic heating of the temperature sensor under those flight conditions.

There are other interesting features of these profiles that may be understood by examination of the flight film and the Knollenberg Probe data. For instance, there is a small deviation in the minimum downward irradiance curve at 38,000 feet. Detailed analysis of the IWC revealed that it was the only flight leg which was totally in cloud for its entire length. All other flight legs experienced some cloud free region and thus, all fit into a coherent profile. In a second example, the

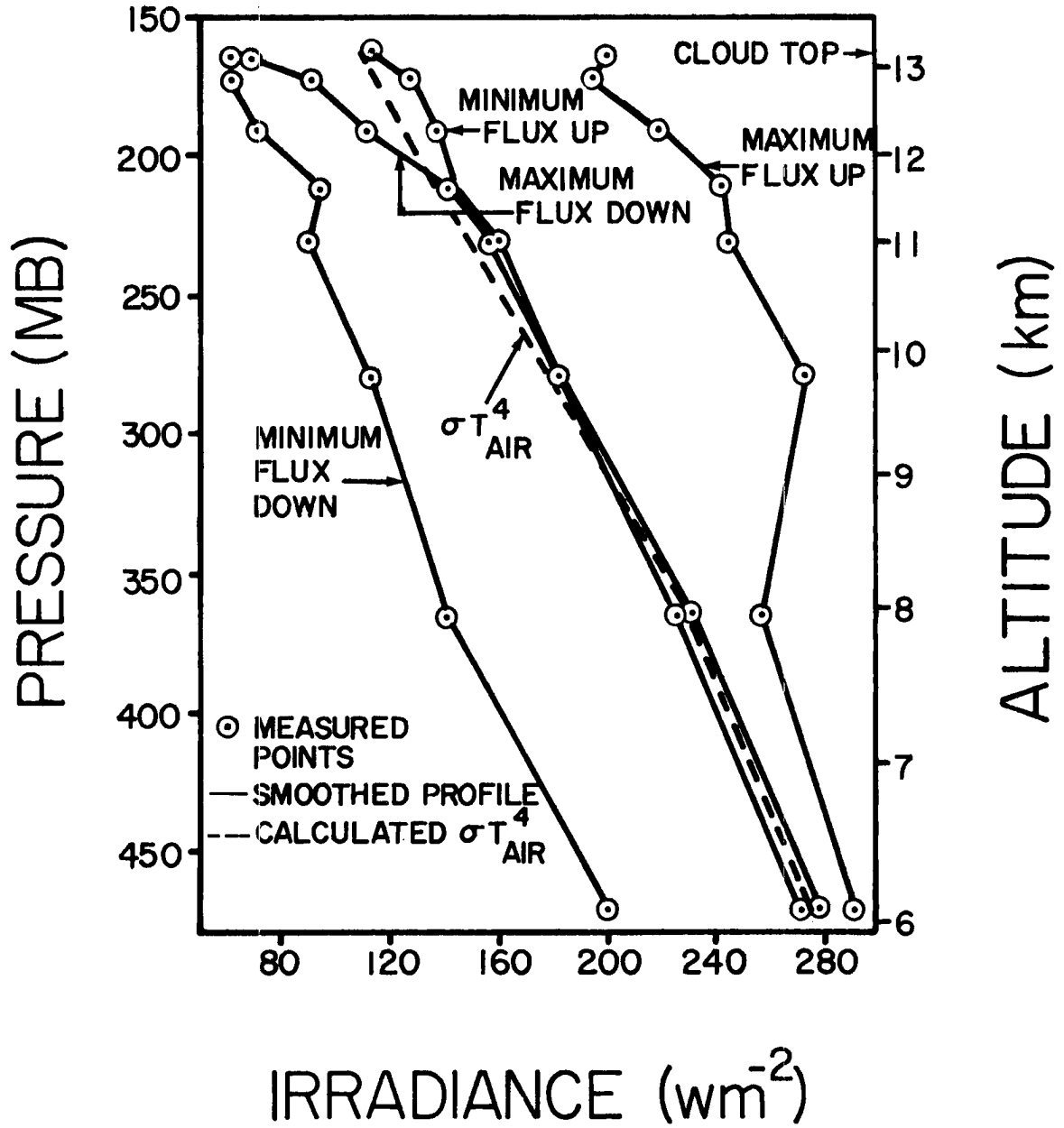


Figure 24. Day 251 irradiance profiles

maximum upward irradiance profile has values at 26,000 and 20,000 feet that do not seem to fit with the values at higher levels. The flight film indicates that these two lowest flight legs were made over a middle cloud deck when not in the cell itself. Hence, the higher flight legs which had a view of the ocean, are relatively "warmer" than the low flight legs that saw only cold middle clouds.

The model was used to analyze the maximum cloud condition curves, i.e. the minimum upward irradiance combined with the maximum downward irradiance. The curves of emissivity vs. distance below cloud top are shown in Figure 25. As mentioned for the other cases, the dashed line envelope outlines the 90% confidence limits when consideration is given to the possibility of concurrent measurement errors. Comparisons to Hunt and Liou are again indicated and were obtained in a manner analogous to that described for Day 226. The three curves therefore use the same function of total column water content vs. distance below cloud top. The results are similar to both Days 226 and 232, because their IWC profiles are similar down to approximately 1000 meters into the cloud. Below that the cloud is already about 90% black and the IWC differences have little effect.

Emissivity vs. total water content of the column is displayed in Figure 26 with the 90% confidence limits shown. A K value of 0.080 is used to describe Day 251. The dependence on IWC is very strong as discussed previously but the most extreme assumptions of IWC would yield K values from 0.070 to  $0.106 \text{ m}^2 \text{ g}^{-1}$ . The assumptions made in deriving IWC are detailed in the Appendix and some effects of alternative IWC assumptions are discussed in Section 3.4. This K value agrees with the values obtained on Day 226 and 232 within the uncertainty of their

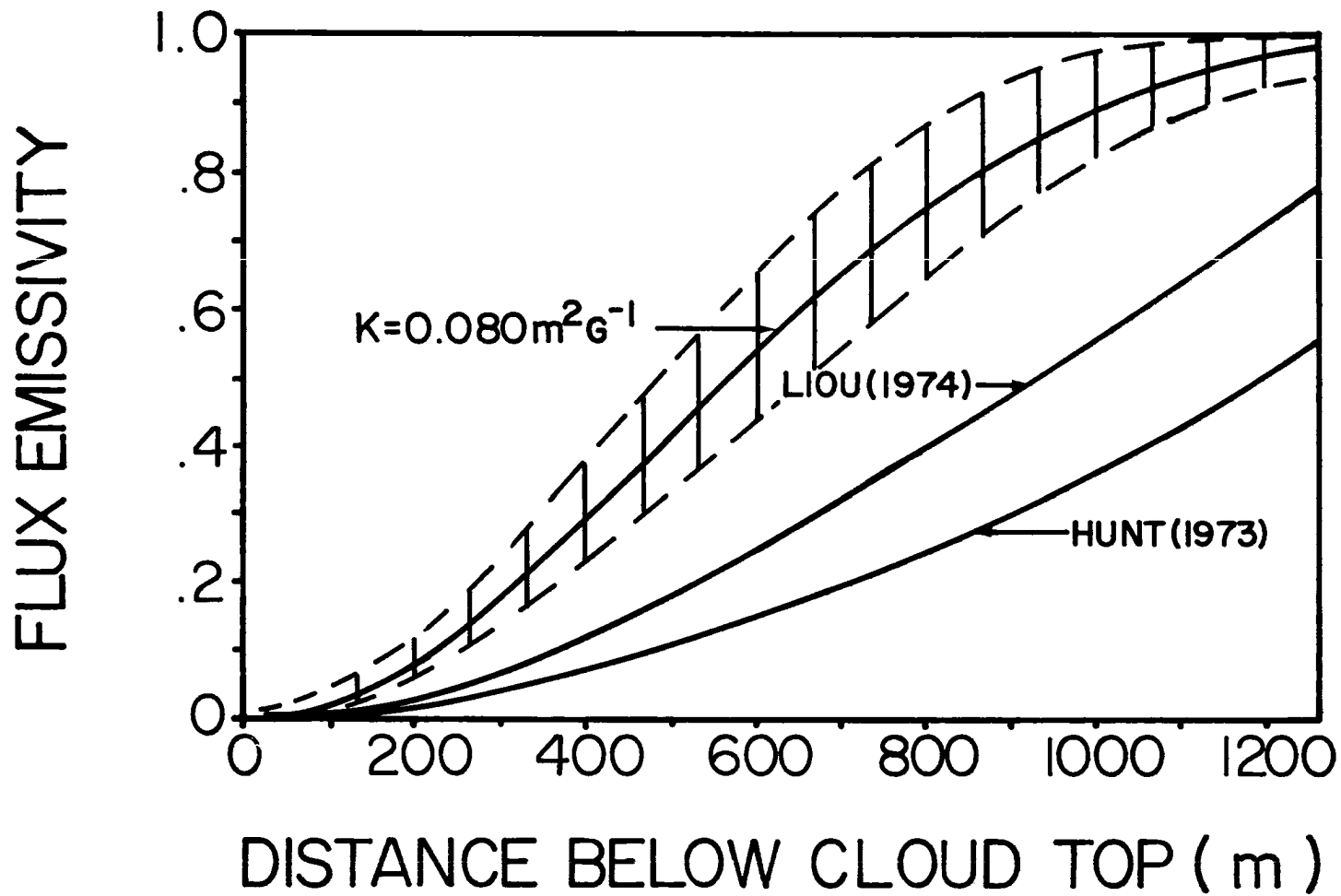


Figure 25. Day 251 emissivity vs. distance below cloud top with comparisons to Hunt (1973) and Liou (1974). Dashed line envelope indicates uncertainty).

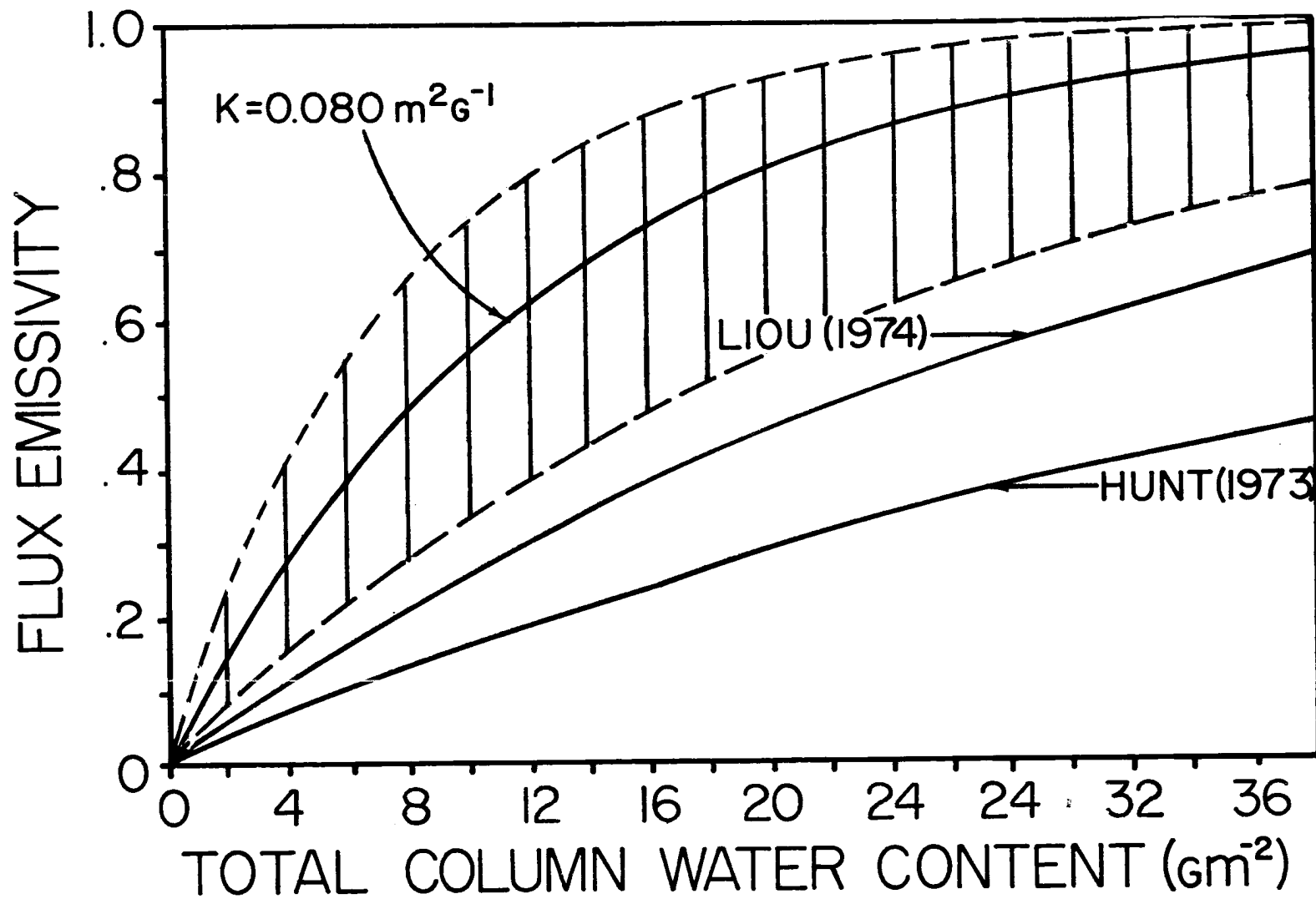


Figure 26. Day 251 emissivity vs. total column water content with comparisons to Hunt (1973) and Liou (1974). (Dashed line envelope indicates uncertainty).

determination. Hunt and Liou curves reveal the same relationship to the measurements as previously indicated: theoretical values are lower.

Heating rates are depicted in Figure 27 as a function of pressure. The curve is derived from the irradiances smoothed by the K value of  $0.080 \text{ m}^2\text{g}^{-1}$ . It is typical of a cloud layer and appears quite similar to the other days studied. The vertical bars represent layer heating rates obtained from the actual measurements of upward and downward irradiance. The expected general characteristics of a cloud layer are evident. The dip in heating rate for the layer from 172 mb to 190 mb is undoubtedly a result of the somewhat layered structure of the cloud as discussed earlier.

### 3.34 Summary of Case Studies

There are substantial similarities in the tropical cirrus cloud properties found on three different days. Broadband mass absorption coefficients fell in the rather narrow range of  $0.076 \text{ m}^2\text{g}^{-1}$  to  $0.096 \text{ m}^2\text{g}^{-1}$ . Heating rates as a function of pressure were quite uniform both in general shape and in the magnitude of the cloud top cooling maximum. Figure 28 superimposes on a single graph the smoothed heating rates for the three days. The curves have been normalized to a common cloud top location. Figure 29 compares emissivity as a function of distance below cloud top for the three cases. The strong similarities are again apparent.

As pointed out in Figures 10 and 11, the particle size distributions as measured by the Knollenberg Probe did not vary substantially from day to day or at different levels on the same day. Hence, the differences in cooling rate profile and emissivity vs. distance cannot

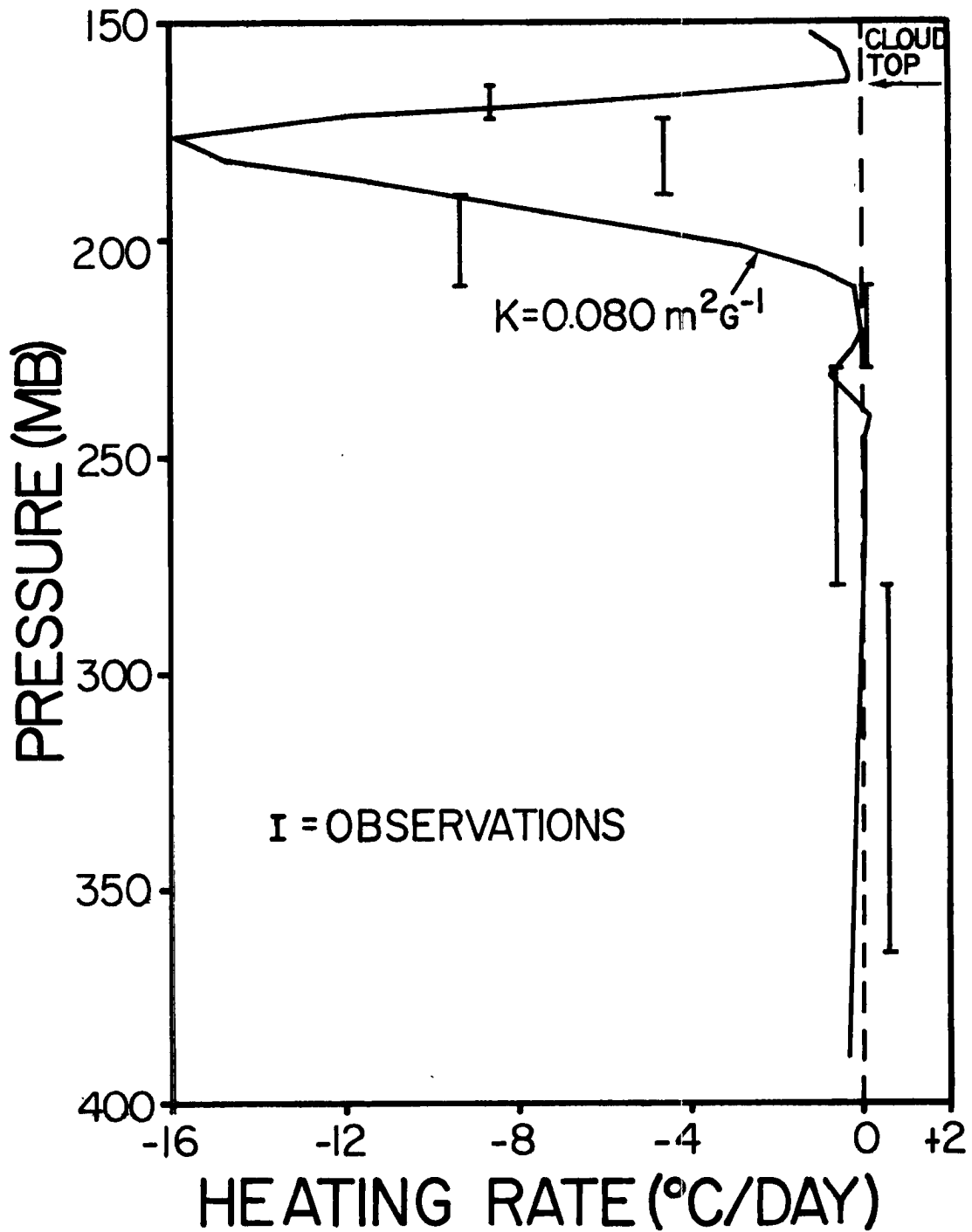


Figure 27. Heating rate as a function of pressure for Day 251.

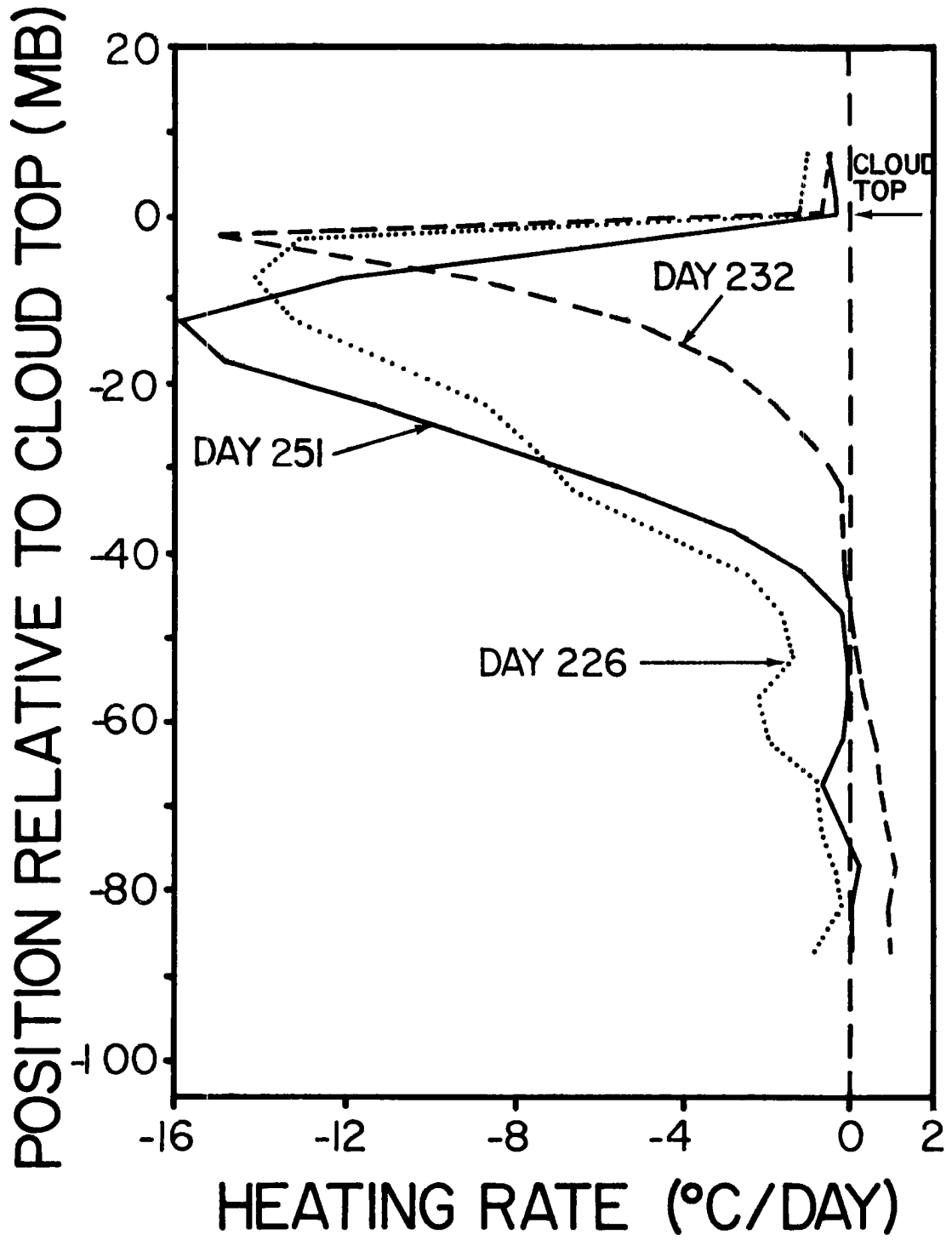


Figure 28. Heating rate as a function of pressure for the three cases. (Normalized cloud top location).

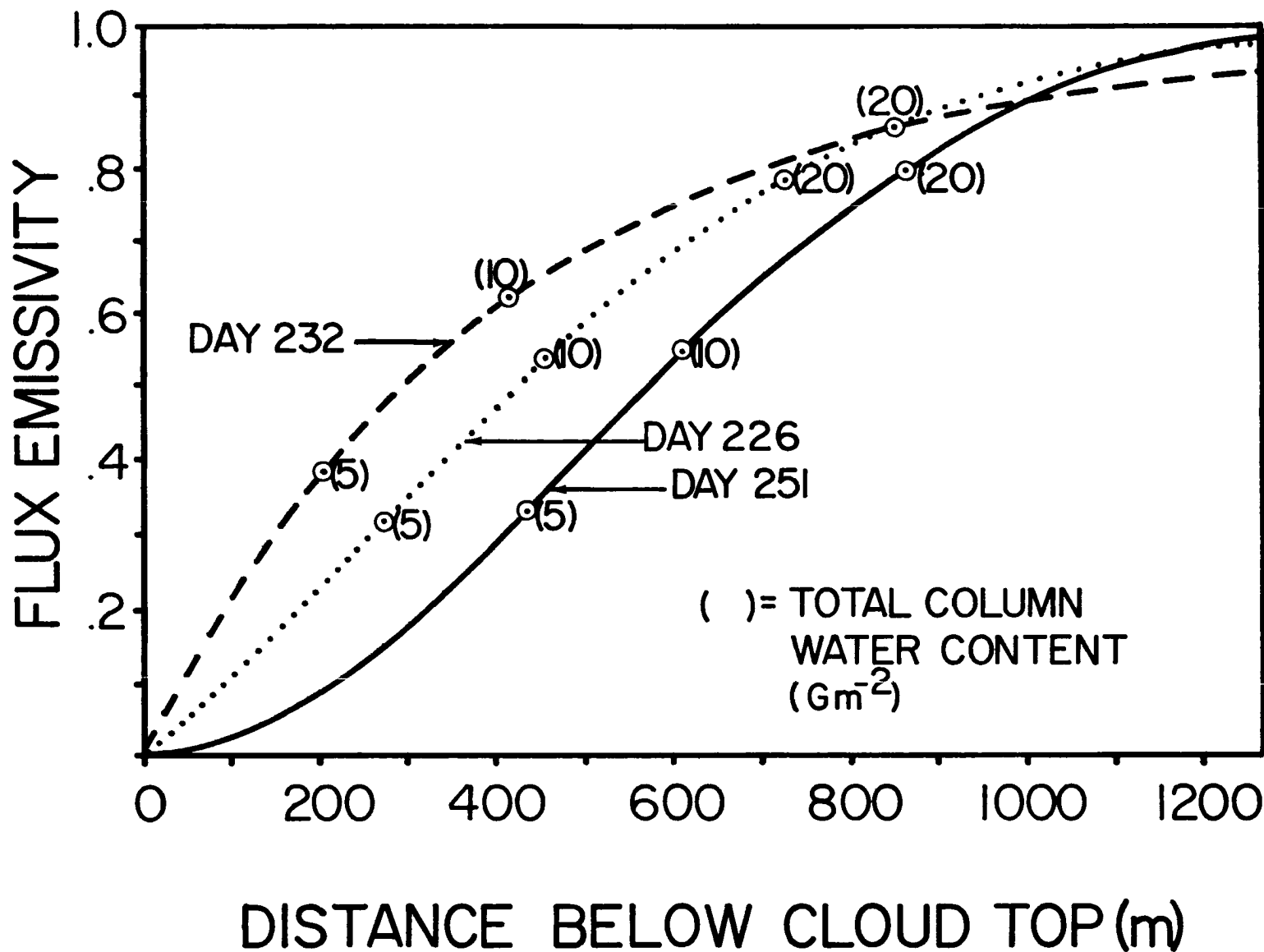


Figure 29. Flux emissivity vs. distance below cloud top for the three cases studied, with total column water content at selected points.

be attributed to size distribution but rather must be a result of number density variations.

The minor differences that are in evidence in Figures 28 and 29 may be readily understood in terms of the IWC profiles of the individual cases. For instance, the cooling maximum occurs deepest into the cloud on Day 251 due to the lower IWC near cloud top on that day. Figure 29 shows that the emissivity as a function of distance below cloud top for the first kilometer is lowest for Day 251. The cooling spike is closest to cloud top on Day 232. Figure 29 shows that of the three cases, Day 232 has the highest emissivity in the first kilometer. Another way of understanding the differences in heating rates is to examine the total column water content as a function of distance below cloud top. This information is indicated in Figure 29. Day 232 accumulates  $5 \text{ gm}^{-2}$  in approximately 200 meters below cloud top. Day 251 requires about 430 meters to accumulate the same  $5 \text{ gm}^{-2}$ . Hence, the top portion of the cloud on Day 232 is more dense than on Day 251.

We may safely assume that the heating rate near cloud top will be driven primarily by the downward irradiance. The greatest cooling will then coincide with the greatest rate of change of downward irradiance. This occurs nearer to cloud top on Day 232 than on Day 251 due to the greater IWC density near cloud top on Day 232.

The variability of downward irradiance on any given data flight leg is a measure of the variability of the cloud emissivity. Examination of a frequency distribution of effective emissivities computed according to Equation 6 reveals important information about the uniformity of these cirrus clouds. Figure 30 is a histogram of downward effective emissivity describing the leg at 36,000 feet on Day 232, 1.3

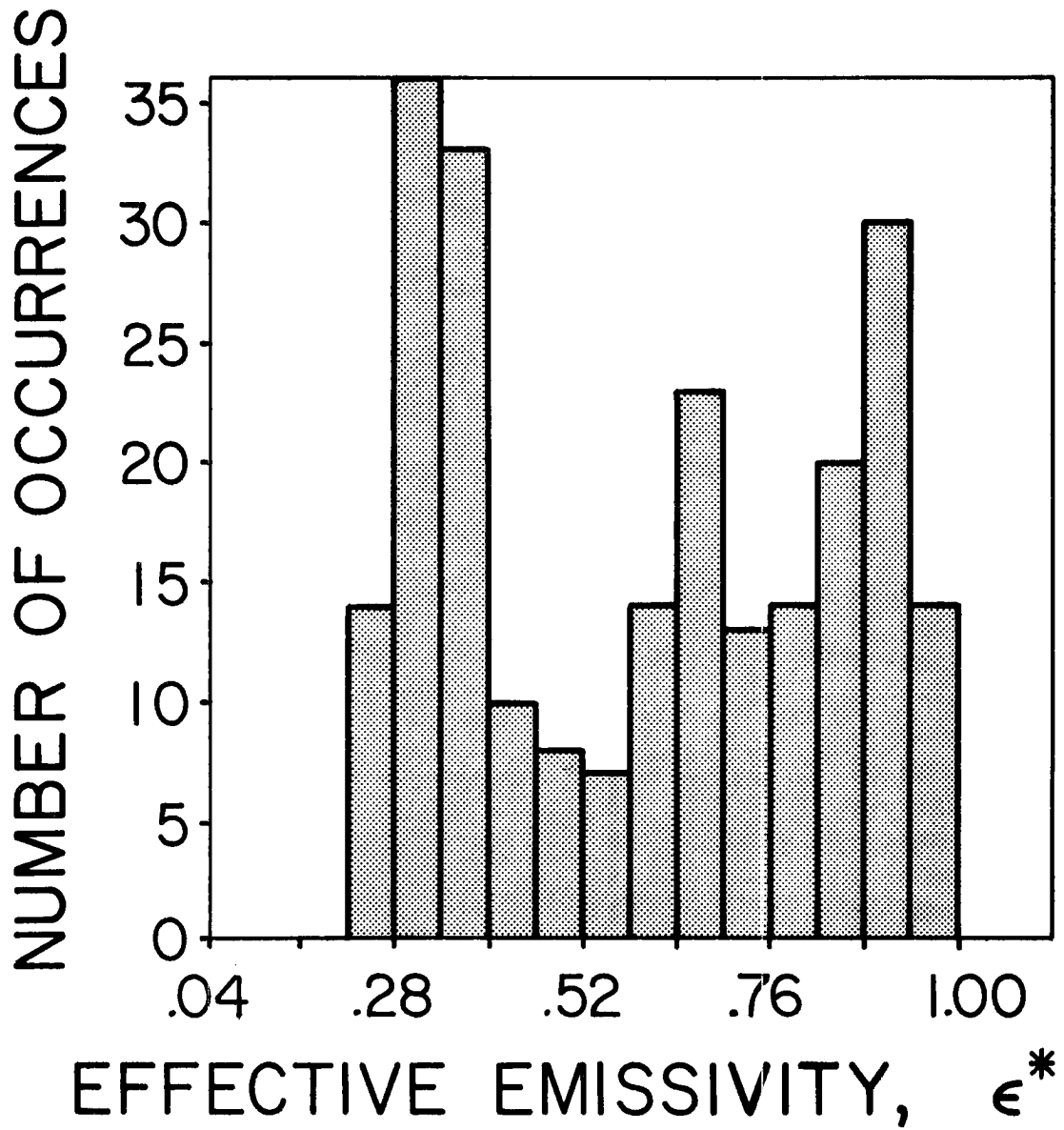


Figure 30. Effective emissivity,  $\epsilon^*$ , vs. frequency of occurrence for flight leg at 36,000 feet on Day 232. (1.3 km below cloud top)

kilometers below cloud top. It shows a wide range of effective emissivities quite uniformly distributed. This is the same flight leg described in Figure 9 in which the time series of downward irradiance and ice water content were given.

### 3.4 Possible Explanations of the Discrepancy Between Theory and Observation

Several of the figures describing the results of the individual case studies have pointed out the large differences between the present results and the calculations of Liou (1974) and Hunt (1973). There are at least two plausible explanations, one concerning the measurement of ice water content and the other concerning the orientation and type of ice crystals assumed in the theoretical studies.

The Appendix describes the process used and the assumptions made in obtaining the ice water content profiles of Figures 12, 18 and 23. If, however, we make different assumptions regarding the extrapolated portion of the particle spectra, significantly different total IWC values can be obtained. Heymsfield (1975, 1976) and Heymsfield and Knollenberg (1972) show particle spectra that indicate an exponential relation in the number of very small particles present. Figure 31 shows the exponential extrapolation of particles per cubic meter for the same measured distribution illustrated in Figure A4 of the Appendix. Figure 32 shows the function of IWC vs. particle size for the size distribution of Figure 31. A distinct secondary maximum results and causes an increase of about 40% in the total ice water content as compared to the identical data set with a difference extrapolation as illustrated in Figure A5. Similar percentage increases in total ice

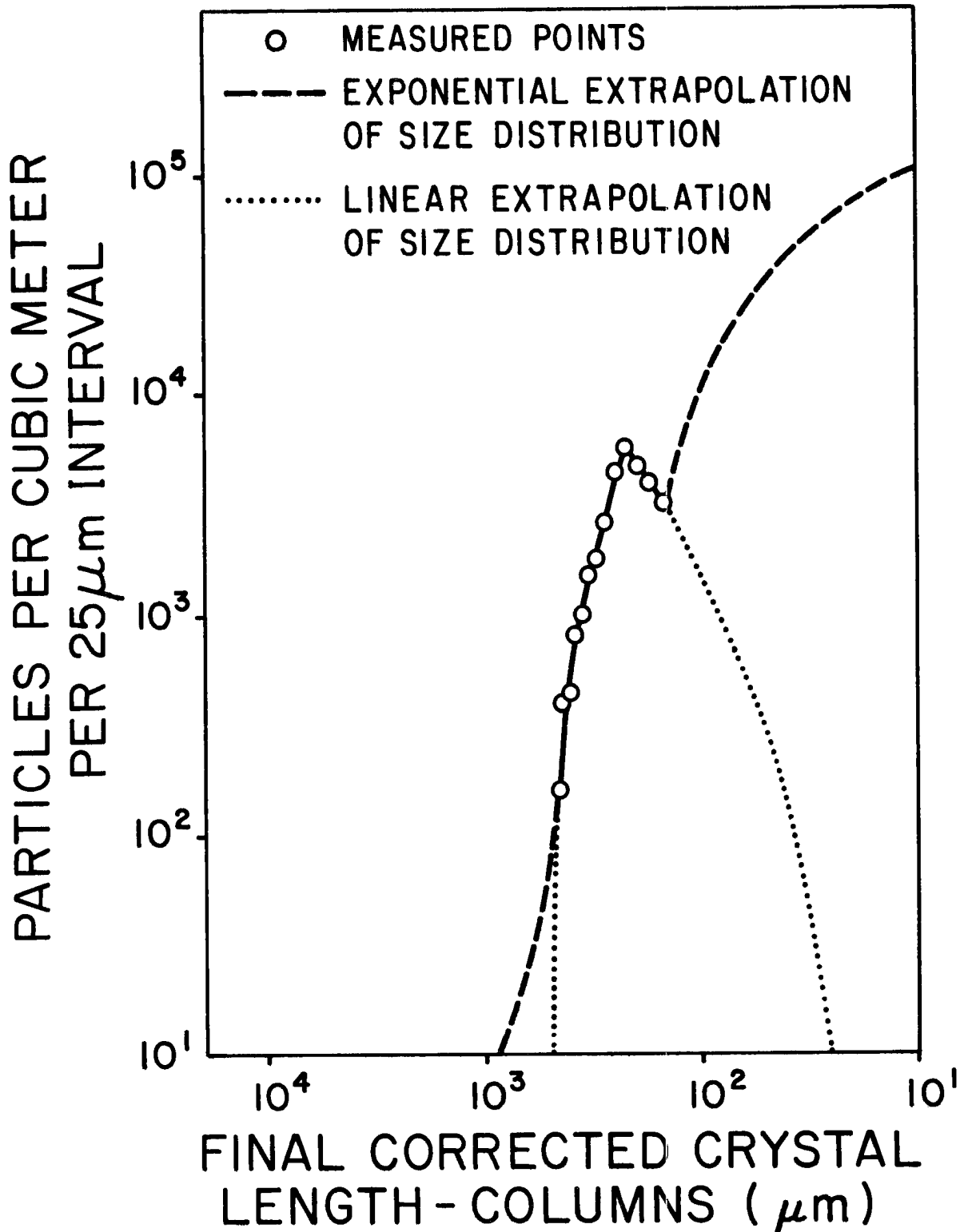


Figure 31. Particle size distribution for Day 226, 34,000 feet. Crystals are here assumed to be 100% columns. Measured points and two possible extrapolations are illustrated.

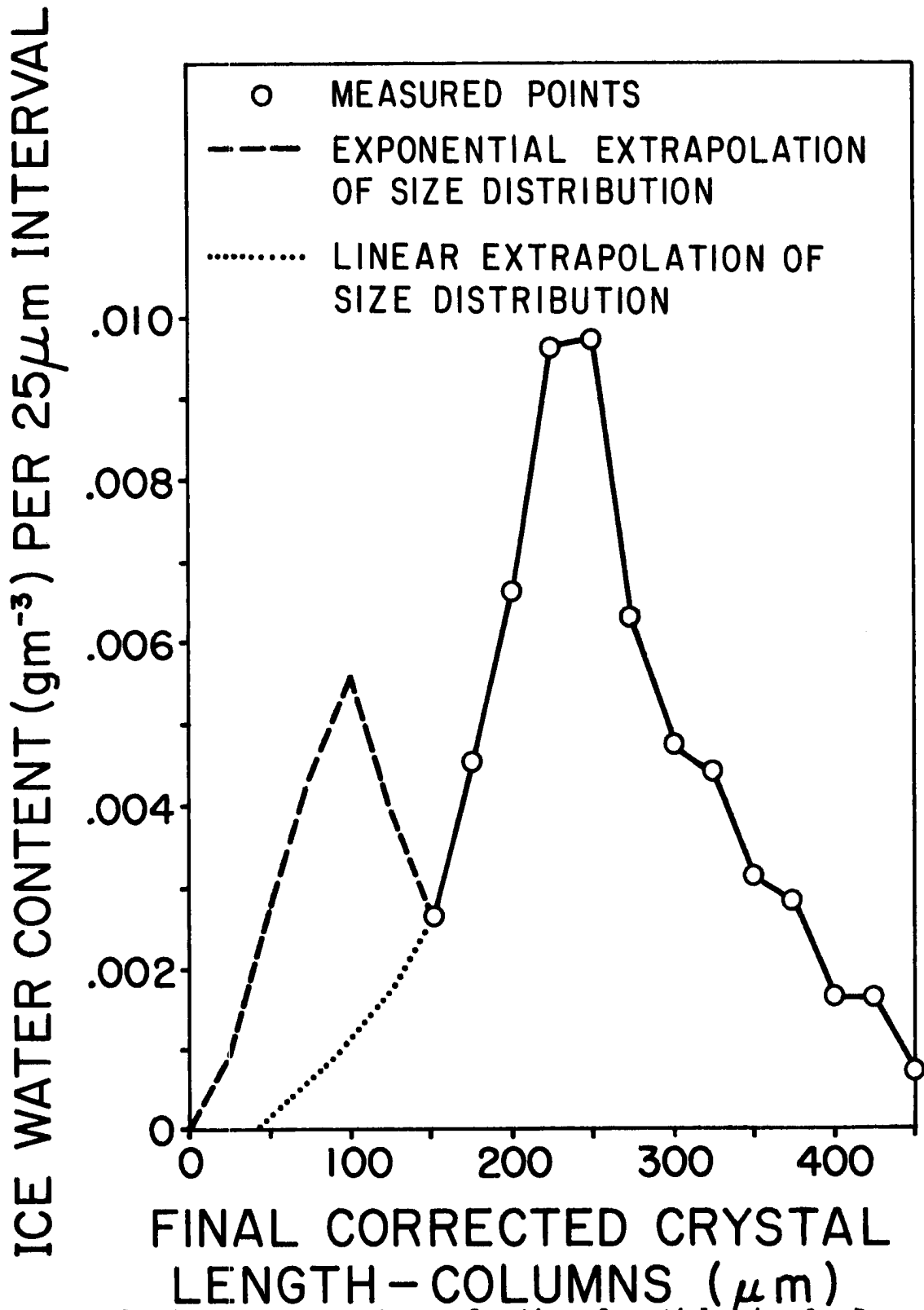


Figure 32. Ice water content as a function of particle size for Day 226, 34,000 feet. Crystals are here assumed to be 100% columns. Measured points and two possible extrapolations are illustrated.

water content were found for other data flight legs on the three days studied.

The effect of this change in IWC on the retrieval of mass absorption coefficients and emissivities is discussed in general terms in Section 2.43 and Table 3. Specifically the K values derived based on the IWC profiles given in Figures 12, 18 and 23 would be too high. The relationship of inverse proportionality between IWC and K would dictate that for a uniform 40% increase in IWC, the previous K value would have to be divided by 1.40. This adjustment would bring better agreement between observation and theory. Figure 33 illustrates this for Day 226. Emissivity vs. total column water content is shown in the same format as Figure 15, complete with comparisons to Liou (1974) and Hunt (1973). The observational curve is now significantly closer to the theoretical. Figure 34 depicts emissivity vs. distance into the cloud for the adjusted IWC profile for Day 226. Comparison with Figure 14 reveals that the discrepancy between the curves is greatly reduced. It is important to note that the observational curve of emissivity vs. distance into the cloud has not changed as a result of the increased ice water content. This characteristic of the emissivity vs. distance function is discussed in Section 2.43 and Table 3. The better agreement in evidence is a result of the two theoretical curves being adjusted upward as a result of the added IWC. A different mechanism is producing the improvement apparent in Figure 33. Here the two theoretical curves have not changed; the observed curve has been lowered due to the lower K value resulting from the higher IWC.

The possible existence of numerous small particles may lead to the conclusion that the extinction efficiency of the entire distribution

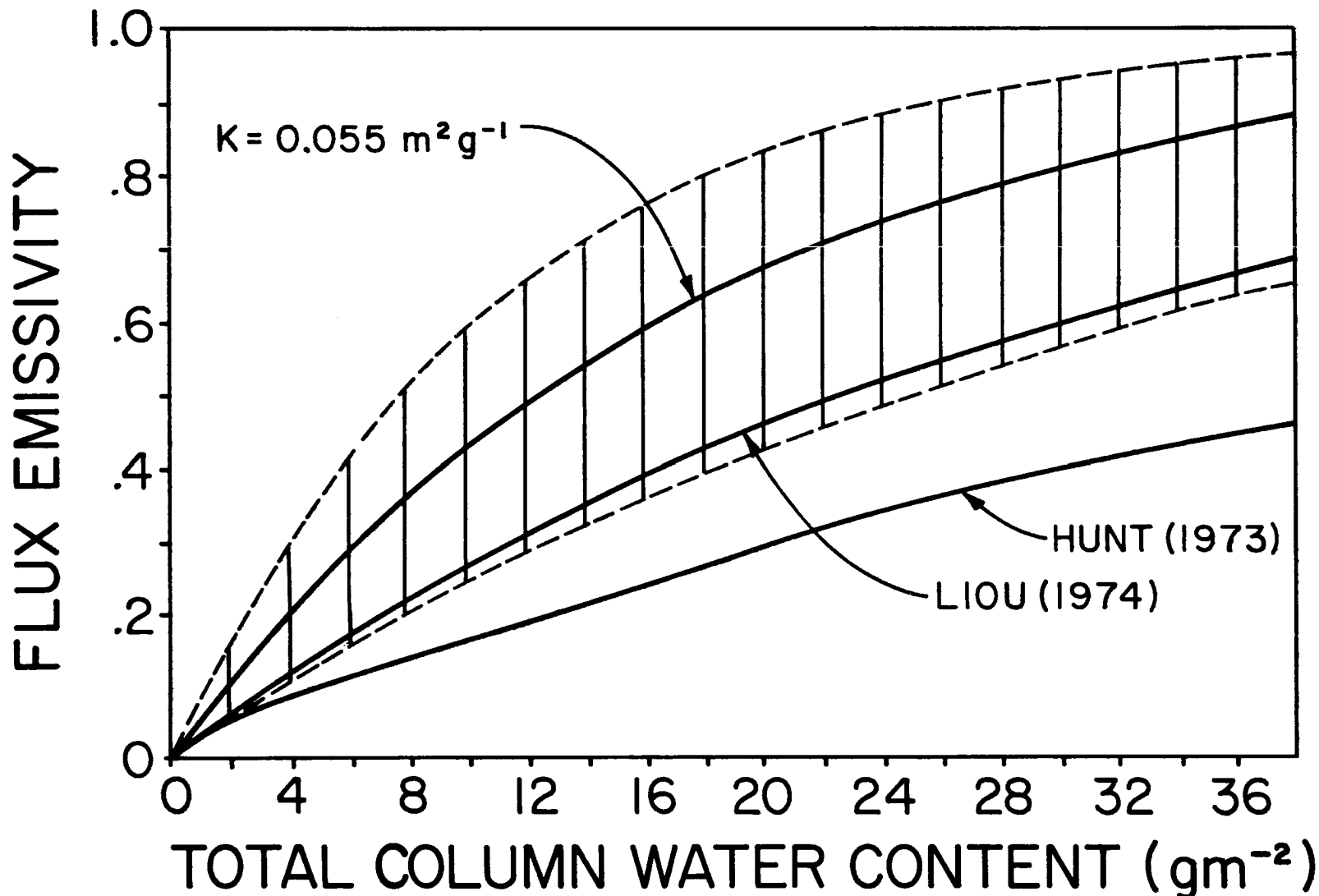


Figure 33. Day 226 emissivity vs. total column water content with comparisons to Hunt (1973) and Liou (1974). Observed curve derived using modified ice water content obtained from extrapolations of Figures 31, 32. (Dashed line envelope indicates uncertainty in observations).

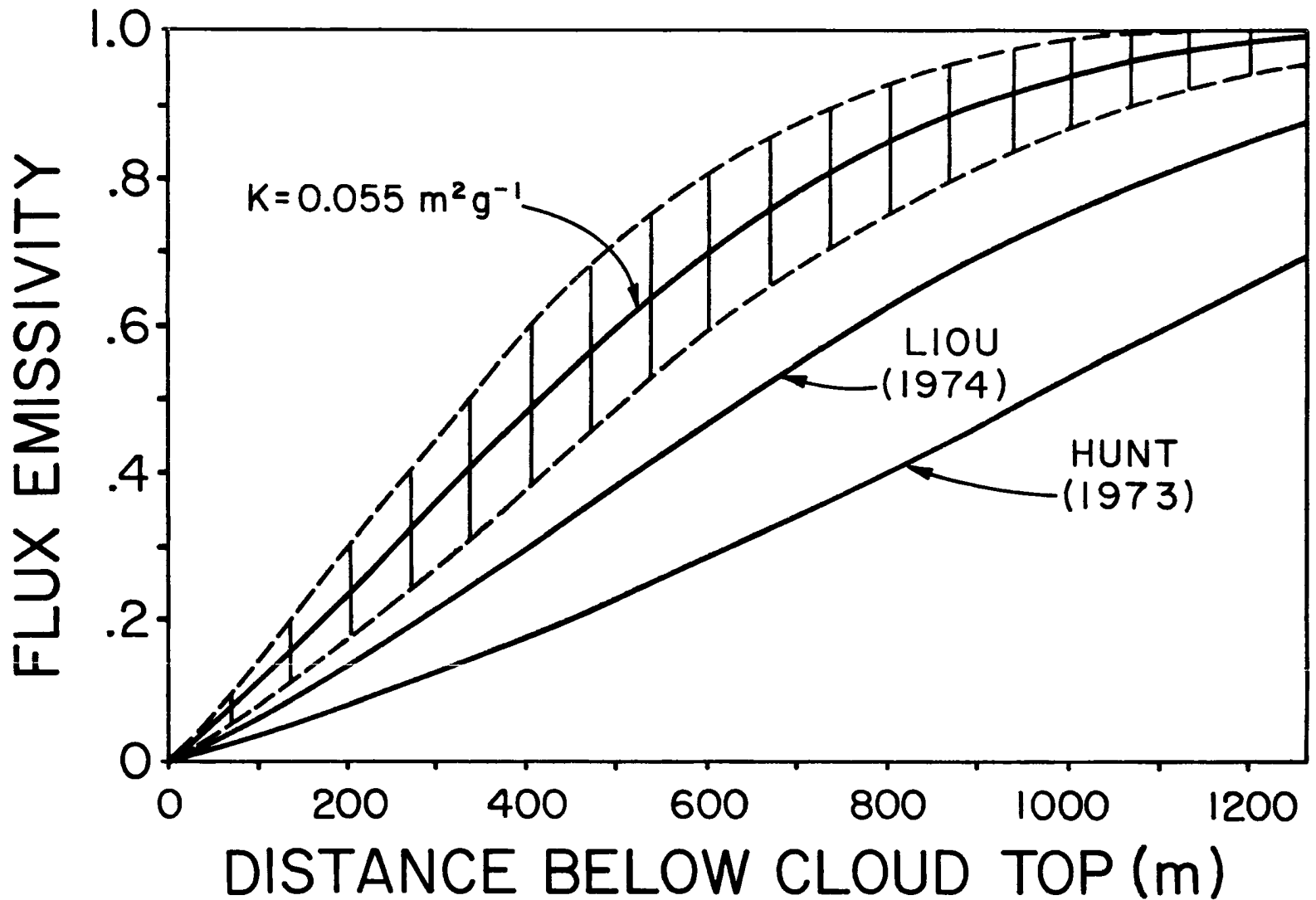


Figure 34. Day 226 emissivity vs. distance below cloud top with comparisons to theoretical studies of Hunt (1973) and Liou (1974). These curves use modified ice water content obtained from Figures 31 and 32. (Dashed line envelope indicates uncertainty in observations).

has been significantly altered. Paltridge and Platt (1976) discuss the effect of the size parameter ( $2\pi R/\lambda$ ) on the extinction efficiency of particles. A weighted average performed for the two extrapolated size distributions reveals that the extinction efficiency, at least for equivalent spheres, changes very little, remaining close to 2.

The second reasonable explanation for the differences between observation and theory concerns the question of crystal type and orientation. It is an accepted fact that cirrus particles are not spherical. The differences between the theoretical work of Hunt (1973), who assumed ice spheres and Liou (1974) who used randomly oriented ice cylinders, are due in large part to this shape difference. This is discussed further in Section 3.1. The discussion here will deal with the effect of Liou's assumption of random orientation of the ice cylinders.

Fluid dynamical considerations dictate that cylindrical crystals present the most resistance to motion while falling. This dictates that the crystals fall with the long axis horizontal. Platt (1977) reported that observations of lidar backscatter from high cirrus layers indicated a coherent crystal orientation pattern in some instances. The presence of distinct optical phenomena such as halos confirm that there is some uniformity of crystal orientation at least occasionally. This means that the cross sectional area in a horizontal plane of a large number of cylindrical crystals would be much greater for the preferential orientation case than for the random orientation assumed by Liou. If we assume that the emissivity change would be proportional to the cross sectional area, then the magnitude of this effect is on the order of a factor of 1.5 to 2.0. This would allow the Liou curve

to move upward to within the envelope of uncertainty of the observations.

Two possible explanations for the discrepancies between theory and observation have been advanced. One suggests that the comparison between calculations and observations may be improved by employing different assumptions about crystal orientation. The other acknowledges the possibility that large numbers of small crystals may have been present but were not measured due to the limited size range of the particle spectrometer. It should be noted that all of the case studies were analyzed using the IWC data reduction procedure as outlined in the Appendix. This means that the possible effects of numerous small particles were not considered, even in computing the envelope of 90% confidence limits. As mentioned before, this would not change the observed curve of emissivity vs. distance below cloud top but would change the emissivity vs. total column water content. Heating rates as a function of pressure are not changed by the possible increase in IWC. This is a direct result of the fact that emissivity vs. distance below cloud top does not vary with IWC.

### 3.5 Comparison to Other Observational Studies

Measurements of the intensity emissivity of cirrus clouds have been made by several authors. The flux emissivity measurements made here have been corrected to intensity emissivity by using a diffusivity factor of 1.6 [Paltridge and Platt (1976)] and a comparison is then made in Figure 35 between the present measurements and other reported values. Note that this figure displays emissivity as a function of depth into the cloud. None of the other studies had any direct

INTENSITY EMISSIVITY

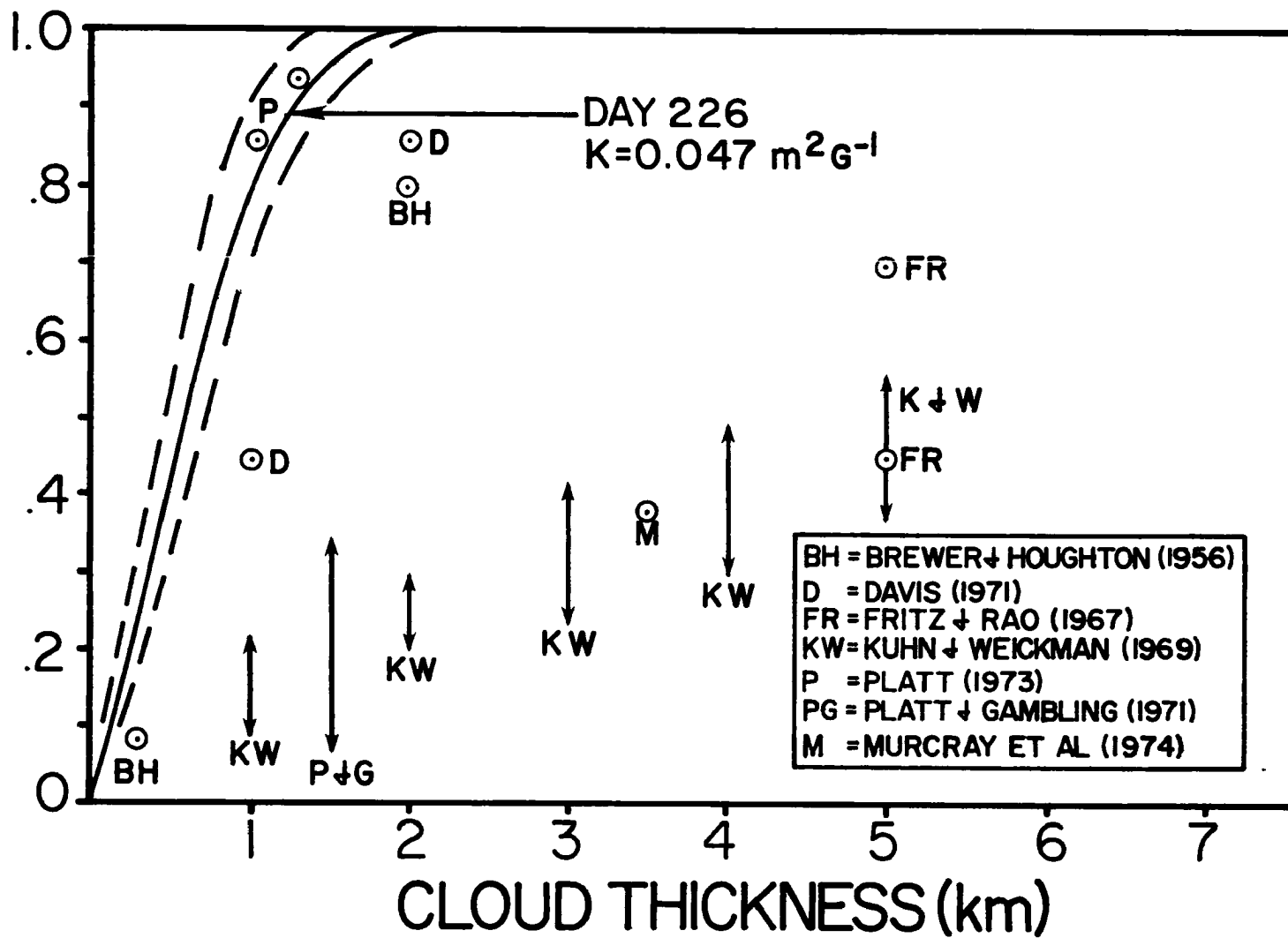


Figure 35. Comparison Between Present Study and Previous Observations of Intensity Emissivity vs. Cloud Thickness. (Dashed line envelope indicates uncertainty).

measurement of IWC available to them, thus a more direct comparison of emissivity vs. total water content is not possible. The studies of Platt (1973), Davis (1971) and Brewer and Houghton (1956) show emissivity values in the same general range as observed in this study. There is a broad range of observed values, however. The extensive study of Kuhn and Weickmann (1969) indicates much lower emissivities. None of their values approach 1.0 even for 5 km thick cirrus. In addition, most of the emissivity values observed by Platt (1973) would agree reasonably well with Kuhn and Weickmann. Platt, however, did not observe the strong correlation between cirrus thickness and emissivity found by Kuhn and Weickmann. Thus, Platt found emissivities ranging from less than 0.1 to approximately 0.9 for 1 km thick cirrus. This is undoubtedly due to the natural variability of cirrus cloud particle density. If the various measurements of emissivity could be referenced to some bulk cloud property such as water content, certainly much of the scatter in the observations would disappear.

There are two other studies [Allen (1971), Valovcin (1968)] which also reported cirrus emissivities that on occasion would approach unity. They have not been included in Figure 35 because no cloud thickness information was given in those studies. It should be noted that the mean emissivities reported by Valovcin and by Allen were much less than unity. For instance, Allen reported a mean cirrus emissivity of approximately 0.35. This is further indication of the wide variability of cirrus emissivity.

It is not surprising then, that the cirrus clouds sampled in this study were found to lie on the high end of observed emissivities. These clouds were produced from recent and/or continuing convective

activity in a moist tropical environment. It is quite possible that the clouds sampled were not even in an equilibrium state due to their close proximity in space and time to the generating cell. One would expect them to be more dense than the mid-latitude cirrus sampled by Kuhn and Weickmann.

Comparisons to theoretical studies of ice clouds have been made in previous figures. Figure 36 compares the current results of emissivity vs. total water content for ice clouds to three theoretical studies of typical liquid water clouds. [Hunt (1973), Zdunkowski and Crandall (1971) Yamamoto et al., (1970)]. The figure illustrates that there is disagreement between various authors as to the proper emissivity relationship even for similar liquid water content and drop size distribution. It is recognized, however, that the study of Zdunkowski and Crandall and the study of Hunt are spectral (10.6  $\mu$  and 11.0  $\mu$ , respectively) and that the work of Yamamoto et al., is broadband, covering 5  $\mu$  to 50  $\mu$ . This may account for a portion of the differences between the curves but certainly not all. The dense tropical cirrus clouds studied here are seen to be more similar to water clouds than to the ice clouds of Hunt or Liou.

The comparison made here depends, of course, on the assumptions made in the Appendix on deriving ice water content. Section 3.4 describes the effects of making different assumptions about the extrapolated portion of the particle size distribution.

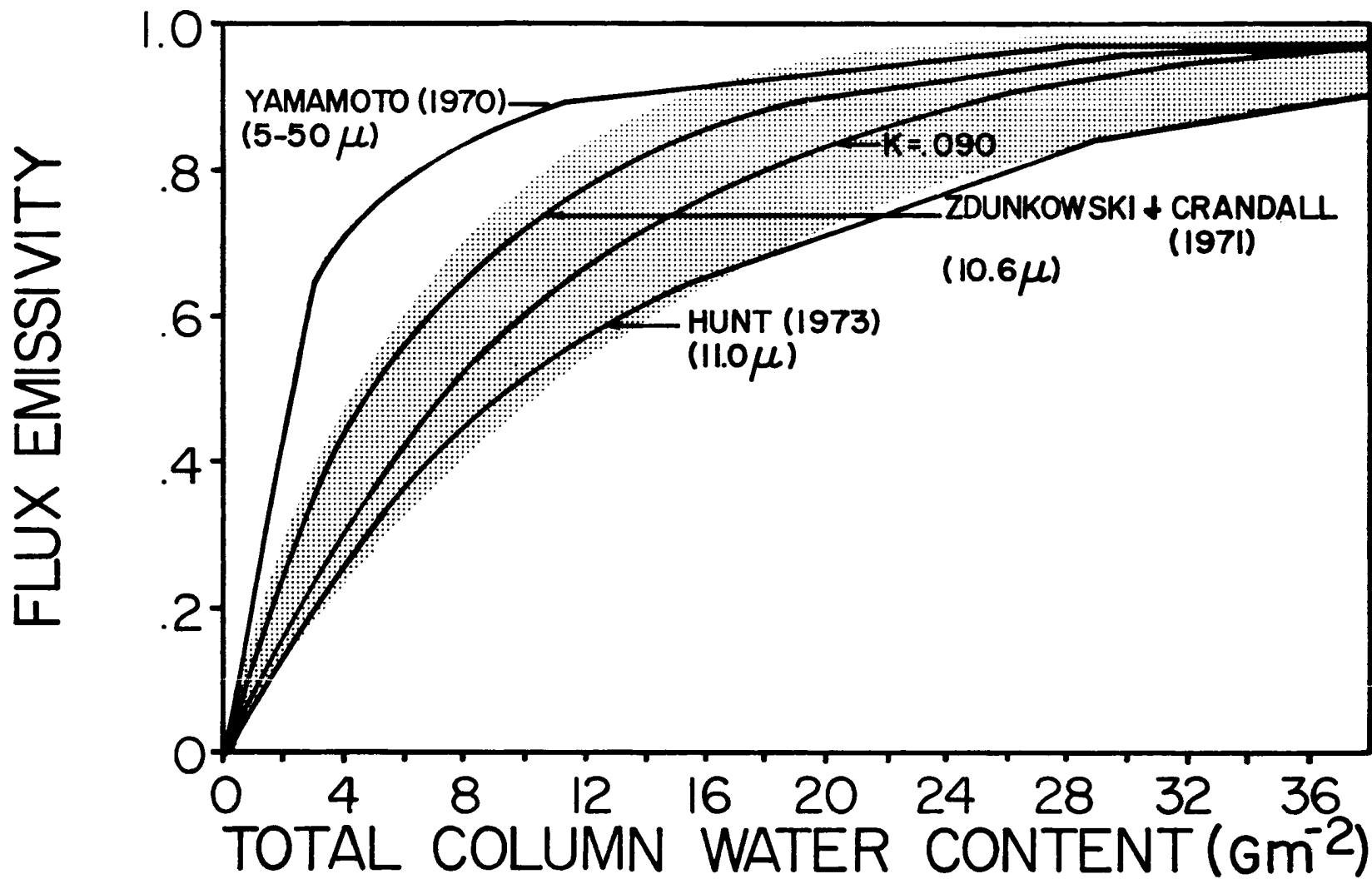


Figure 36. Comparison of Emissivity vs. Total Column Water Content Between Present Study and Theoretical results for Water Clouds of Similar LWC and Drop Size Distribution. (Stippled area indicates uncertainty in present observations).

#### 4.0 CONCLUSIONS

A broadband infrared radiative transfer computational routine has been developed and described which will determine cloud emissivities and cooling rates. A broadband mass absorption coefficient is also derived when the vertical structure of ice water content is known. The required inputs to the model are the vertical profile of upward and downward irradiance, temperature, water vapor, carbon dioxide, ozone, cloud base and top pressure, and ice water content.

This model has been used to analyze data collected by the National Center for Atmospheric Research (NCAR) Sabreliner during the GARP Atlantic Tropical Experiment (GATE) in the summer of 1974.

Three cases of high dense, CB anvil cirrus clouds were analyzed. It was found that these clouds approached an emissivity of 1.0 in a vertical distance of 1 - 1.5 kilometers. Comparison of these results with the theoretical results of Hunt (1973) and Liou (1974) revealed large discrepancies. Both of these theoretical studies predict emissivities of less than 1.0 even at over 6 kilometers into the cloud.

The data yielded mass absorption coefficients ranging from  $0.076 \text{ m}^2\text{g}^{-1}$  for Day 226 to  $0.096 \text{ m}^2\text{g}^{-1}$  for Day 232, with an average of  $0.084 \text{ m}^2\text{g}^{-1}$ . Again, comparison of emissivities vs. total column water content between the theoretical results of Hunt (1973) and Liou (1974) and the present study reveal large differences. It is postulated that the large irregular particles of real cirrus clouds have significantly greater extinction efficiencies than the spheres of Hunt's study or the regular columns of Liou's study.

Further comparison is made to measurements of cirrus emissivities as a function of depth of cloud made by other authors. A wide range of observational results have been reported. The studies of Platt (1973), Davis (1971), and Brewer and Houghton (1956) have some measurements in the same general range as the present study. However, the study of Kuhn and Weickmann (1969) reported no cirrus emissivities as high as those found here. These differences are probably due to the natural variability of cirrus cloud properties. If all of these diverse measurements could be referenced to the water content of the clouds, certainly most of the differences would be resolved.

Theoretical curves of emissivity vs. column water content for liquid water clouds as compiled by Yamamoto et al. (1970), Zdunkowski and Crandall (1971), and Hunt (1973) are compared to the results for ice clouds reported here. This comparison indicates that perhaps the differences between water clouds and ice clouds veiling the tropical cloud cluster are not as great as indicated by theoretical studies.

The infrared radiative heating rates within the cloud layer for these cirrus clouds are similar to those of lower cloud layers. The typical cloud top cooling maximum followed by essentially neutral heating rates deeper into the cloud was observed. The magnitude of the cooling spike at cloud top ranged from 12-16 °C/Day. The exact location of the cooling peak was found to be modulated by the ice water content structure near cloud top.

The high emissivity values of dense tropical cirrus reported in this study have important implications to the energy balance of the tropics. Manabe and Strickler (1964), in their classical theoretical study of the thermal equilibrium of the atmosphere found that the

temperature of the earth's surface may be warmed or cooled depending on the IR emissivity of the cirrus cloud and its position in the atmosphere. We can state on the basis of the Manabe and Strickler paper and the high emissivities found here that the presence of the tropical cirrus CB anvil acts to warm the surface.

Fleming and Cox (1974) reported on the suppression of tropospheric IR cooling by cirrus clouds. The high emissivities reported here will result in total tropospheric cooling that is only half of the clear sky value. In addition, this cooling is 40% to 50% less than would occur with cirrus emissivities of 0.5 which are suggested by the Kuhn and Weickmann study (1969).

These results lead to the conclusion that tropical cirrus clouds are significant positive contributors to the energy balance of the tropics.

## REFERENCES

- Albrecht, B., M. Poellot, and S.K. Cox, 1974. Pyrgeometer Measurements from Aircraft. Review of Scientific Instruments, 45, pp. 33-38.
- Albrecht, B.A. and S.K. Cox, 1976a. Radiation Data Reduction Procedures for Sabreliner, C-130, and DC-6 Aircraft during the GARP Atlantic Tropical Experiment. Colorado State University Atmospheric Science Paper No. 244, Fort Collins, Colorado.
- Albrecht, B.A. and S.K. Cox, 1976b. Pyrgeometer Data Reduction and Calibration Procedures. Colorado State University Atmospheric Science Paper No. 251, Fort Collins, Colorado.
- Allen, J.R., 1971. Measurements of Cloud Emissivity in the 8-13 $\mu$  Waveband. Journal of Applied Meteorology, 10, pp. 260-265.
- Bignell, K.J., 1970. The Water Vapor Infrared Continuum. Q. J. Roy. Meteor. Soc., 96, pp. 390-403.
- Brewer, A.W. and J.T. Houghton, 1956. Some Measurements of the Flux of Infra-red Radiation in the Atmosphere. Proceedings Royal Society (London) A, 236, pp. 175-186.
- Cox, S.K., 1971. Cirrus Clouds and the Climate. Journal of Atmospheric Sciences, 28, pp. 1513-1515.
- \_\_\_\_\_, 1973. Infrared Heating Calculations with a Water Vapor Pressure Broadened Continuum. Q. J. Roy. Meteor. Soc., 99, No. 442, pp. 669-679.
- \_\_\_\_\_, 1976. Observations of Cloud Infrared Effective Emissivity. Journal of the Atmospheric Sciences, 33, pp. 287-289.
- \_\_\_\_\_, M.C. Polifka, K. Griffith, A. Rockwood, and D. Starr, 1976. Radiative Transfer Computational Routines for Atmospheric Science Applications. Colorado State University Atmospheric Science Research Report.
- Davis, P.A., 1971. Applications of an Airborne Ruby Lidar During a BOMEX Program of Cirrus Observations. Journal of Applied Meteorology, 10, pp. 1314-1323.
- Feigel'son, E.M., 1970. Radiant Heat Transfer in a Cloudy Atmosphere. Israel Program for Scientific Translations, 191 pp.
- Fleming, J.R. and S.K. Cox, 1974. Radiative Effects of Cirrus Clouds. Journal of Atmospheric Science, 31, pp. 2182-2188.
- Fritz, S. and P. Krishna Rao, 1967. On the Infrared Transmission through Cirrus Clouds and the Estimation of Relative Humidity from Satellites. Journal of Applied Meteorology, 6, pp. 1088-1096.

## REFERENCES - Continued

- Heymsfield, A.J., 1975. Cirrus Uncinus Generating Cells and the Evolution of Cirroform Clouds. Part I: Aircraft Observations of the Growth of the Ice Phase. Jour. Atmos. Sci., 32, pp. 799-808.
- \_\_\_\_\_, 1976. Particle Size Distribution Measurement: An Evaluation of the Knollenberg Optical Array Probes. Atmospheric Technology, 8, pp. 17-24.
- \_\_\_\_\_, and R.G. Knollenberg, 1972. Properties of Cirrus Generating Cells. Journal of the Atmospheric Sciences, 29, pp. 1350-1366.
- Hunt, G.E., 1973. Radiative Properties of Terrestrial Clouds at Visible and Infrared Thermal Window Wavelengths. Quarterly Journal of the Royal Meteorological Society, 99, pp. 346-369.
- Knollenberg, R.G., 1970. The Optical Array: An Alternative to Scattering or Extinction for Airborne Particle Size Determination. Journal of Applied Meteorology, 9, pp. 86-103.
- \_\_\_\_\_, 1973. Measurements of the Growth of the Ice Budget in a Persisting Contrail. Journal of the Atmospheric Sciences, 29, pp. 1367-1374.
- \_\_\_\_\_, 1975. The Response of Optical Array Spectrometers to Ice and Snow: A Study of Probe Size to Crystal Mass Relationships. Air Force Cambridge Research Laboratories, ARCRL-TR-75-0494.
- \_\_\_\_\_, 1976. Personal Communication.
- Kuhn, P.M. and H.K. Weickmann, 1969. High Altitude Radiometric Measurements of Cirrus. Journal of Applied Meteorology, 8, pp. 147-154.
- Liou, K., 1974. On the Radiative Properties of Cirrus in the Window Region and their Influence on Remote Sensing of the Atmosphere. Journal of the Atmospheric Sciences, 31, pp. 522-532.
- Manabe, S. and R.F. Strickler, 1964. Thermal Equilibrium of the Atmosphere with a Convective Adjustment. Journal of Atmospheric Sciences, 21, pp. 361-385.
- Murcray, D.G., J.N. Brooks, F.H. Murcray and W.J. Williams, 1974. 10 to 12  $\mu\text{m}$  Spectral Emissivity of a Cirrus Cloud. Journal of Atmospheric Sciences, 31, pp. 1940-1942.
- Paltridge, G.W., 1974. Infrared Emissivity, Short-Wave Albedo, and the Microphysics of Stratiform Water Clouds. Journal of Geophysical Research, 79, pp. 4053-4058.

## REFERENCES - Continued

- Paltridge, G.W. and C.M.R. Platt, 1976. Radiative Processes in Meteorology and Climatology, Elsevier Scientific Publishing Company, 318 pp.
- Platt, C.M.R., 1977. Personal Communication.
- \_\_\_\_\_, 1973. Lidar and Radiometric Observations of Cirrus Clouds. Journal of the Atmospheric Sciences, 30, pp. 1191-1204.
- \_\_\_\_\_, and D.J. Gambling, 1971. Emissivity of High Layer Clouds by Combined Lidar and Radiometric Techniques. Quarterly Journal of the Royal Meteorological Society, 97, pp. 322-325.
- Smith, W.L., 1969. A Polynomial Representation of Carbon Dioxide and Water Vapor Transmission. ESSA Technical Report, NESC 47, 20 pp.
- Staley, D.O. and G.M. Jurica, 1970. Flux Emissivity Tables for Water Vapor, Carbon Dioxide and Ozone. J. Appl. Meteor., 9, No. 3, pp. 365-372.
- Valovcin, F.R., 1968. Infrared Measurements of Jet-Stream Cirrus. Journal of Applied Meteorology, 7, pp. 817-826.
- Walshaw, C.D., 1957. Integrated Absorption by the 9.6  $\mu$  Band of Ozone. Q. J. Roy. Meteor. Soc., 83, pp. 315-321.
- Yamamoto, G., M. Tanaka and S. Asano, 1970. Radiative Transfer in Water Clouds in the Infrared Region. Journal of the Atmospheric Sciences 27, pp. 282-292.
- Zdunkowski, W.G. and W.K. Crandall, 1971. Radiative Transfer of Infrared Radiation in Model Clouds. Tellus, XXIII, pp. 517-527.

## APPENDIX

## Derivation of Cirrus Cloud Ice Water Content from Knollenberg Probe Data

A one-dimensional optical array spectrometer operates on the principle that a cloud particle passing through a laser beam will cast a shadow on a linear array of photodiodes oriented at right angles to the flow. Basically, the number of photodiode elements darkened by the particle is proportional to the particle size (Knollenberg, 1970). The information is gathered and recorded on magnetic tape in one second intervals as the number of counts in each size channel. The Sabreliner Knollenberg probe was equipped to measure particles in 15 channels of nominally equal size from 20 $\mu\text{m}$  to 300 $\mu\text{m}$ .

The design of the probe dictates that spherical particles are sized and counted more accurately than any other shape. The particles in cirrus clouds are usually columns and/or bullet rosettes (Heymsfield and Knollenberg, 1972). This fact introduces a systematic error in the probe measurements. The cirrus crystals are normally undersized and undercounted. Heymsfield (1976) gives a very readable explanation of why the instrument responds in this manner.

This systematic error in the particle spectrometer was evaluated by Knollenberg (1975). His report details the theoretical probe response to particles of different shapes along with laboratory and field studies aimed at quantitatively defining the relationship between indicated and actual particle size. This report shows that the Knollenberg Probe is highly sensitive to particle shape. For instance, the corrected size of a spherical particle counted in the 200 $\mu\text{m}$  nominal channel would be 202.7  $\mu\text{m}$ . If that same count represented a column of 4:1 aspect ratio, the

corrected size would be  $250.0\mu\text{m}$ . Hence it is quite important to know what type of particles were sampled by the probe in order to make the correct conversions.

No data concerning crystal habit were collected by the Sabreliner on the GATE missions. The assumption was made that the particles were 50% columns and 50% bullet rosettes (Knollenberg, 1976). The indicated sizes of the raw data from the Sabreliner were then corrected using Figures 14 and 16 of Knollenberg (1975), which are reproduced below in Figures A1 and A2.

The Knollenberg Probe is designed and calibrated for optimum performance at aircraft speeds of 100 meters per second. At speeds above this figure the particles are transiting the photodiode array too quickly for proper instrument response. This results in significant undersizing. An empirical correction for this shortcoming was made according to equation A1.

$$\text{CSF} = \text{CS1} + 50\mu\text{m} (\text{TAS} - 100) \quad (\text{A1})$$

Where TAS is the aircraft true airspeed in  $\text{ms}^{-1}$ , CS1 is the corrected size from Figures 14 and 16 of Knollenberg (1975), and CSF is the final corrected particle size. Since the Sabreliner generally operated at speeds of 180 to 210  $\text{ms}^{-1}$ , the entire spectrum is shifted to larger diameters by an average of  $40\mu\text{m}$  to  $55\mu\text{m}$ . This implies that the instrument was actually measuring particles as large as  $460\mu\text{m}$  instead of the theoretical maximum of  $300\mu\text{m}$ . On the other hand, all particles less than approximately  $70\mu\text{m}$  were not counted by the instrument.

## COLUMN 4:1 PROBE RESPONSE

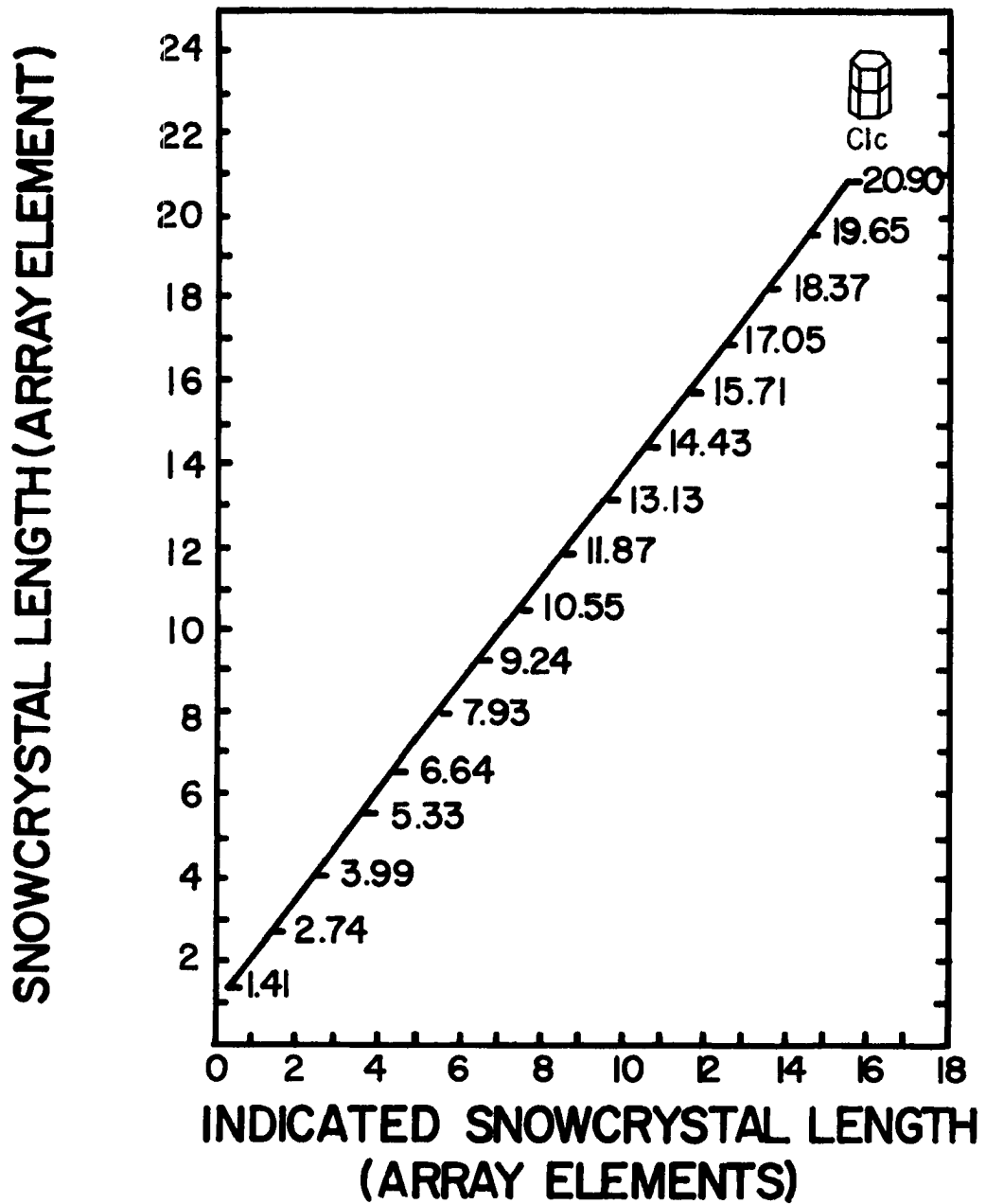


Figure A1. Corrected Crystal Size vs. Indicated Crystal Size  
(Reproduced from Figure 14 of Knollenberg (1975).

## ROSETTE PROBE RESPONSE

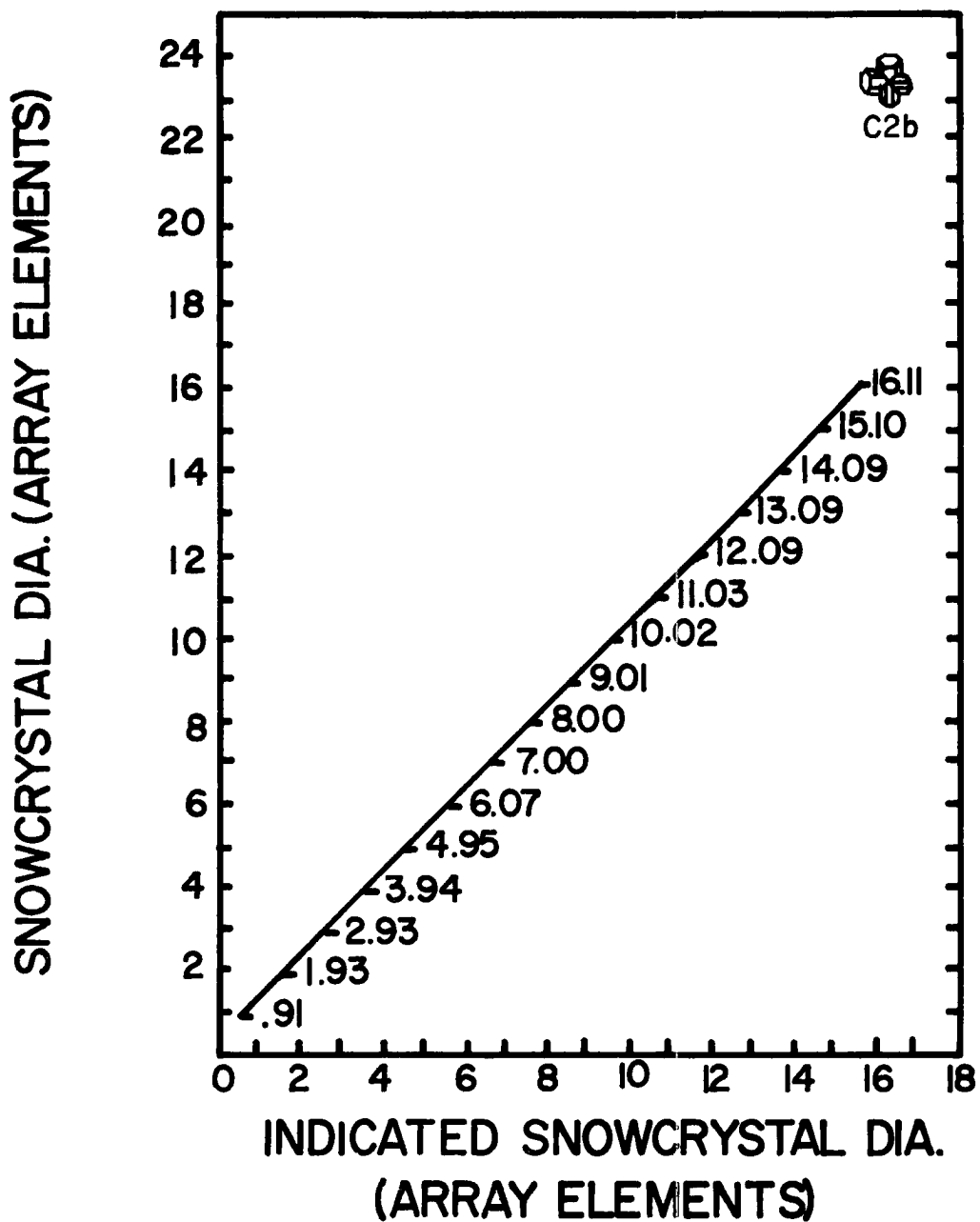


Figure A2. Corrected Crystal Size vs. Indicated Crystal Size  
(Reproduced from Figure 16 of Knollenberg (1975)).

The true size (length) of the crystal is now known. However, because of the somewhat irregular shape of the crystals, variable densities and variable aspect ratios, a conversion from crystal size to equivalent water drop diameter is needed. Extrapolations of Figures 41 and 43 of Knollenberg (1975) are used for this and are shown below in Figure A3. A table may now be constructed relating a count in a given nominal size channel to the equivalent water drop diameter. This is then easily converted to mass using the relationship for volume of a sphere and the density of water.

The water content of each particle has now been defined. It remains only to calculate the volume of air sampled each second so that the number of particles per second can be interpreted as a number of particles per cubic meter. This was done by multiplying the real sample area of each size channel as given by Knollenberg (1975) by the aircraft true airspeed to obtain cubic meters sampled per second.

In summary, the sequential steps used to find ice water content (IWC) are given below:

- 1) The number of particle counts per nominal size channel is determined from the raw data stored on magnetic tapes.
- 2) The nominal size channel is converted to the corrected size, CS1, by means of a table for the specific assumed particle shape (columns or bullet rosettes).
- 3) The shape corrected size, CS1, is adjusted for the excess airspeed according to Eq. A1 to yield the final crystal size, CSF, in each of the 15 channels.
- 4) The final crystal size is transformed according to its assumed shape to the equivalent water drop diameter by a tabular method.

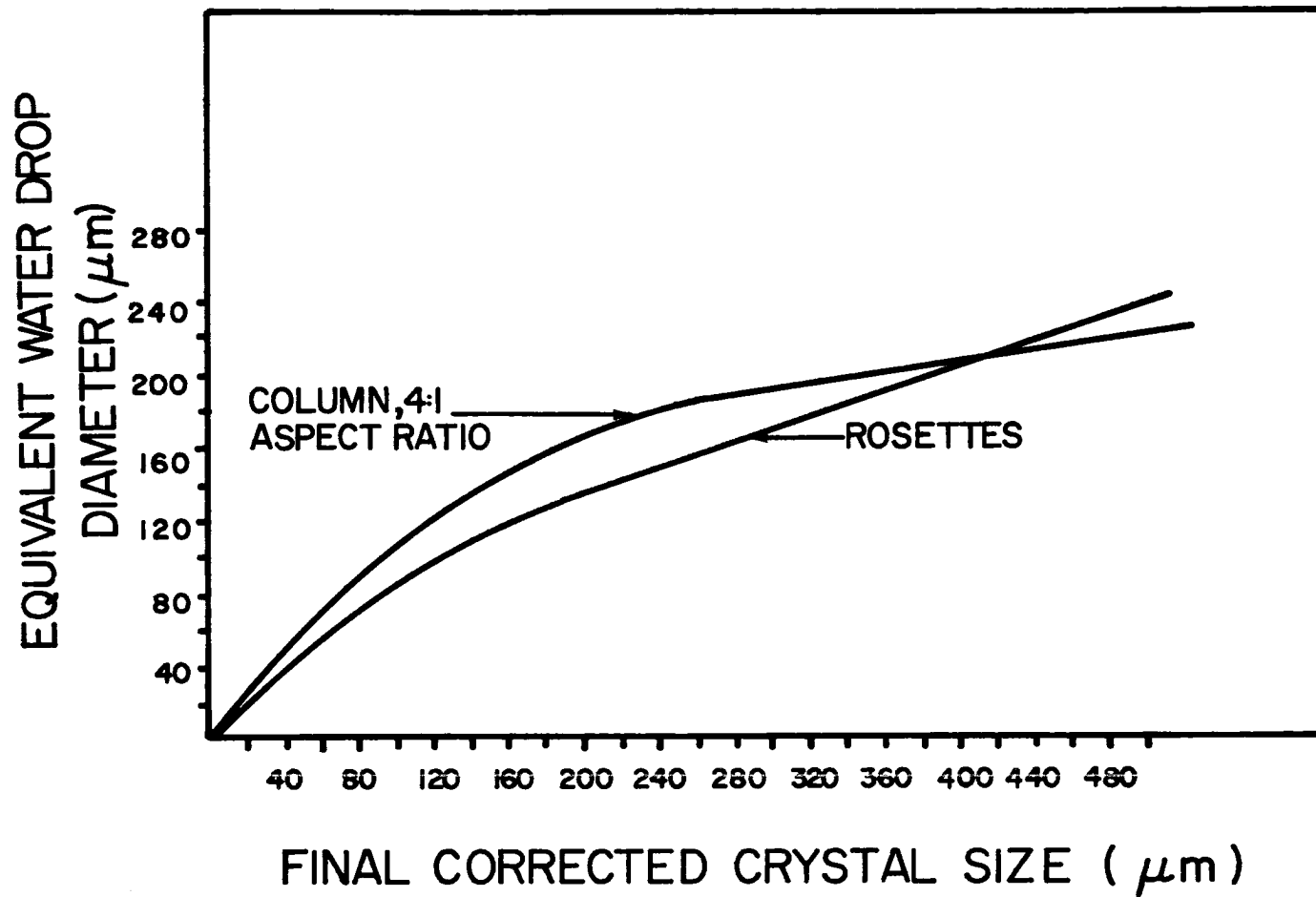


Figure A3. Equivalent Water Drop Diameter vs. Corrected Crystal Size for the Two Crystal Shapes Assumed to be Present.

- 5) Sample volume per channel is determined from the product of real sample area for each channel (tabular) and true air-speed.
- 6) Particles per cubic meter per channel is obtained by dividing raw counts per time interval by sample volume for that time interval.
- 7) Equivalent water drop diameter for each channel is multiplied by the expression for volume of a sphere and the density of water and the number of particles per cubic meter per channel to yield IWC in grams per cubic meter per channel. The sum over all channels gives the total mass of water per unit volume in the particle size range measured by the probe.

All of the data in the first 2 size channels (nominally 20 $\mu$ m and 40 $\mu$ m) were excluded from the calculations due to obviously bad data. Particle counts of 10,000,000 per cubic meter or more were commonly found in channel 1 and 10,000 or more in channel 2 even when flying in clear air. We assume that this exclusion will not affect total IWC more than a few percent since these small particles contain very little of the water and an extrapolation adjustment is made to account for their absence.

Measured IWC was adjusted upward to account for the fact that there were particles both above and below the size range of the instrument. The plots of IWC vs. final corrected particle size were extrapolated out for selected legs on each day and the average correction added to all the legs on that day. Figures A4 and A5 show the extrapolations used for both particles per cubic meter and IWC as a function of final

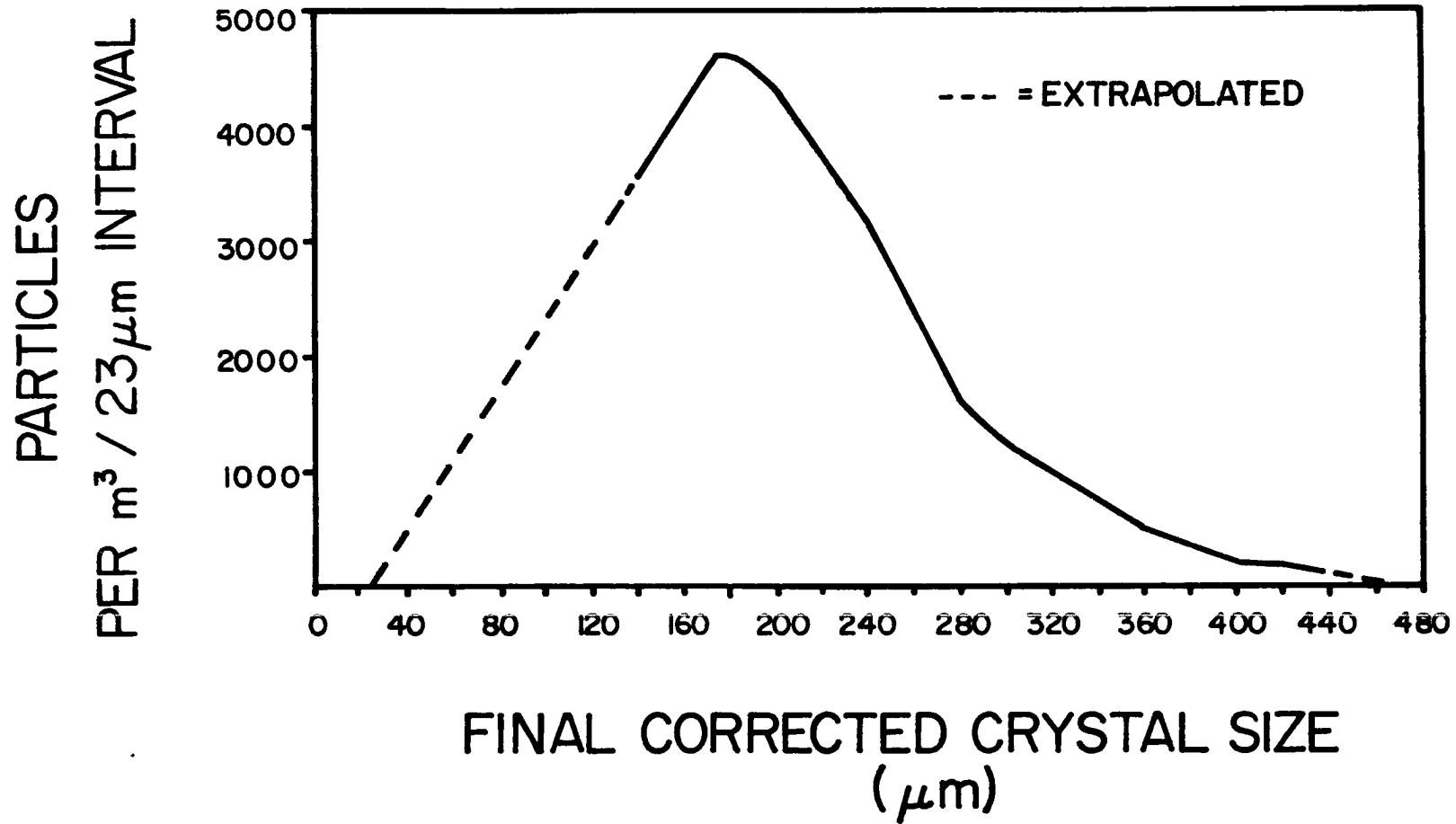


Figure A4. Particle size distribution for Day 226, 34,000 feet. Combined rosettes (50%) and columns (50%).

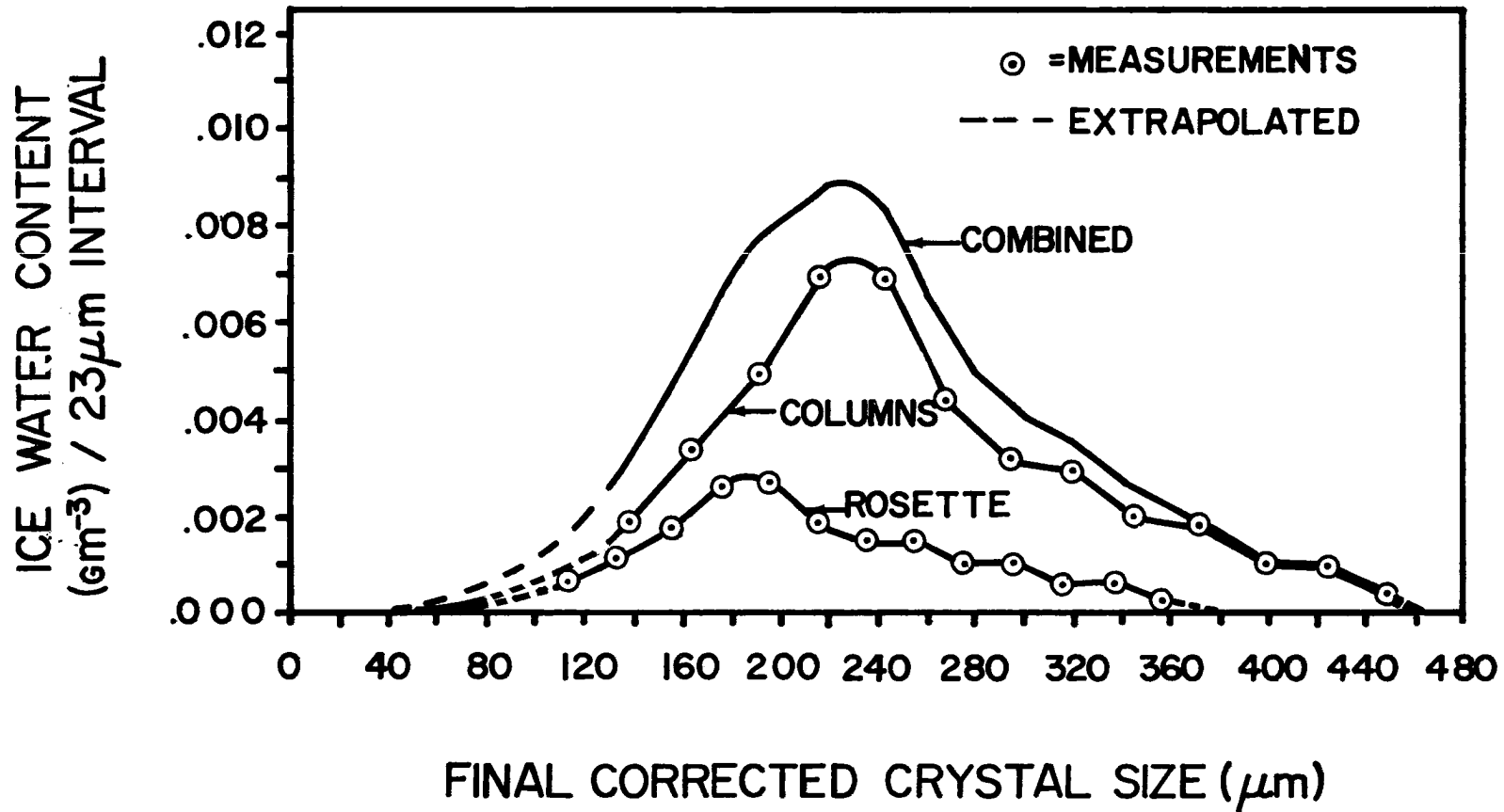


Figure A5. Ice water content as a function of particle size for a mixture of columns (50%) and Rosettes (50%) for Day 226, 34,000 feet. Ice water content is per  $25\mu\text{m}$  interval for curve representing columns and per  $20\mu\text{m}$  interval for curve representing rosettes.

corrected crystal size. Table A1 gives the correction factors used for each day.

It is possible that the number of particles in the small size channels is very much greater than assumed here. Figure A4 depicts the assumption we have made that the particle density drops linearly to zero from the measured peak near 180  $\mu\text{m}$ . If, in fact, the curve rises exponentially after the initial measured dip at 140  $\mu\text{m}$ , there may be significant amounts of ice water contributed by these smaller sizes. Such an exponential particle distribution was in fact reported by Heymsfield (1975). We have chosen in this study to use the extrapolation illustrated in Figure A4. Further discussion of the effects of having significant amounts of IWC outside of the measured size range is given in Section 3.4

TABLE A1. Correction factors used for adjusting measured IWC

Day 226	1.07
Day 232	1.08
Day 251	1.17

The effect on IWC of the assumption of 50% columns and 50% rosettes for the crystal shape is shown in Table A2. The raw data were processed for 5 different assumptions of crystal habit and for the size distribution of Figure A4. It is seen that the shape used in this study yields a value about midway between the maximum (spheres, columns) and the minimum (rosettes, small snow).

TABLE A2. The effect of particle shape assumption on calculated IWC

Shape Assumption	Calculated IWC ( $\text{gm}^{-3}$ )
Spheres (100%)	.0703
Columns (100%)	.0818
Rosettes (100%)	.0348
Small Snow (100%)	.0350
Columns (50%) and Rosettes (50%)	.0583

A sample of a typical particle size distribution and the resulting IWC distribution are given in Figures A4 and A5. Figure A4 is a graph of particles per cubic meter vs. final corrected particle size for the data flight leg at 34,000 feet on Day 226.

Figure A5 is a graph of IWC vs. final corrected particle size for the same flight leg as Figure A4. Note that in both figures the peak of the distribution and the bulk of the curve are well contained within the measured boundaries. Consequently, we have assumed that we have accounted for most of the IWC and that only a small correction term will be necessary to extrapolate to total IWC.

BIBLIOGRAPHIC DATA SHEET	1. Report No. CSU - ATSP - 269	2.	3. Recipient's Accession No.
4. Title and Subtitle Infrared radiative properties of tropical cirrus clouds inferred from broadband measurements.		5. Report Date April, 1977	6.
7. Author(s) Keith T. Griffith and S.K. Cox		8. Performing Organization Rept. No. CSU - ATSP - 269	
9. Performing Organization Name and Address Department of Atmospheric Science Colorado State University Fort Collins, Colorado 80523		10. Project/Task/Work Unit No.	
12. Sponsoring Organization Name and Address Office for Climate Dynamics National Science Foundation 1800 G. Street N.W. Washington, D.C.		11. Contract/Grant No. OCD -74-21678 04-6-158-44036	
12. Sponsoring Organization Name and Address GATE Project Office NOAA		13. Type of Report & Period Covered M.S. Thesis	
15. Supplementary Notes			
<p>16. Abstracts</p> <p>The longwave radiative properties of tropical cirrus clouds are studied using broadband hemispheric irradiance data. The data used were collected by the National Center for Atmospheric Research (NCAR) Sabreliner during the GARP Atlantic Tropical Experiment (GATE) in the summer of 1974. The longwave emissivities and the vertical profile of cooling rates are derived. Additionally, a broadband mass absorption coefficient relating water content to emissivity is defined. These parameters are determined by employing a broadband infrared radiative transfer routine. This model requires that the vertical structure of upward and downward irradiance, ice water content, temperature, water vapor and carbon dioxide along with cloud top and cloud base pressure be specified.</p> <p>Three cases of high cirrus clouds are analyzed. It is found that these clouds approached an emissivity of 1.0 in a vertical distance of 1.0 to 1.5 kilometers. Broadband mass absorption coefficients ranging from <math>0.076 \text{ m}^2 \text{ g}^{-1}</math> are derived. Comparison of these results to both theoretical and observational studies reveal large differences.</p> <p>Ice water content information is deduced from data collected by a one-dimensional particle spectrometer. Information on the variability of IWC in the horizontal and its correlation to downward irradiance is presented. The observed particle size distributions are also depicted and discussed.</p>			
<p>17. Key Words and Document Analysis. 17a. Descriptors</p> <p>IR radiation measurements Cirrus Ice Water Content IR cooling near cirrus Cirrus mass absorption coefficients Emissivities, cirrus</p>			
<p>17b. Identifiers/Open-Ended Terms</p> <p>GATE</p>			
17c. COSATI Field/Group			
18. Availability Statement		19. Security Class (This Report) UNCLASSIFIED	21. No. of Pages 102
		20. Security Class (This Page) UNCLASSIFIED	22. Price